9-20-2016 12:00 AM

Utilization of Lidar Intensity Data and Passive Visible Imagery for Geological Mapping of Planetary Surfaces

Taylor M. Haid
The University of Western Ontario

Supervisor
Dr. Gordon Osinski
The University of Western Ontario

Graduate Program in Geology
A thesis submitted in partial fulfillment of the requirements for the degree in Master of Science

Recommended Citation

Haid, Taylor M., "Utilization of Lidar Intensity Data and Passive Visible Imagery for Geological Mapping of Planetary Surfaces" (2016). *Electronic Thesis and Dissertation Repository*. 4187.
https://ir.lib.uwo.ca/etd/4187

Abstract

While lidar has been historically used for generating digital terrain maps and as a navigation tool, recent research demonstrates that lidar has many potential scientific applications, including high resolution analysis of geological outcrops. Case studies were completed at the Tunnunik impact structure, Victoria Island, Arctic Canada, and the Nickel Rim South mine, Sudbury, Canada, to assess the fidelity of characterizing and differentiating mineralogical and lithological units remotely by integrating passive visible imagery with lidar intensity data. Unsupervised classification via k-means clustering was performed on the fused datasets, with results indicating that lithologies can indeed be successfully differentiated with minor a priori knowledge of the setting. Semi-quantitative analysis through XRD of Tunnunik samples demonstrates that distance-corrected intensity is linked in a linear relationship with both dolomite and clay content. The simultaneous acquisition of both geospatial and scientific data greatly increases the applications and value of using lidar, especially for mining, geological mapping in remote environments, and for future planetary missions.

Keywords

Intensity, Terrestrial Laser Scanning, Lidar, Unsupervised Classification, Geology, Planetary Exploration, Ore Detection

Acknowledgments

First and foremost I must thank my supervisor Dr. Gordon Osinski for providing me with guidance and support throughout this project. During my two years here at Western, you have provided me with opportunities that I never thought would be possible; from studying an impact structure in the remote regions of Arctic Canada to being an instrument lead on an analogue mission in conjunction with the Canadian Space Agency. Thank you Oz.

I want to thank my co-advisor Dr. Michael Daly, for providing me with the technical support on understanding lidar, which was a technology completely foreign to me at the beginning of my studies here. I am also extremely grateful for the funding and opportunities provided to me by the NSERC CREATE 'Technologies and Techniques for Earth and Space Exploration' Fellowship, along with the Ontario Graduate Scholarship (OGS) program.

Thank you to Jeremy, Rob, Hun, Racel, William, Jen, Livio, Jean, and the rest of the Tunnunik crew for helping me haul my bulky and extremely heavy lidar instrument all over the crater. Your company in the land of the midnight sun helped make this expedition something I will always remember fondly.

I am grateful for the assistance on any and all technical issues that I ran into with the ILRIS provided by Dave Adams at Teledyne-Optech, along with Stephen Falconer of Glencore and Damien Duff of the Ontario Centre for Excellence in Mining Innovation (CEMI), who helped get me underground to perform scans. Thanks to Raymond Francis and Shamus Duff for the assistance with the scans at Nickel Rim South.

To my family: Mom, Dad, Drew, and Sydney, thank you for the continual support of my endeavours; I would not be here without you. Thank you to my friends and fellow planetary scientists and geologists who have made this experience better than I could have ever imagined: Connor, Ian, Diego, Danny, Gordy, Mary, Becca, Zach, Patrick, Matt, Marcus, and Adam. I also want to thank my defense committee members Livio

Tornabene, Catherine Neish, Jinfei Wang, and the chair of the examination, Bob Linnen for providing me with prompt and helpful edits of this thesis.

Table of Contents

List of Tables

List of Figures

List of Appendices

Chapter 1

1 Introduction

Geology is in part, a descriptive science, and often requires a three-dimensional understanding of the environment in order to solve geological problems. Traditionally, geologists have used sketches in field notebooks, along with cameras, air photos, and more recently, Global Positioning System (GPS) devices to record field observations to elucidate these problems. The issue with these traditional tools is that they do not provide a 3D representation of the geological area of interest, which is what a geologist requires in order to truly immerse themselves in the data. The advent of laser scanning has led to the generation of high resolution 3D models, which can be utilized by the geologist to ‘revisit’ a scanned site even after returning to the office. The application of lidar to geology is also leading to new avenues for accurate remote lithological classification, which is explored in this investigation. The purpose of this investigation is to ascertain if mineralogy of certain materials can be correlated with corrected lidar intensity (at the near infrared wavelength of the lidar instrument) and also to determine the viability of remotely discriminating lithologies through fusion of corrected lidar intensity with passive visible imagery with only minor *a priori* knowledge of the setting. Case studies were performed at the Tunnunik impact structure and underground at the Nickel Rim South mine to confirm and assess the fidelity of this method and its applications to the future of planetary exploration and mining.

1.1 Lidar

Lidar (light detection and ranging) is a rapidly advancing laser scanning and surveying technique which is becoming a vital tool in multiple fields, and currently has platforms for spaceborne, airborne, and ground-based applications (Kemp, 2008). Lidar operates on the same principles as radar, except at shorter wavelengths (Jelalian, 1992). The earliest and most common utility for lidar has been the generation of detailed three-dimensional topographic measurements of surface relief via airborne scans (Pfeifer and Briese, 2007). This technique uses the time-of-flight principle and angle of emission to measure ranges via laser pulses—between 500 nm and 1550 nm—to objects with extremely high accuracy (Jensen, 2007; Pfeifer and Briese, 2007). The receiver can collect hundreds of thousands of points per second, with each point containing specific x, y, and z coordinates that can be attributed to a precise point on the object or surface that is being scanned. The range (z value) is calculated by halving the product of the two-way travel time of the laser pulse and the speed of light (Jensen, 2007), while the x and y values are related to the position of the transmitter at the moment the laser pulse exits the instrument (Jensen, 2007; Bellian, 2005). The collection of these data points, each with unique and distinct values from the corresponding scan, are collectively known as a point cloud (Fig. 1.1) (Jensen, 2007).

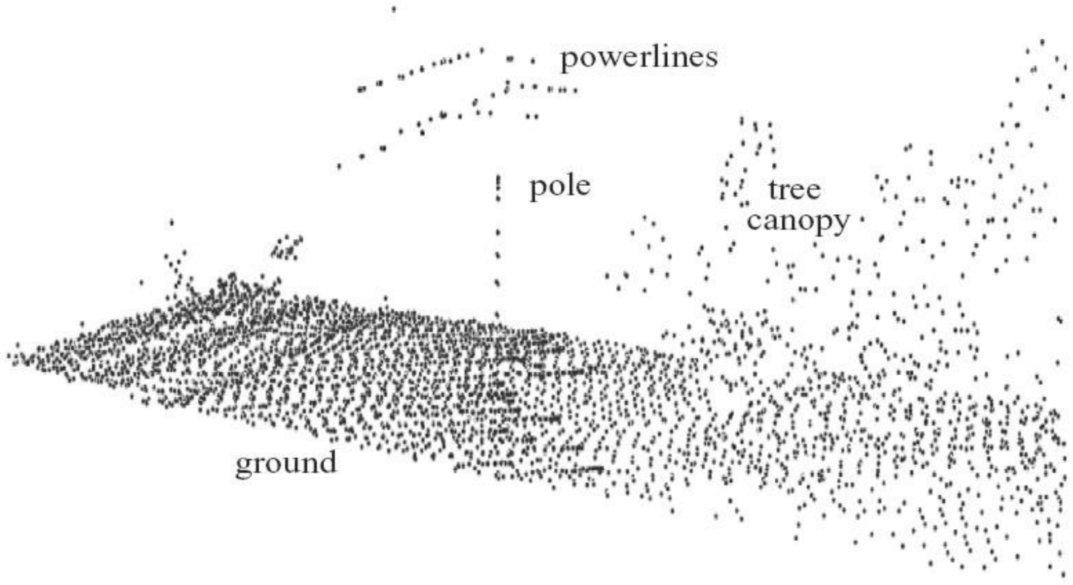

Figure 1.1. Example of a point cloud collected by an aerial lidar scan, which show points returned off the ground, powerlines, and tree canopy (from Jensen, 2007).

The increased utilization of lidar in multiple fields most likely has been influenced by the fact that it has multiple benefits over traditional passive remote sensors. These benefits include the ability to acquire highly resolved and accurate collection of 3D point clouds from up to thousands of metres away and the collection of multiple returns from a single pulse, allowing ground surface discrimination even in forested environments. Lastly, lidar is an active remote sensor, which means it does not require ambient lighting to collect data, making this an excellent tool for planetary exploration (ability to operate on night side orbits for planetary bodies) and underground and/or poorly lit applications (e.g., mining, pipeline inspection, etc.), where surface illumination is not always possible.

Each laser pulse emitted from the instrument can yield single or multiple returns, depending on the nature of the surface being scanned. The number of returns is a function of the initial beam diameter (instrument specific), the scan angle, the material properties of the surface, and the range of the target from the instrument. These factors will dictate the diameter of the instantaneous laser footprint of each laser pulse (Jensen, 2007). For example when scanning a forested area from above, some portion of a single pulse may reflect off the canopy of a tree (1st return), while another portion hits lower branches (2nd return), with the final portion hitting the ground surface (last return) (Fig. 1.2) (Jensen, 2007). Post processing of the data allows the user to tailor the results based on their respective needs, and choose whether to generate the point cloud from the first return, or the final. If the focus is on identifying tree density or height, the first returns would be utilized, whereas if the focus were on creating a bare earth model, the last (ground) returns would be used.

Besides providing detailed spatial information, lidar instruments also record the intensity of the returned laser pulse. This intensity is a measure of the backscattered energy (at the wavelength of the laser) reflected off the target relative to the energy of the initial pulse (Jelalian, 1992), which generally is scaled to 8, 12, or 16-bit dynamic range and can be included as a parameter in the point cloud (Höfle and Pfeifer, 2007; Kashani et al., 2015). The intensity response will be investigated further in section 1.2. This data can be stored in multiple file formats (often manufacturer-specific), with the most common format being the ASCII .xyz file, which stores data in columns with X, Y, Z, intensity values, as well as other possible entries including scan angle and time. More recently, the LAS(er) file format has become the main format for the exchange of point cloud data between users. Benefits of the LAS format include the fact that it is a binary file format, with smaller files compared to ASCII, while still retaining the necessary lidar data for further processing and analysis (ASPRS, 2016).

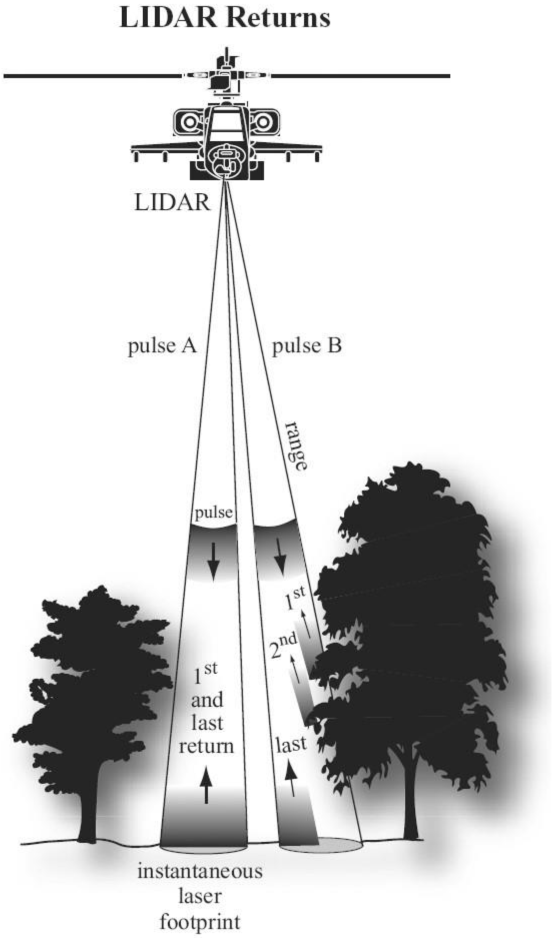

Figure 1.2 Depiction of how multiple returns can be generated from a single laser pulse. For example, all of the energy from pulse A interacts with the ground, meaning there is only one return. Pulse B has returns from two parts of the tree canopy, along with the ground, leading to three separate returns. Note that this only affects the range (z value) of the data point (from Jensen, 2007).

A growing range of instrumentation is becoming available for aerial and terrestrial laser scanning. While the focus of this thesis is on the utilization of a ground-based scanner, basic information regarding both aerial and terrestrial scanners will be mentioned here for context.

Aerial laser scanners (herein noted as ALS) were the main method of acquisition in the early days of laser scanning, providing wide area data acquisition in swaths across the Earth’s surface. Mounted to fixed-wing planes or helicopters, these instruments would collect detailed spatial information that led to the development of high quality topographic profiles. The spatial data collected from the moving aircraft is defined with the help of Global Positioning Systems (GPS) along with an internal measurement unit (IMU) to record the pitch, yaw, and roll of the aircraft in flight (Jensen, 2007). Meanwhile, terrestrial laser scanners (herein noted as TLS) are stationary, and often mounted on tripods. In order to acquire data, rotating mirrors within the instrument allow the laser pulses to cover the area of interest across the angular domain (Pfeifer and Briese, 2007). While ALS excels at collecting surface information, it lacks the ability to gather information on vertical faces, such as façades of buildings, or even canyon walls. TLS is an excellent solution to this, as it can acquire detailed façade information at extremely high resolution. Generally, TLS are able to collect higher resolution data due to the closer range of the scanner to the target (tens to hundreds of metres, as opposed to hundreds to thousands of metres with ALS) (Cheng et al., 2015). Most ALS and TLS instruments are considered discrete echo scanners, which generally document the maximum amplitude of the return pulse. Recently full waveform systems have hit the commercial market for both systems, which digitizes and documents the entire echo waveform from the backscattered pulse energy (Pfeifer and Briese, 2007; Kaasalainen et al., 2008). While work with full waveform lidar is still in its infancy, it is believed that using this technology will lead to increased applications and more effective classification of the data collected by ALS and TLS (Kaasalainen et al., 2008; Hartzell et al., 2013).

1.2 Intensity

Lidar intensity has become a topic of much interest within the remote sensing community, as it presents potential for a multitude of applications, including improved classification of scenes, as well as the possibility of distinguishing between materials with different reflective or compositional properties (Burton et al., 2011). Intensity data is related to the target reflectance, but is also influenced by several other variables, which must be corrected for before the intensity can be considered as a proxy for absolute reflectance. The four main variables affecting intensity include: (1) data acquisition geometry; (2) target surface characteristics; (3) instrumental effects; and (4) atmospheric effects; all of which will be addressed in the following section.

This absolute reflectance of the target material is what many recent studies have attempted to identify through radiometric correction or calibration. With regard to geological applications, once the intensity is calibrated at the instrument-specific wavelength, spectral and textural differences between geological units can be identified, aiding in the remote characterization of materials, especially in remote or inaccessible environments such as deep mines or even other planetary bodies including the Moon and Mars.

1.2.1 Effect of Acquisition Geometry on Intensity

Acquisition geometry, including range (R) (the distance between the instrument and the target) and angle of incidence (α) (the angle between the laser beam and the target surface normal) play a large factor in the intensity response. In a recent review paper, it has been noted that the majority of correction and calibration methods developed to date have been to correct for these acquisition geometry factors (Kashani et al., 2015).

In regards to range, the main factor is that with increasing distance to the target, the laser pulse must travel through more atmosphere, resulting in a diminishing return strength. For extended targets, raw intensity is generally accepted to be a function of the inverse range square ($1/R^2$), and this relationship is visualized in Figure 1.3a. (Wagner et al., 2006; Höfle and Pfeifer, 2007; Pesci et al., 2008; Krooks et al., 2013). Extended targets are defined as targets larger in size than the laser footprint, and therefore remove the effect of beam divergence, resulting in a $1/R^2$ relationship as opposed to $1/R^4$ (Pfeifer et al, 2008). Non-extended targets refer to targets that have an area smaller than the laser footprint, such as wires or leaves, which would lead to a different range dependence, appearing to be a function of the inverse range with higher powers ($1/R^3$, $1/R^4$) (Jelalian, 1992; Pfeifer et al., 2008).

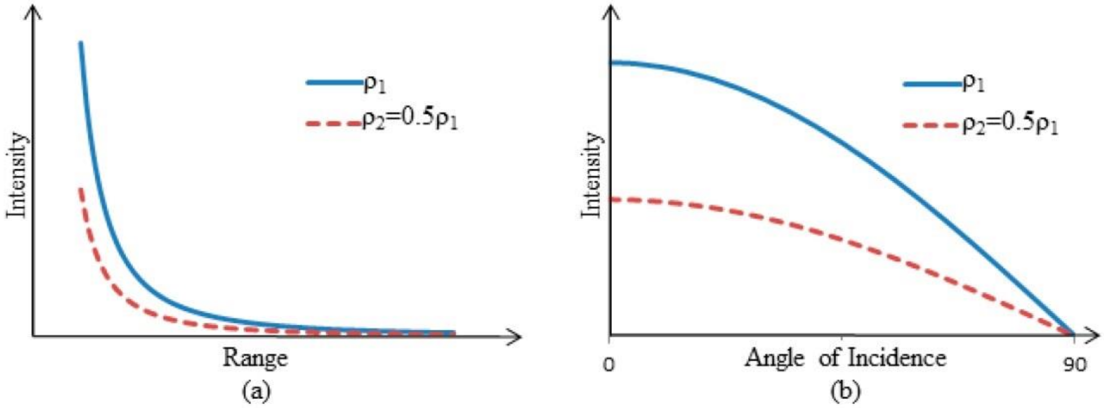

Figure 1.3. a) The $1/R^2$ relationship between intensity and range for two materials of differing reflectance. b) The cos (α) relationship between intensity and angle of incidence for two materials of differing reflectance. ρ represents material reflectance at the laser wavelength (from Kashani et al., 2015).

The angle of incidence between the target surface and the laser beam pulse also has a direct influence on the intensity return. In general, increasing incidence angle will lead to a decrease in intensity, due to less of the initial beam being backscattered in the direction of the sensor. Generally, TLS will have greater variations in both range and incidence angle compared to ALS. For example, TLS often are utilized to capture a 360° panoramic scan of an area including the ground surface, which leads to data points collected at extremely oblique angles (Chin et al., 2015). Another potential issue arising from TLS is the fact that multiple scans of the same area may be acquired (often with overlap) in multiple scanning locations, so as to create a complete dataset without gaps in the point cloud. These point clouds must then be merged, raising the issue of objects present in multiple clouds, but having different ranges and angles. This leads to objects with mixed intensity values in the merged point cloud which must be accounted for prior to further processing (Kashani et al., 2015).

As noted by (Krooks et al., 2013), the incidence angle is related to both the scanning geometry as well as to the target surface characteristics. Raw intensity is generally accepted to be reduced by the cosine of the angle of incidence (Fig. 1.3b), assuming Lambertian behaviour (Pesci and Teza, 2008; Pfeifer et al., 2008; Jutzi and Gross, 2009). Lambertian materials are considered diffuse reflectors that reflect radiance equally in all directions, and intensity proportionally to the cosine of the angle of incidence (Carrea et al., 2016). Several authors have noted that it becomes important to correct intensity values for incidence angle when angles exceed 20^0 for most materials (Kaasalainen et al., 2009; Kaasalainen et al., 2011; Krooks et al., 2013). Others note that the effect of incidence angle appears to be neutralized by the presence of macroscopic irregularities at the scale of the laser footprint (mm to cm) due to the fact that a significant part of the surface illuminated by the laser pulse will always be normal the scanner (Pesci et al., 2008; Kaasalainen et al., 2011; Hartzell et al., 2014; Penasa et al., 2014). This is important when applying this to natural surfaces such as geological outcrops, which are characterized by roughness on the scale of the laser footprint.

1.2.2 Effect of Target Surface Characteristics on Intensity

The effect of target surface characteristics is often the main parameter of interest in recent studies which aim to isolate and utilize the reflectance of the scanned surface for remote classification and differentiation of materials. Target surface characteristics are influenced by two main factors, which are reflectance and roughness.

Reflectance of the target material can be defined as the ratio between the power of the reflected laser pulse and the incident laser pulse (Reshetyuk, 2006). The higher the surface reflectance, the more of the laser pulse that will be returned to the instrument, leading to a higher intensity reading for that specific point. Using two different lithologies present in an outcrop as an example, it would be expected that dolomite would have a higher reflectance than that of a shale. The reflectivity of rocks is controlled by a complex combination of variables including moisture, composition of individual grains, and grain size, to name a few (Burton et al., 2011). Theoretically, dolomite, with the higher tonality, will scatter more photons back toward the receiver, while shale will absorb more of the photons, due to its darker tonality and finer grain size. The vast majority of TLS available today are single wavelength systems, which means that the differentiation of materials via reflectance requires spectral separation at the specified wavelength. It is important to note that TLS instruments produced by different companies often use lasers of different wavelengths, so the reflectivity of the targeted material will be specific to the wavelength used. Fusion of hyperspectral imagery with terrestrial lidar point clouds is a recent advance that provides increased spectral separability between materials, and will be further addressed in Section 1.3.3. It follows that in order to elucidate the true reflectance of the scanned material, all of the other parameters that affect the intensity response must be eliminated or reduced. To achieve this, many authors have proposed methods for radiometric calibration, which often rely on scanning reference targets with known absolute reflectance that are then compared to the intensity response from the instrument (Pfeifer et al., 2007; Pfeifer et al., 2008; Kaasalainen et al., 2009; Kaasalainen et al., 2011; Krooks et al., 2013).

The influence of surface roughness on the intensity response has begun to be investigated by several authors (Pesci et al., 2008; Kaasalainen et al., 2009; Mills and Fotopoulos, 2013), but a standardized correction has yet to be implemented (Carrea et al., 2016). Carrea et al. (2016) propose a correction for target surface roughness using the Oren-Nayar reflectance model, stating that natural rock surfaces deviate from Lambertian behaviour at incidence angles over 60^0. This correction may be beneficial for scans of natural surfaces from multiple scanning positions at high incidence angles. For TLS scans where the surface of interest is normal (or of low obliquity) to the laser pulse, the surface may still be considered Lambertian (Pesci et al., 2008; Pesci and Teza, 2008; Franceschi et al., 2009).

1.2.3 Instrumental Effects on Intensity

Intensity returns are unitless measurements of the maximum response of the laser pulse, and specific to the instrument being used. These measurements vary between instrument manufacturers, and in order to develop a reflectance measurement method that is consistent for all instruments, specific instrument parameters must be known (Hartzell et al., 2013; Kashani et al., 2015). These parameters include wavelength, laser power, beam divergence, and aperture size of the scanner. As mentioned previously, the laser wavelengths used for ALS and TLS can range between 500 nm and 1550 nm. Pfeifer and Briese (2007) note that ALS tend to utilize lasers at 1060 nm or 1550 nm, while TLS can be more variable and range the entire span from 500 nm to 1550 nm. An assessment of several available TLS indicates this variability, with the Leica HDS3000 having a wavelength of 532 nm, the Zoller + Fröhlich (Z + F) IMAGER 5003 at 785 nm, and the Riegl VZ-400 at 1550 nm (Hartzell et al., 2014). The Teledyne-Optech ILRIS TLS, which is used in the following study, has a wavelength of 1535 nm (near infrared) (Optech, 2016). A benefit of using a TLS with a wavelength in the near infrared (as opposed to in the visible spectrum) is that if the data is fused with a digital camera image, there are now four separate wavelengths that can be utilized for image classification. Laser power, or transmitted energy also varies with each manufacturer, which affects the amount of backscattered energy returned from each pulse (Kashani et al., 2015). Beam divergence—which is an angular measure of how much the beam diameter will increase with distance—also varies between instruments, which will result in different laser footprint diameters at a certain range. Lastly, aperture size will have an effect on the angular resolution of the backscattered response (Kaasalainen and Kaasalainen, 2008). A larger aperture will allow for greater admittance of light, which could increase the signal strength. While most ALS have aperture sizes varying from 8 to 15 cm, TLS are generally smaller, and on the order of several centimetres (Kaasalainen and Kaasalainen, 2008). This difference in aperture size between airborne and terrestrial instruments is due to the fact that the ranges are generally much larger for airborne scans compared to terrestrial.

1.2.4 Atmospheric Effects on Intensity

The final parameter which influences the intensity return in laser scanning is the effect of atmospheric attenuation and wetness. As the laser pulse travels from the sensor to the surface, it must travel through the atmosphere, which can reduce the backscattered response. The influence of atmospheric attenuation is most seen in scans with high ranges. This often means that ALS are more affected by this factor than for TLS with shorter ranges. Especially for airborne scans at the scale of kilometres, aerosol and Rayleigh scattering must be accounted for, which represent scattering due to dust, smoke, or water droplets and scattering due to small air particles and clusters, respectively (Yan et al., 2012). As previously mentioned, terrestrial scans at a short range (tens to hundreds of metres), the atmospheric attenuation can often be considered negligible (Franceschi et al., 2009).

It has been documented that water causes a strong absorption in the near infrared, around 1400 nm (Clark, 1999), which leads to a decreased intensity return from wet targets, especially for TLS that operate in the near infrared. (Kaasalainen et al., 2009) note that scans of wet brick led to a 30% to 50% decrease in intensity when compared to the returns from the dry brick. Even if the target is dry, when humidity is high enough, the intensity values will fall (Franceschi et al., 2009). These atmospheric conditions are important to note and document when attempting to observe changes over time in an area, as only scans that occur under similar weather conditions will be able to be compared with high levels of confidence.

1.2.5 The Lidar Range Equation

The lidar range equation has been developed from the radar range equation, which is described in (Jelalian, 1992), and relates the parameters which decrease the transmitted signal power from the received signal power. This equation incorporates all of the aforementioned factors, and is the basis for the majority of processing methods available today. While many forms of the lidar range equation are available in the literature (Wagner et al., 2006; Kaasalainen et al., 2009; Kaasalainen et al., 2011; Hartzell et al., 2013), the format provided by Carrea et al. (2016) will be utilized here.

$$P_r = \frac{P_t D_r^2}{4\pi R^4 \beta_t^2} \eta_{sys} \eta_{atm} \sigma_{cross} \tag{1}$$

where P_r is the received pulse power in watts; P_t is the transmitted pulse power in watts; D_r is the instrument aperture diameter in meters; η_{sys} is the system transmission efficiency; η_{atm} is the atmospheric transmission factor; σ_{cross} is the target cross section in square meters; R is the range from the scanner to the target in meters; and β_t is the laser beam width in radians.

Assuming that all of the laser beam hits the target and that the surface is Lambertian in nature, the target cross section is:

$$\sigma_{cross} = \pi \rho_{\lambda} R^2 \beta_t^2 \cos\alpha \tag{2}$$

where ρ_{λ} is the target surface reflectivity at a specific wavelength; and α is the angle of incidence between the beam and the normal to the surface.

Substituting σ_{cross} from Eq. (2) to Eq. (1) leads to a simplified lidar equation (3), which leads to the inverse range squared dependency of the received pulse power.

$$P_r = \frac{P_t D_r^2 \rho_{\lambda} \cos\alpha}{4R^2} \eta_{atm} \eta_{sys} \tag{3}$$

The remaining variables can be broken into three categories: instrumental (P_t, D_r η_{sys}) and atmospheric (η_{atm}) factors; acquisition geometry factors (R, α); and target reflectance (ρ_{λ}). (Carrea et al., 2016) note that both transmitted pulse power (P_t) and aperture diameter (D_r) are deemed as constant for a particular TLS instrument, and so can be eliminated from the equation. The atmospheric transmission factor is dependent on the weather conditions present during the scan, and as previously mentioned, can be greatly affected by humidity or aerosol concentrations, and often influence ALS far more than TLS. For a TLS, assuming that the conditions under which the scans were acquired were stable, and that transmittance was consistent, η_{atm} can also be considered a constant (Carrea et al., 2016).

This leads to the received power being proportional to the product of the target reflectivity and the cosine of the incidence angle, and inversely proportional to the square range:

$$P_r \propto \frac{\rho_\lambda \cos \alpha}{R^2} \tag{4}$$

The received power (P_r) of the TLS is generally converted into a Digital Number (DN) which is documented as the raw intensity value (I_{raw}). This value is often manufacturer specific, and related to the parsing software used. That being said, simple tests have proven that raw intensity is directly proportional to the received power (Carrea et al., 2016):

$$P_r \propto I_{raw} \tag{5}$$

Using Eq. (5), and assuming a Lambertian surface, I_{raw} can be substituted for P_r:

$$I_{raw} \propto \frac{\rho_\lambda \cos \alpha}{R^2} \tag{6}$$

Finally, the target surface reflectivity factor (ρ_λ) can be utilized to differentiate between different lithologies if it is corrected to remove the effects of incidence angle and range. The corrected intensity value (I_{corr}) is therefore proportional to the wavelength-specific target surface reflectivity.

$$I_{corr} = \frac{I_{raw} R^2}{\cos \alpha} \tag{7}$$

It is important to note that the utilization and application of intensity data from lidar is a developing field, and while there have been multiple calibration methods proposed (Pesci et al., 2008; Franceschi et al., 2009; Kaasalainen et al., 2011; Penasa et al., 2014; Carrea et al., 2016), a standard method for all scanners still does not exist. When developing an experiment involving TLS, one must be aware of the instrumental effects of the chosen sensor, as well as taking into account the environment in which the scanning is to take place. For example, different corrections will have to be applied for a close-range scan that is focusing on a vertical rock outcrop with little range variation compared to a long-range scan of a glacial valley, which would contain large variation in both range and incidence angles. While outside the scope of this study, a comprehensive review of lidar correction models can be found within (Kashani et al., 2015)**.** The correction methods utilized for this thesis begin with Eq. (7) and will be elaborated on in the following chapters.

1.3 Applications Utilizing Lidar Intensity Data

The burgeoning field of laser scanning has led to a rapid growth of applications interested in applying the intensity data to solve unique problems. Olsen et al. (2013) have developed techniques to analyze and assess pre-disaster hazards and post-disaster damage. Structural damage assessment studies have also been undertaken for crack detection in concrete as well as for bridge surface degradation (Olsen et al., 2010; Masiero et al., 2015). Another major application of lidar intensity is the field of land cover classification. Early work by Song et al. (2002) along with Charaniya et al. (2004), indicated that intensity was able to differentiate between land cover surfaces including buildings, trees, roads, and grass. These discoveries have continued to be built upon, with Im et al. (2008) showing that the incorporation of intensity leads to increased classification accuracy in urban areas. Zhou et al. (2009) present the benefits of classification with lidar over aerial photos, especially in shaded regions. Based on this work among others, a robust land cover classification scheme is often now one of the first data products produced by ALS scans.

1.3.1 Lidar and Planetary Science

While the majority of laser scanning has occurred in the lower atmosphere, lidar has also been utilized outside of Earth, both as a docking aid on the International Space Station (Allen et al., 2008) and for atmospheric measurements on the Phoenix rover on Mars (Whiteway et al., 2008). The Phoenix Mars Lander was the first mission to land in the Arctic region of Mars, and also the first time Canada as a nation landed on the planet. The Canadian Space Agency contributed a meteorological station with a suite of instruments—including a lidar sensor—that measured the atmospheric conditions of Mars. This was the first time a lidar instrument was utilized on the surface of another planet, with the goal of measuring the height profile from airborne dust and clouds in the Martian atmosphere (Whiteway et al., 2008). This lidar instrument operated at 532 nm and 1064 nm, having a maximum range of 20 km, with the backscattered signals being collected by a reflective telescope and recorded (Whiteway et al., 2008). The results collected from this instrument were extremely promising, recording the first evidence of ice crystal precipitation on Mars (Fig. 1.4), and confirming the hypothesis that precipitation of ice crystals is an important factor for the exchange of water between the atmosphere and the surface (Whiteway et al., 2009; Dickinson et al., 2010). This successful utilization of lidar on the surface of Mars provides evidence that the instrumentation is viable at extreme temperatures and conditions. Another key use of lidar in planetary science has been laser altimetry, which has been used to generate both topographic and intensity datasets at 1064 nm for Mars (MOLA) (Smith et al., 2001), the Moon (LOLA) (Lucey et al., 2014), and Mercury (MLA) (Neumann et al., 2013), respectively.

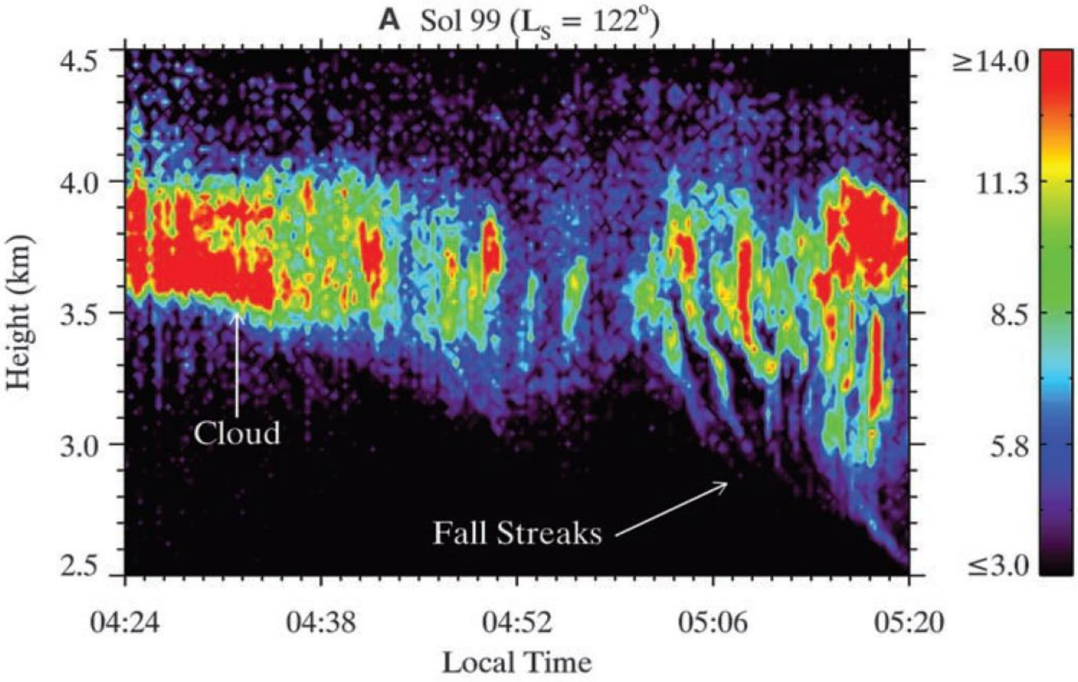

Figure 1.4. Contour plot of the backscatter coefficient at 532nm derived from the lidar instrument on the Phoenix Mars Lander on Sol 99. The fall streaks are indicative of precipitation (from Whiteway, et al., 2009).

NASA considers lidar to be a key technology for space exploration in the coming decades (National Aeronautics and Space Administration, 2015). In conjunction with this, research has recently been performed at a Mars analogue site in Utah exhibiting the multiple benefits of rover-based lidar for future planetary exploration (Osinski et al., 2016; Zylberman et al., 2016). This analogue mission demonstrates how lidar could have a key role in navigation and hazard awareness on future rover-based planetary missions. Due to the ability to collect extremely detailed surface maps of materials, Zylberman et al. (2016) note that the data from the lidar instrument may also be able to provide vital scientific information, especially at distances where contact science instruments cannot reach.

1.3.2 Geological Applications

Lidar scanning of natural environments has arguably been one of the largest applications in this field in the past decade. For example, intensity data has been utilized as a remote sensing tool for: biomass assessment in forestry (Antonarakis et al., 2008; Barnea and Filin, 2012; Cook et al., 2013); identifying ruins in geoarchaeology (Challis et al., 2011); discrimination between snow and glacial ice in glaciology (Lutz et al., 2003; Arnold et al., 2006); discriminating different ages of volcanic flows (Mazzarini et al., 2007; Pesci et al., 2008); differentiating sand and gravel lithofacies in hydrology (Klise et al., 2009); and high resolution scanning of hemipelagic successions in outcrops for cyclostratigraphy (Franceschi et al., 2011) .

Terrestrial laser scanning is rapidly becoming the geologist's new favourite tool for rock characterization and analysis on outcrops, especially those that are inaccessible or difficult to reach. Rapid data collection of study areas in 3D with high resolution and accuracy has led to the TLS becoming widely disseminated in the earth sciences. The development of digital outcrop models has been a boon to the petroleum sector, which has benefited from the collection of accurate spatial information which aid in distinguishing geological heterogeneity, allowing for improved modelling of subsurface reservoirs (Rarity et al., 2013). These digital outcrop models also provide the researcher with the ability to attain accurate strike and dip measurements, which are extremely valuable, especially when the outcrop is inaccessible (Bellian, 2005; Buckley et al., 2008; Rarity et al., 2013; Matasci et al., 2015).

Several studies have assessed the application of lidar to planetary science and geology, with promising results (Berinstain et al., 2003; Osinski et al., 2010). Initial work with an early prototype of Optech's ILRIS TLS at the Haughton impact structure, Devon Island, Canada led to the conclusion that there is high value in the collection of 3-D spatial information on ejecta blocks and impact-generated rock formations (Berinstain et al., 2003). This 3D record of the environment can be used to make precise measurements of features of interest even after physically leaving the field. Berinstain et al. (2003) also observed differing intensity values between two lithologies, with the dark drown gypsum clasts having a lower intensity compared to the light grey impact melt breccia matrix.

Further lidar research was completed at Haughton by Osinski et al. (2010), concluding that there is a high potential for lidar being utilized as both a navigational and scientific tool for future planetary missions. The ability to collect up to months' worth of manual surveying data in 45 minutes of lidar scanning allows for the geologist to focus on operations that can only be completed while on site, such as sample collection. Osinski et al. (2010) note the ability to discern detailed structural information in outcrops that are not present in passive visible photography. The authors conclude that there appears to be a strong potential to link composition of the impactites to the intensity response, which could have implications for automated analysis and differentiation of lithologies in impact craters on other planetary bodies (Osinski et al., 2010).

Another application with wide ranging implications is the discrimination of rock properties at outcrop faces with TLS; which often could not be scanned from the air due to its extreme incidence angle. Using an example that was mentioned above, Pesci et al. (2008) used intensity data to map and differentiate between different lava flow facies exposed in the walls of the Vesuvius crater. These authors were also able to differentiate between block scoria and welded scoria, showing that intensity is firmly correlated to physical and chemical properties of the reflecting target (Pesci et al., 2008). Further support for this is provided by (Franceschi et al., 2009), who were able to link reflectance at a wavelength of 1535 nm (intensity) in an inverse linear relationship to hydrogen weight percent (clay content proxy) in a carbonate succession. Burton et al. (2011) studied a clastic succession of sandstones and mudstones, and were able to correlate distance normalized lidar intensity (at 1500 nm) in a log-linear inverse relationship with weight percent clay (shale proxy). The authors also correlated a positive log-linear relationship between the normalized intensity and weight percent combined quartz, potassium feldspar, and plagioclase (sandstone proxy). It was concluded that the majority of the variation in the normalized intensity response could be explained by the different mineralogical composition of the shales and sandstones (Burton et al., 2011). Matasci et al. (2015) were able to identify and differentiate nine lithologies at the Dents-du-Midi limestone massif in Switzerland by analyzing the corrected intensity values at 1064 nm. Finally, Campos Inocencio et al. (2014) were able to spectrally differentiate between basalt, gabbro, granite, and banded iron formation using corrected intensity (at 1535 nm) to classify the rocks into distinctive classes, although further work is required to advance from simple differentiation to being able to diagnostically characterize the lithologies. Most importantly, these authors were able to detect small changes in the physical-chemical characteristics of the rocks, specifically the iron oxide concentration within the cement of the sandstone (Campos Inocencio et al., 2014).

1.3.3 Data Fusion for Lithological Discrimination

Several authors have begun to utilize multiple sensors and integration of these datasets often achieve a greater accuracy when identifying and classifying objects. Due to the fact that lidar only operates at a single wavelength, it can be extremely beneficial to fuse datasets together to create multispectral feature spaces that can be used for classification of point clouds. Early work in this field showed that the extraction of trees and buildings from urban scenes were more accurate when using a four channel (red, blue, green, near infrared) feature space, as opposed to solely utilizing the lidar intensity data (Lichti, 2005; Barnea and Filin, 2012). The integration of passive visible imagery with lidar intensity was shown to help elucidate structurally complex geological areas, such as the Suez rift in Egypt (Wilson et al., 2009).

Data fusion has also begun in terrestrial lidar scans on outcrops in order to remotely differentiate lithologies. The recent application of multispectral lidar by Hartzell et al. (2014) led to the collection of intensity values at 532 nm (visible green), 785 nm (red), 1550 nm (near infrared), as well as passive imagery (RGB) for each point scanned from a rock outcrop. The authors concluded that fusing the 1550 nm band with the visible imagery was equivalent to fusing all three TLS intensity bands with passive imagery (Hartzell et al., 2014). This information may be beneficial to researchers who are attempting to decide which TLS instrument to utilize for their studies.

The capability to fuse hyperspectral imaging with lidar scans has also led to an enhanced analysis—both qualitatively and quantitatively—of digital outcrop models. Bellian et al. (2007) utilized airborne AVIRIS hyperspectral image data combined with airborne lidar scans to map limestone and dolostone over a large area in the Franklin Mountains, Texas. It should be noted that the pixel resolution for the AVIRIS data was 20 m per pixel, meaning that any lithological variations present at a scale smaller than that would not be recognized (Bellian et al., 2007). These airborne hyperspectral imagers also are in a scanning direction that is unsuitable for collecting information off of near-vertical faces, such as outcrops (Kurz et al., 2013). Close-range hyperspectral imaging can remedy this issue, and provides an increased spectral range along with enhanced resolution that is often able to differentiate subtle mineralogical and chemical changes present in an outcrop (Buckley et al., 2013; Kurz et al., 2013; Penasa et al., 2014). Close-range hyperspectral imagers are generally mounted on tripods, and often have the ability to rotate to collect panoramic data (Kurz et al., 2013). Buckley et al. (2013) were able to differentiate and classify dolomite from limestone after fusing and properly registering the lidar point cloud and the hyperspectral images.

1.4 Thematic Classification

The aim of digital image classification is to group each of the pixels present in an image to specific classes, which result in a thematic map. In the case of classification in a geological context, the goal is most often to differentiate the lithologies present in a given outcrop. This thematic classification can be achieved by grouping or classifying pixels together that share similar feature-space characteristics (Lichti, 2005). For TLS, this feature-space can be composed of four channels, which is achieved by fusing the RGB channels from passive imagery with the NIR channel from the corrected lidar intensity. There are other channels that could potentially be added to the feature-space, including range, texture, or a plethora of higher level derivatives (channel ratios, differences, etc.) of these previously mentioned channels can be utilized to further discriminate objects in an image (Lichti, 2005; Francis, 2014). Classification methods can be broken into supervised and unsupervised, and will be addressed below.

1.4.1 Supervised Classification

Supervised classification requires the researcher to provide the algorithm with a set of training data for each of the proposed classes. This training data is reference data, and can be aerial photos, geological maps of a region, or even actual rock samples from an outcrop; anything that can ground truth the area and ensure the correct classification of each object in the image (Richards, 2013). The training data is generally assessed to a subset (1-5%) of the entire image, thereafter which the classifier will attach classes to all of the pixels in the image. The final classified thematic map then will undergo an accuracy assessment, which produces an error matrix to indicate the residual error for each class (Richards, 2013). This final step of producing an accuracy assessment also occurs for unsupervised classification.

1.4.2 Unsupervised Classification

Unsupervised classification operates in the reverse order as supervised classification, where the classification occurs prior to any input or training by the researcher. This method aims to uncover structure or commonalities in the data without input. This is most often performed by clustering algorithms, which separate the image data into distinct clusters or classes based on commonalities within their feature-space (Richards, 2013). The researcher will then look at the thematic map and identify if any classes can be combined further, with the final goal of having only as many clusters as there are spectral classes in the image (Richards, 2013). Following this process, the researcher will perform a process of random sampling in order to assess the accuracy and validity of the classification. While there are many clustering algorithms available in the field of remote sensing, only the k-means clustering algorithm will be addressed here.

1.4.2.1 K-Means Clustering

The k-means clustering method is a commonly used and relatively simplistic algorithm that will iteratively assign data to a specified number (*k)* of classes input by the researcher. The initial cluster centres will be arbitrarily set and represented by the means of the pixel vectors allocated to them (Richards, 2013). These initial clusters will undergo multiple iterations of re-clustering based on the pixel vectors continuing to be reassigned to the nearest mean cluster. This process will repeat until there is no longer any further movement of pixels between clusters (Richards, 2013). The researcher will then assess these final clusters to confirm the validity of the classification and see if any classes need to be merged or broken into multiple classes. The final result should be a thematic map that has the initial *k* number of classes. For the geologist, these classes will most likely represent the different lithologies present in an outcrop. The last step is for the geologist to confirm the accuracy and validity of this clustering by perform a visual interpretation on the same image, using their training to visually differentiate the rock types, and then comparing it to the thematic map. For example, one study recently presented the application of a k-means classification method to corrected intensity (Campos Inocencio et al., 2014). These authors found that they were able to distinguish between sandstone, diamictite, and carbonaceous pelites in an outcrop by performing unsupervised classification using a single band (corrected near infrared intensity). As well, the authors note that it was possible to identify the presence of iron oxide cement in a sandstone outcrop, and classify it with high accuracy using the unsupervised k-means classification method (Campos Inocencio et al., 2014).

1.5 Introduction to the Thesis

In Chapter 2, we carried out a case study of an outcrop at the Tunnunik impact structure, Victoria Island, Arctic Canada, in which we perform unsupervised classification (via k-means clustering) on a fused dataset of NIR lidar intensity along with passive visible imagery to confirm the validity of using lidar as a remote sensor of lithology, especially in planetary analogue environments. X-Ray Diffraction analysis is also performed on samples collected within the scanned area, and are semi-quantitatively correlated with distance corrected intensity values. We discuss the relationship between intensity and lithology, potential misclassification factors of the technique, along with the future application of lidar for planetary missions.

In Chapter 3 we perform a case study of similar data fusion and classification in an underground environment at the Nickel Rim South mine, Sudbury, Canada. This study focuses on the novel approach of classification and differentiation of ore from host rock using k-means clustering on a 4-band fused dataset. We also discuss potential misclassification factors, effects of dust cover and moisture on the lidar intensity returns, and the applications for future utilization of lidar in mining.

Chapter 4 concludes the thesis and offers several possible avenues for the future of utilizing lidar intensity for geological applications.

1.6 References

Allen, A.C.M., Langley, C., Mukherji, R., Taylor, A.B., Umasuthan, M., and Barfoot, T.D., 2008, Rendezvous lidar sensor system for terminal rendezvous, capture, and berthing to the International Space Station (R. T. Howard & P. Motaghedi, Eds.): Proc. SPIE 6958, Sensors and Systems for Space Applications II, 69580S, v. 6958, p. 69580S–69580S–8, doi: 10.1117/12.777208.

Antonarakis, a. S., Richards, K.S., and Brasington, J., 2008, Object-based land cover classification using airborne LiDAR: Remote Sensing of Environment, v. 112, no. 6, p. 2988–2998, doi: 10.1016/j.rse.2008.02.004.

Arnold, N.S., Rees, W.G., Devereux, B.J., and Amable, G.S., 2006, Evaluating the potential of high-resolution airborne LiDAR data in glaciology: International Journal of Remote Sensing, v. 27, no. 6, p. 1233–1251, doi: 10.1080/01431160500353817.

ASPRS, 2016, LASer (LAS) File Format Exchange Activities. <https://www.asprs.org/committee-general/laser-las-file-format-exchange-activities.html> (accessed on 05.03.2016).

Barnea, S., and Filin, S., 2012, Extraction of objects from terrestrial laser scans by integrating geometry image and intensity data with demonstration on trees: Remote Sensing, v. 4, p. 88–110, doi: 10.3390/rs4010088.

Bellian, J. a., 2005, Digital Outcrop Models: Applications of Terrestrial Scanning Lidar Technology in Stratigraphic Modeling: Journal of Sedimentary Research, v. 75, no. 2, p. 166–176, doi: 10.2110/jsr.2005.013.

Bellian, J. a., Beck, R., and Kerans, C., 2007, Analysis of hyperspectral and lidar data: Remote optical mineralogy and fracture identification: Geosphere, v. 3, no. 6, p. 491–500, doi: 10.1130/GES00097.1.

Berinstain, A., Osinski, G., Spray, J., Lee, P., Hahn, J., and Ulitsky, A., 2003, Applications of time-of-flight lidar in crater geology, in Kamerman, G.W. ed., Laser Radar Technology and Applications VIII, Proceedings of the SPIE, p. 292–298.

Buckley, S.J., Howell, J. a., Enge, H.D., and Kurz, T.H., 2008, Terrestrial laser scanning in geology: data acquisition, processing and accuracy considerations: Journal of the Geological Society, v. 165, no. 3, p. 625–638, doi: 10.1144/0016-76492007-100.

Buckley, S.J., Kurz, T.H., Howell, J. a., and Schneider, D., 2013, Terrestrial lidar and hyperspectral data fusion products for geological outcrop analysis: Computers and Geosciences, v. 54, p. 249–258, doi: 10.1016/j.cageo.2013.01.018.

Burton, D., Dunlap, D.B., Wood, L.J., and Flaig, P.P., 2011, Lidar Intensity as a Remote Sensor of Rock Properties: Journal of Sedimentary Research, v. 81, no. 5, p. 339–347, doi: 10.2110/jsr.2011.31.

Campos Inocencio, L., Veronez, M.R., Wohnrath Tognoli, F.M., De Souza, M.K., Da Silva, R.M., Gonzaga, L., and Blum Silveira, C.L., 2014, Spectral pattern classification in lidar data for rock identification in outcrops: The Scientific World Journal, v. 2014, p. 1–10, doi: 10.1155/2014/539029.

Carrea, D., Abellan, A., Humair, F., Matasci, B., Derron, M.-H., and Jaboyedoff, M., 2016, Correction of terrestrial LiDAR intensity channel using Oren–Nayar reflectance model: An application to lithological differentiation: ISPRS Journal of Photogrammetry and Remote Sensing, v. 113, p. 17–29, doi: 10.1016/j.isprsjprs.2015.12.004.

Challis, K., Carey, C., Kincey, M., and Howard, A.J., 2011, Airborne lidar intensity and geoarchaeological prospection in river valley floors: Archaeological Prospection, v. 18, no. 1, p. 1–13, doi: 10.1002/arp.398.

Charaniya, A.P., Manduchi, R., and Lodha, S.K., 2004, Supervised Parametric Classification of Aerial LiDAR Data: IEEE Conference on Computer Vision and Pattern Recognition Workshop. CVPRW '04, p. 1–8, doi: 10.1109/CVPR.2004.172.

Cheng, L., Tong, L., Wu, Y., Chen, Y., and Li, M., 2015, Shiftable leading point method for high accuracy registration of airborne and terrestrial LiDAR data: Remote Sensing, v. 7, no. 2, p. 1915–1936, doi: 10.3390/rs70201915.

Chin, A., Olsen, M.J., Ph, D., and Asce, A.M., 2015, Evaluation of Technologies for Road Profile Capture, Analysis, and Evaluation: J. Surv. Eng., v. 141, no. 1, p. 1–13, doi: 10.1061/(ASCE)SU.1943-5428.0000134.

Clark, R.N., 1999, Spectroscopy of rocks and minerals, and principles of spectroscopy, Chapter 1. In: Rencz, A. (Ed.), Manual of Remote Sensing. John Wiley and Sons Inc, New York.

Cook, B.D., Corp, L. A., Nelson, R.F., Middleton, E.M., Morton, D.C., McCorkel, J.T., Masek, J.G., Ranson, K.J., Ly, V., and Montesano, P.M., 2013, NASA goddard's LiDAR, hyperspectral and thermal (G-LiHT) airborne imager: Remote Sensing, v. 5, p. 4045–4066, doi: 10.3390/rs5084045.

Dickinson, C., Whiteway, J. a., Komguem, L., Moores, J.E., and Lemmon, M.T., 2010, Lidar measurements of clouds in the planetary boundary layer on Mars: Geophysical Research Letters, v. 37, no. 18, doi: 10.1029/2010GL044317.

Franceschi, M., Preto, N., Hinnov, L. a., Huang, C., and Rusciadelli, G., 2011, Terrestrial laser scanner imaging reveals astronomical forcing in the Early Cretaceous of the Tethys realm: Earth and Planetary Science Letters, v. 305, no. 3-4, p. 359–370, doi: 10.1016/j.epsl.2011.03.017.

Franceschi, M., Teza, G., Preto, N., Pesci, A., Galgaro, A., and Girardi, S., 2009, Discrimination between marls and limestones using intensity data from terrestrial laser scanner: ISPRS Journal of Photogrammetry and Remote Sensing, v. 64, no. 6, p. 522–528, doi: 10.1016/j.isprsjprs.2009.03.003.

Francis, R., 2014, Automated Image Interpretation for Science Autonomy in Robotic Planetary Exploration: Ph. D. Dissertation, University of Western Ontario, London, p. 170.

Hartzell, P., Glennie, C., Biber, K., and Khan, S., 2014, Application of multispectral LiDAR to automated virtual outcrop geology: ISPRS Journal of Photogrammetry and Remote Sensing, v. 88, p. 147–155, doi: 10.1016/j.isprsjprs.2013.12.004.

Hartzell, P.J., Glennie, C.L., and Finnegan, D.C., 2013, Calibration of a Terrestrial Full Waveform Laser Scanner: ASPRS 2013 Annual Conference Proceedings, p. 7.

Höfle, B., and Pfeifer, N., 2007, Correction of laser scanning intensity data: Data and model-driven approaches: ISPRS Journal of Photogrammetry and Remote Sensing, v. 62, no. 6, p. 415–433, doi: 10.1016/j.isprsjprs.2007.05.008.

Im, J., Jensen, J.R., and Hodgson, M.E., 2008, Object-Based Land Cover Classification Using High-Posting-Density LiDAR Data: GIScience & Remote Sensing, v. 45, no. 2, p. 209–228, doi: 10.2747/1548-1603.45.2.209.

Jelalian, A.V., 1992, Laser Radar Systems. Artech House, Boston London.

Jensen, J.R., 2007, Remote sensing of the environment: An earth resource perspective (2nd edition). Prentice Hall, Upper Saddle River, NJ.

Jutzi, B., and Gross, H., 2009, Normalization of Lidar Intensity Data Based on Range and Surface Incidence Angle: The International Archives of the Photogrammetry, Remote Sensing and Spatial Information Sciences 38 (Part 3/W8), v. XXXVIII, no. 2006, p. 213–218.

Kaasalainen, S., Hyyppä, H., Kukko, A., Litkey, P., Ahokas, E., Hyyppä, J., Lehner, H., Jaakkola, A., Suomalainen, J., Akujärvi, A., Kaasalainen, M., and Pyysalo, U., 2009, Radiometric calibration of LIDAR intensity with commercially available reference targets: IEEE Transactions on Geoscience and Remote Sensing, v. 47, no. 2, p. 588–598.

Kaasalainen, S., Jaakkola, A., Kaasalainen, M., Krooks, A., and Kukko, A., 2011, Analysis of incidence angle and distance effects on terrestrial laser scanner intensity: Search for correction methods: Remote Sensing, v. 3, p. 2207–2221, doi: 10.3390/rs3102207.

Kaasalainen, M., and Kaasalainen, S., 2008, Aperture size effects on backscatter intensity measurements in Earth and space remote sensing: Journal of the Optical Society of America. A, Optics, image science, and vision, v. 25, no. 5, p. 1142–1146, doi: 10.1364/JOSAA.25.001142.

Kaasalainen, S., Kukko, A., Lindroos, T., Litkey, P., Kaartinen, H., Hyyppä, J., and Ahokas, E., 2008, Brightness measurements and calibration with airborne and terrestrial laser scanners: IEEE Transactions on Geoscience and Remote Sensing, v. 46, no. 2, p. 528–533.

Kashani, A.G., Olsen, M.J., Parrish, C.E., and Wilson, N., 2015, A review of LIDAR radiometric processing: From ad hoc intensity correction to rigorous radiometric calibration: Sensors (Switzerland), v. 15, no. 11, p. 28099–28128, doi: 10.3390/s151128099.

Kemp, K.K., 2008, Encyclopedia of geographic information science: Reference User Services Quarterly, v. 48, no. 1, p. xxv, 558 p., doi: 10.4135/9781412953962.

Krooks, a., Kaasalainen, S., Hakala, T., and Nevalainen, O., 2013, Correction of Intensity Incidence Angle Effect in Terrestrial Laser Scanning: Annals of Photogrammetry, Remote Sensing and Spatial Information Sciences, v. II-5/W2, no. June 2015, p. 145–150, doi: 10.5194/isprsannals-II-5-W2-145-2013.

Kurz, T.H., Buckley, S.J., and Howell, J. a, 2013, Close-range hyperspectral imaging for geological field studies: workflow and methods: International Journal of Remote Sensing, v. 34, no. 5, p. 1798–1822, doi: 10.1080/01431161.2012.727039.

Lichti, D., 2005, Spectral filtering and classification of terrestrial laser scanner point clouds: The Photogrammetric Record, v. 20, no. September, p. 218–240.

Lucey, P.G., Neumann, G.A., Riner, M.A., Mazarico, E., Smith, D.E., Zuber, M.T., Paige, D.A., Bussey, D.B., Cahill, J.T., McGovern, A., Isaacson, P., Corley, L.M., Torrence, M.H., Melosh, H.J., et al., 2014, The global albedo of the Moon at 1064 nm from LOLA: Journal of Geophysical Research: Planets, v. 119, no. 7, p. 1665–1679, doi: 10.1002/2013JE004592.

Lutz, E., Geist, T., and Stötter, J., 2003, Investigations of airborne laser scanning signal intensity on glacial surfaces – Utilizing comprehensive laser geometry modelling and orthophoto surface modelling (A case study: Svartisheibreen, Norway): International Archives of Photogrammetry, Remote Sensing and Spatial Information Sciences, v. 34, no. Part 3, p. 143–148.

Masiero, a., Guarnieri, a., Pirotti, F., and Vettore, a., 2015, Semi-automated detection of surface degradation on bridges based on a level set method: International Archives of the Photogrammetry, Remote Sensing and Spatial Information Sciences - ISPRS Archives, v. 40, no. 3W3, p. 15–21, doi: 10.5194/isprsarchives-XL-3-W3-15-2015.

Matasci, B., Carrea, D., Abellan, A., Derron, M.H., Humair, F., Jaboyedoff, M., and Metzger, R., 2015, Geological mapping and fold modeling using terrestrial laser scanning point clouds: Application to the Dents-du-Midi limestone massif (Switzerland): European Journal of Remote Sensing, v. 48, p. 569–591, doi: 10.5721/EuJRS20154832.

Mazzarini, F., Pareschi, M.T., Favalli, M., Isola, I., Tarquini, S., and Boschi, E., 2007, Lava flow identification and aging by means of lidar intensity: Mount Etna case: Journal of Geophysical Research, v. 112, no. B2, p. B02201, doi: 10.1029/2005JB004166.

Mills, G., and Fotopoulos, G., 2013, On the estimation of geological surface roughness from terrestrial laser scanner point clouds: Geosphere, v. 9, no. 5, p. 1410–1416, doi: 10.1130/GES00918.1.

National Aeronautics and Space Administration, 2015, NASA Technology Roadmaps TA 8: Science Instruments, Observatories, and Sensor Systems: NASA Technology Roadmaps, no. July, p. 115.

Neumann, G.A, Cavanaugh, J.F., Sun, X., Mazarico, E.M., Smith, D.E., Zuber, M.T., Mao, D., Paige, D.A, Solomon, S.C., Ernst, C.M., and Barnouin, O.S., 2013, Bright and Dark Polar Deposits on Mercury: Evidence for Surface Volatiles: Science, v. 339, no. 6117, p. 296–300, doi: 10.1126/science.1229764.

Olsen, M.J., Chen, Z., Hutchinson, T., and Kuester, F., 2013, Optical techniques for multiscale damage assessment: Geomatics, Natural Hazards and Risk, v. 4, no. 1, p. 49–70, doi: 10.1080/19475705.2012.670668.

Olsen, M.J., Kuester, F., Chang, B.J., and Hutchinson, T.C., 2010, Terrestrial Laser Scanning-Based Structural Damage Assessment: Journal of Computing in Civil Engineering, v. 24, no. 3, p. 264–272, doi: 10.1061/(ASCE)CP.1943-5487.0000028.

Osinski, G.R., Barfoot, T.D., Ghafoor, N., Izawa, M., Banerjee, N., Jasiobedzki, P., Tripp, J., Richards, R., Auclair, S., Sapers, H., Thomson, L., and Flemming, R., 2010, Lidar and the mobile Scene Modeler (mSM) as scientific tools for planetary exploration: Planetary and Space Science, v. 58, no. 4, p. 691–700, doi: 10.1016/j.pss.2009.08.004.

Osinski, G.R., Francis, R., Fulford, P., Haltigin, T., Kerrigan, M., Pontefract, A., Silber, E.A., Tornabene, L.L., and Team, 2015 CanMars, 2016, Overview of the 2015 CanMars Mars Sample Return Analogue Mission, in 47th Lunar and Planetary Science Conference, Houston, Texas.

Penasa, L., Franceschi, M., Preto, N., Teza, G., and Polito, V., 2014, Integration of intensity textures and local geometry descriptors from Terrestrial Laser Scanning to map chert in outcrops: ISPRS Journal of Photogrammetry and Remote Sensing, v. 93, p. 88–97, doi: 10.1016/j.isprsjprs.2014.04.003.

Pesci, A., and Teza, G., 2008, Effects of surface irregularities on intensity data from laser scanning: An experimental approach: Annals of Geophysics, v. 51, no. 5-6, p. 839–848, doi: 10.4401/ag-4462.

Pesci, A., Teza, G., and Ventura, G., 2008, Remote sensing of volcanic terrains by terrestrial laser scanner: preliminary reflectance and RGB implications for studying Vesuvius crater (Italy): Annals of Geophysics, v. 51, no. 4, p. 633–653, doi: 10.4401/ag-4455.

Pfeifer, N., Dorninger, P., Haring, A., and Fan, H., 2007, Investigating terrestrial laser scanning intensity data: Quality and functional relations: 8th Conference on Optical 3-D Measurement Techniques, p. 328–337.

Pfeifer, N., Höfle, B., Briese, C., Rutzinger, M., and Haring, A., 2008, Analysis of the backscattered energy in terrestrial laser scanning data: Int. Arch. Photogramm. Remote Sens. Spat. Inf. Sci., v. 37, p. 1045–1052.

Pfeifer, N. and Briese, C., 2007, Geometrical aspects of airborne laser scanning and terrestrial laser scanning: International Archives of Photogrammetry, Remote Sensing and Spatial Information Sciences, v. XXXVI, p. 311–319.

Rarity, F., van Lanen, X.M.T., Hodgetts, D., Gawthorpe, R.L., Wilson, P., Fabuel-Perez, I., and Redfern, J., 2013, LiDAR-based digital outcrops for sedimentological analysis: workflows and techniques: Geological Society, London, Special Publications, v. 387, no. 1, p. 153–183, doi: 10.1144/SP387.5.

Reshetyuk, Y., 2006, Investigation of the Influence of Surface Reflectance on the Measurementswith the Terrestrial Laser Scanner Leica HDS 3000: Zeitschrift für Vermessungswesen, v. 2, p. 96–103.

Richards, J. A., 2013, Remote Sensing Digital Image Analysis: An Introduction (5th ed). Springer.

Song, J.H., Han, S.H., Yu, K.Y., and Kim, Y.I., 2002, Assessing the possibility of land-cover classification using lidar intensity data: International Archives of Photogrammetry, Remote Sensing and Spatial Information Sciences, v. 34, p. 259–263.

Smith, D.E., Zuber, M.T., Frey, H. V., Garvin, J.B., Head, J.W., Muhleman, D.O., Pettengill, G.H., Phillips, R.J., Solomon, S.C., Zwally, H.J., Banerdt, W.B., Duxbury, T.C., Golombek, M.P., Lemoine, F.G., et al., 2001, Mars Orbiter Laser Altimeter: Experiment summary after the first year of global mapping of Mars: Journal of Geophysical Research: Planets, v. 106, no. E10, p. 23689–23722, doi: 10.1029/2000JE001364.

Wagner, W., Ullrich, A., Ducic, V., Melzer, T., and Studnicka, N., 2006, Gaussian decomposition and calibration of a novel small-footprint full-waveform digitising airborne laser scanner: ISPRS Journal of Photogrammetry and Remote Sensing, v. 60, no. 2, p. 100–112, doi: 10.1016/j.isprsjprs.2005.12.001.

Whiteway, J., Daly, M., Carswell, A., Duck, T., Dickinson, C., Komguem, L., and Cook, C., 2008, Lidar on the Phoenix mission to Mars: Journal of Geophysical Research, v. 113, no. 3, p. E00A08, doi: 10.1029/2007JE003002.

Whiteway, J., Komguem, L., Dickinson, C., Cook, C., Illnicki, M., Seabrook, J., Popovici, V., Duck, T.J., Davy, R., Taylor, P. a, Pathak, J., Fisher, D., Carswell, a I., Daly, M., et al., 2009, Mars Water-Ice Clouds and Precipitation: Science, v. 325, no. 5936, p. 68–70, doi: 10.1126/science.1172344.

Wilson, P., Hodgetts, D., Rarity, F., Gawthorpe, R.L., and Sharp, I.R., 2009, Structural geology and 4D evolution of a half-graben: New digital outcrop modelling techniques applied to the Nukhul half-graben, Suez rift, Egypt: Journal of Structural Geology, v. 31, no. 3, p. 328–345, doi: 10.1016/j.jsg.2008.11.013.

Yan, W.Y., Shaker, A., Habib, A., and Kersting, A.P., 2012, Improving classification accuracy of airborne LiDAR intensity data by geometric calibration and radiometric correction: ISPRS Journal of Photogrammetry and Remote Sensing, v. 67, no. 1, p. 35–44, doi: 10.1016/j.isprsjprs.2011.10.005.

Zhou, W., Huang, G., Troy, A., and Cadenasso, M.L., 2009, Object-based land cover classification of shaded areas in high spatial resolution imagery of urban areas: A comparison study: Remote Sensing of Environment, v. 113, no. 8, p. 1769–1777, doi: 10.1016/j.rse.2009.04.007.

Zylberman, W., Hickson, D., Haid, T., and Osinski, G.R., 2016, 2015 CanMars MSR Analogue Mission: The Key Role of LiDAR in Rover Navigation and Potential for Future Missions, in 47th Lunar and Planetary Science Conference, Houston, Texas.

Chapter 2

2 Integration of passive visible imagery with terrestrial lidar intensity data for geological mapping and characterization: A case study of the Tunnunik impact structure, Victoria Island, Canada

2.1 Introduction

While lidar has been historically used for generating digital terrain maps and as a navigation tool, recent research shows lidar has many potential scientific applications, including high resolution analysis of geological outcrops for differentiation of materials (Pesci et al., 2008; Franceschi et al., 2009; Osinski et al., 2010; Burton et al., 2011; Campos Inocencio et al., 2014; Hartzell et al., 2014). Terrestrial lidar scanners have several benefits over typical cameras, including the collection of intensity data, which is a measure of the backscattered energy reflected off the target relative to the initial pulse, and the ability to collect data without the need for ambient light (Höfle and Pfeifer, 2007), which means they can be used in poorly lit environments.

Lidar uses the time-of-flight principle and angle of emission to measure ranges via laser pulses—in the near infrared between 500 nm and 1550 nm—to objects with extremely high accuracy (Jensen, 2007; Pfeifer and Briese, 2007). The receiver can collect hundreds of thousands of points per second, with each point containing specific x, y, and z coordinates that can be attributed to a precise point on the object or surface that is being scanned. Besides providing detailed spatial information, lidar instruments also record the intensity of the returned laser pulse. This intensity is a measure of the backscattered energy reflected off the target relative to the energy of the initial pulse (at the wavelength of the laser) (Jelalian, 1992), which generally is scaled to 8, 12, or 16-bit dynamic range and can be included as a parameter in the point cloud (Höfle and Pfeifer, 2007; Kashani et al., 2015). The goal of many studies that utilize lidar for outcrop analysis is to identify and differentiate the lithologies present, which requires knowledge of the absolute reflectance of the target material. This necessitates the need to correct the intensity return prior to analysis to remove extraneous factors such as range, incidence angle, surface roughness and atmospheric effects. Many correction methods for intensity have been proposed (Pesci et al., 2008; Franceschi et al., 2009; Kaasalainen et al., 2011; Penasa et al., 2014; Carrea et al., 2016), but a standardized method for all Terrestrial Laser Systems (TLS) still does not exist. Currently, the correction method to utilize will be situational, depending on the influence of the factors mentioned above. As different rock types will return a different intensity response, the corrected intensity can then be compared to the target composition, thus acting as a remote sensor of lithology. Several previous studies have been performed using corrected lidar intensity to differentiate between sandstones and shale (Burton et al., 2011), limestones from marls (Franceschi et al., 2009), and shales, marlstones, and limestones in a limestone massif (Matasci et al., 2015). For example, as seen in Figure 2.1, there is a large spectral difference in the reflectivity of dolostone and calcareous shale in the NIR (Baldridge et al., 2009). If there is a significant mineralogical difference between the dolostone and shale in an outcrop, it should be differentiable via the lidar intensity response, especially at the 1535 nm wavelength of the instrument used in this study. Besides purely discriminating between the rock types, Franceschi et al. (2009) were able to link reflectance in an inverse linear relationship to hydrogen weight percent—as a proxy for clay content—in a carbonate succession. Burton et al. (2011) studied a clastic succession of sandstones and mudstones, and were able to correlate distance normalized lidar intensity in a log-linear inverse relationship with weight percent clay (shale proxy), and a positive log-linear relationship between the normalized intensity and weight percent combined quartz, potassium feldspar, and plagioclase (sandstone proxy).

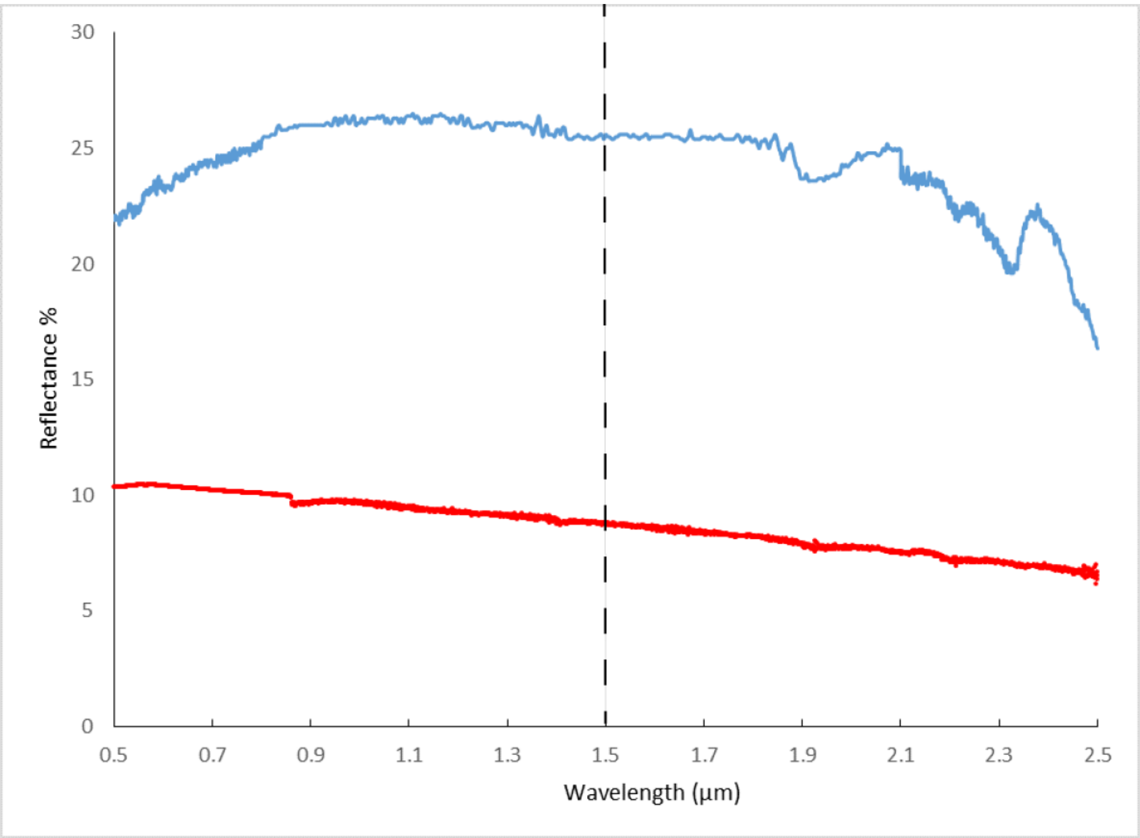

Figure 2.1. Plot showing an example of solid sample spectra data for dolostone (blue) and shale (red). The dashed vertical line indicates the wavelength the Optech ILRIS terrestrial lidar operates in. Note the spectral separability between the two lithologies at 1.5 µm. Figure plotted with data from Baldridge et al. (2009).

Lidar point clouds can also be fused with the red, green, and blue (RGB) colour patterns obtained by photographs captured by either an internal or externally mounted camera, which has led to innovations for multispectral analysis of materials (Hartzell et al., 2014). This data fusion between lidar intensity and passive visible imagery has successfully led to the differentiation and supervised classification of sandstone and limestone in an outcrop (Hartzell et al., 2014). For these reasons, lidar is becoming an ideal candidate for high fidelity image classification, especially for geological applications such as remote outcrop analysis.

This study builds upon previous research by conducting unsupervised classification via k-means clustering of a rock outcrop at the Tunnunik impact structure, Canadian High

Arctic, by fusing high-resolution lidar intensity data with passive visible imagery for the remote discrimination of distinct lithological units. Rock samples of each lithology were also collected and analyzed via X-ray Diffraction in order to assess the relationship between mineralogy and corrected intensity.

The goal of this study is to: a) ascertain if mineralogy of materials can be correlated with corrected intensity at the near infrared wavelength of the lidar instrument; and b) determine the viability of remotely identifying and discriminating lithologies through the fusion of corrected lidar intensity and passive visible imagery. Application of an unsupervised classification technique (k-means clustering) is demonstrated on the dataset, establishing a thematic map of the outcrop that differentiates the lithologies present. The accuracy and effectiveness of the classification will be assessed and the benefits and limitations of this method are discussed. Finally, because lidar has been proposed for future planetary exploration robotic missions, the fidelity of utilizing such data as a remote sensor of lithology in planetary analogues is discussed.

2.2 Study Area

Lidar scans were acquired at the Tunnunik impact structure during the summer of 2015. As indicated in Figure 2.2, the Tunnunik impact structure is located on the Prince Albert Peninsula (south of the Richard Collinson Inlet), NW Victoria Island, Canada (72° 28′ N, 113° 58′ W) (Dewing et al., 2013). This impact structure was recently identified by (Dewing et al., 2013) after the identification of shatter cones along with steeply dipping central strata and radial faulting patterns. This initial study was followed up by an expedition in 2012, which confirmed the impact origin of Tunnunik through confirmation of shatter cones, the identification of planar deformation features in quartz, along with the discovery of allochthonous impactites (Osinski et al., 2013). This expedition was followed by a larger mission to perform a detailed study of the impact crater in the summer of 2015, which included detailed geological mapping, geophysical and paleomagnetic surveys, along with lidar scans of many areas of interest within the crater.

This 28-km deeply eroded impact structure formed within Neoproterozoic and lower Paleozoic carbonate and sedimentary rocks. While the majority of the impact structure is now overlain by glacial sediments, excellent exposure of the impact-induced steeply dipping strata is present in a canyon that has been carved through the crater. The focus of the lidar scans occurred at the entrance to this canyon (Fig. 2.3), where there are spectacular exposures of several different lithologies within a small area. These units are made up of alternating successions of dolostone and shale.

Figure 2.2. Landsat image with regional context of the study area. Tunnunik impact structure indicated by the red star (from Google Earth, 2016).

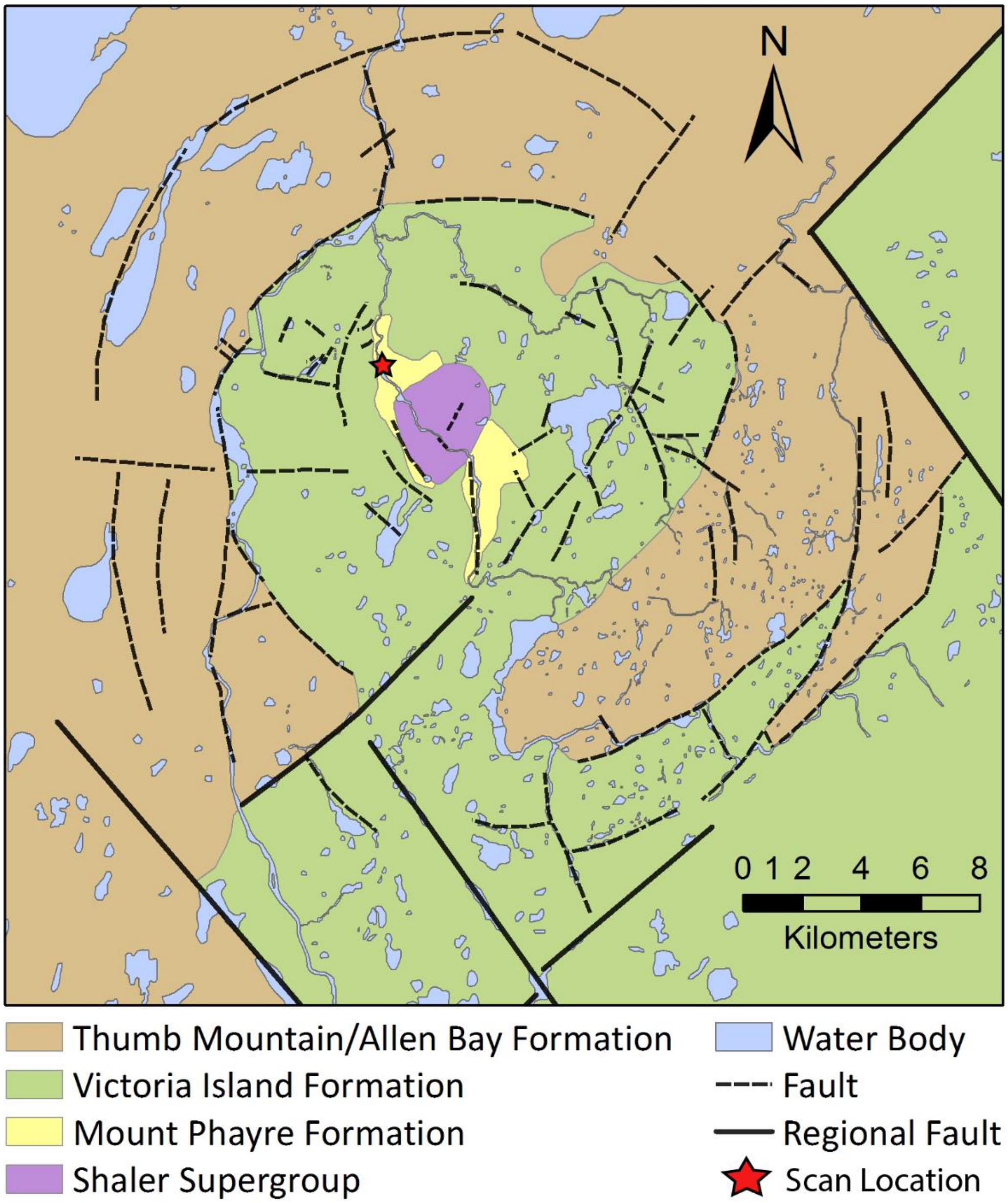

Figure 2.3. Geological map of the Tunnunik impact structure, Victoria Island, NWT, Arctic Canada. Lidar scan location indicated by red star (after Newman, 2016).

2.3 Methods

2.3.1 Instrumentation

The lidar scans for this study were acquired with the Optech ILRIS (Intelligent Laser Ranging and Imaging System) 3D laser scanner, which operates in the NIR at a wavelength of 1535 nm. The main specifications are shown in Table 2.1. This sensor is field portable and also comes with a pan-tilt unit for panoramic data acquisition, which is mounted on a tripod for operations (Fig. 2.4). The ILRIS can be powered by a portable battery pack, but due to the long duration of the scans, a portable gas generator was used to supply power. The instrument is controlled by Optech software—sending information from the field laptop via Ethernet cable—which allows the user to pan and tilt the instrument to achieve the optimal viewing position to collect scan data. The field of view is 40º x 40º, and regions of interest (ROI) can be chosen from targets within this field of view. Once the ROI has been set, parameters such as spot spacing and angular resolution can be adjusted, followed by the scan acquisition. A digital single-lens reflex (DSLR) camera was mounted to the top of the ILRIS, which allowed for registration of the photo and corresponding lidar scan. The camera used was a Canon EOS Rebel XTi with an 18-55 mm lens, and 10.1-megapixel resolution.

2.3.2 Data and Sample Collection

An outcrop with excellent exposure of impacted and near vertical lithologies near the southern edge of a canyon within the Tunnunik impact structure was chosen as the location to perform high resolution scans with the ILRIS (Fig. 2.5). The scan was acquired on a clear, sunny day with negligible humidity. From left to right, these steeply dipping units (~70º) are composed of ~10–30 cm-thick tan carbonate units; 1.5 m of thin, shaley alternating dark grey and tan beds; 1 m of very thinly bedded and shaley dark grey unit; 0.5 m of extremely friable and shaley grey to light grey material; 0.7 m thick tan carbonate unit; 0.3 m thin alternating and shaley dark grey and tan beds (as above); 0.3 m tan carbonate unit; and finally 1 m of alternating shaley and friable green and red material. Shatter cones were present throughout these units. Two ground control points were also incorporated in the scan for later georeferencing, but were masked for the subsequent classification.

Table 1.1. Main technical specifications of the Optech ILRIS 3D terrestrial laser scanner (Optech, 2016).

Parameter	**Unit**	
Wavelength	nm	1535
Laser Class		1 (eyesafe)
Range (80% target reflectivity)	m	1250
Range (10% target reflectivity)	m	400
Minimum acquisition distance	m	3
Laser beam divergence	mrad	0.15
Laser beam divergence at 50 m	mm	21
Acquisition accuracy at 50 m	mm	7
Minimum spot spacing at 50 m	mm	1.3

Figure 2.4. Image of the Optech ILRIS 3D laser scanner used to perform data acquisition at the Tunnunik impact structure.

.

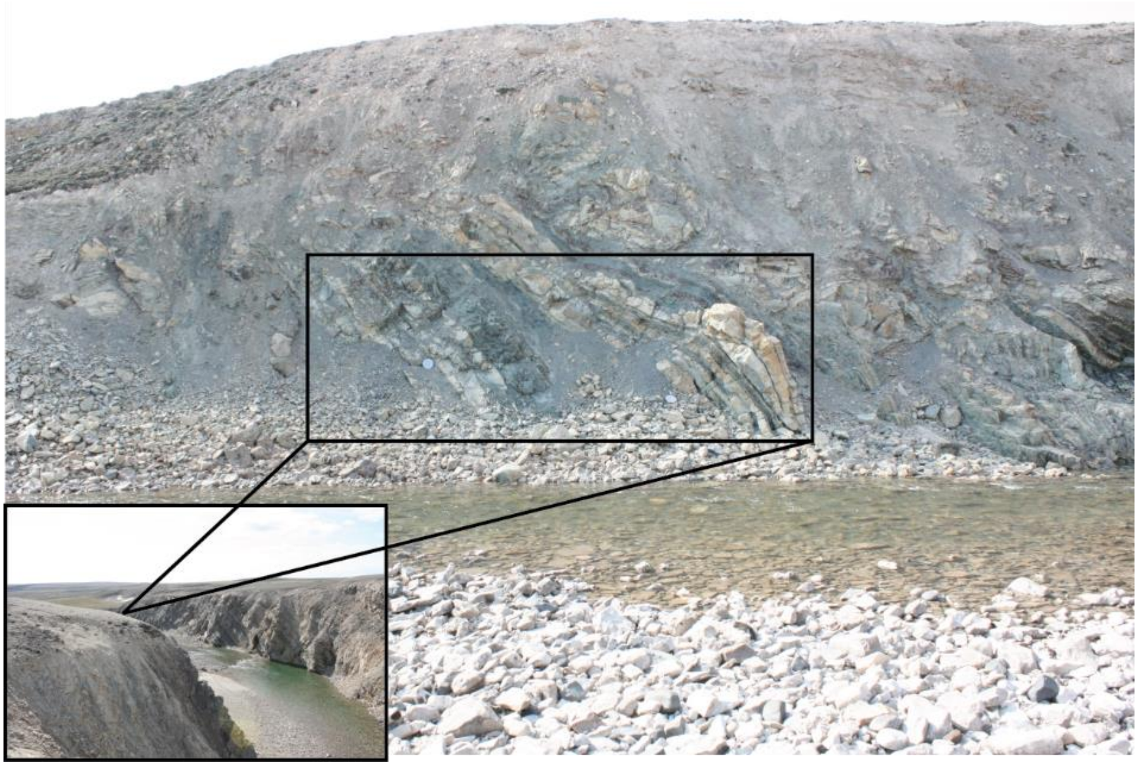

Figure 2.5. Canyon wall chosen for lidar scanning. Area of point cloud analyzed is indicated by the black rectangular box. Dimensions of the box are 15m x 5m. Lithologies present include dolostone, dark grey shale, green shale, and red shale. Inset: View of canyon looking south.

To acquire the high resolution data used in this study, a scan of the canyon wall was performed from a distance of ~30 m, with a point spacing of 1.3 mm. The scan was performed to ensure that the outcrop face was perpendicular to the scanner so as to reduce effects of incidence angle. The data acquired was initially stored in an Optech proprietary file format, which was later parsed into an ASCII format. The scanned area used for analysis was 15 m x 5 m, and had a total of 28,067,939 points collected. A digital camera was mounted on top of the scanner, and corresponding passive visible images were captured.

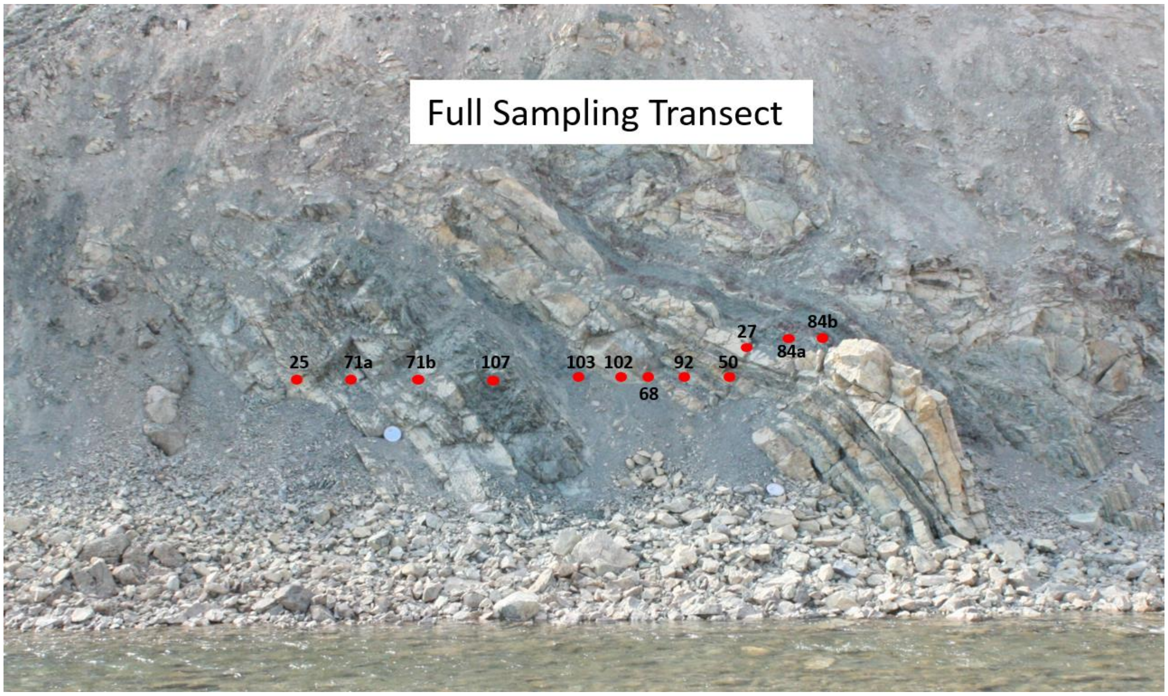

Figure 2.6. Full sampling transect across scanned outcrop. Red dots indicate location of sample collection, with the number allocating the RFID tag associated with each collected sample.

2.3.3 Sample characterization via X-Ray Diffraction

Following the completion of the scans, a total of 12 samples were taken for reference (Fig. 2.6) and follow up mineralogical analysis. Analysis of the 12 samples was carried out by powder X-ray Diffraction (XRD) to establish semi-quantitative mineralogy that could be compared to the lidar intensity returns. Samples were ground to a fine powder using a mortar and pestle and then back-packed into powder mounts in order to achieve maximum randomness in crystal orientation. These mounts were subsequently loaded into the Rigaku DMAX Geigerflex powder diffractometer in the X-Ray Diffraction and Microdiffraction Laboratory in the Department of Earth Sciences, Western University. X-ray diffraction data were collected from 10º to 90º 2θ, with Co Kα radiation (λ = 1.79021 Å), 0.02º step size, 66 min total counting time, at 40 kV accelerating voltage and 35 mA beam current. The resulting XRD patterns were analyzed with the Bruker-AXS EVA software package, with the International Center for Diffraction Data database as the reference data (BrukerAXS, 2005).

2.3.4 Intensity Pre-processing

The utilization of Optech's parsing software transforms the raw data into file formats that can be managed and visualized by open source point cloud software analysis programs, such as CloudCompare (Girardeau-Monteaut, 2016). Intensities were exported using the "8-bit scaled" option as a XYZ ASCII format. The parser converts the raw data into a point cloud with the set $\{(x_k, y_k, z_k, I_n (x_k, y_k, z_k)) \; k = 1, 2, \ldots N\}$ where $I_n (x_k, y_k, z_k)$ is an 8-bit digital number which represents the distance-corrected intensity normalized to the range 0-255, and N is the number of points where the intensity is useful (for example, the parser will remove extraneous returns that saturate the receiver). It is generally understood that raw intensity is a function of the inverse range square ($1/R^2$) (Wagner et al., 2006; Höfle and Pfeifer, 2007; Pesci et al., 2008; Krooks et al., 2013). This range correction is applied to produce similar intensity values for the same material at different distances. The Optech parser converts the raw intensity to the distance-corrected intensity in three steps:

1) The shot intensity is pre adjusted according to its range via $I_p = I_r * (d_k / d_r)^2$ where I_p is the preadjusted intensity, I_r is the raw intensity in the dat/i3d file, d_k is the shot range, and d_r is a reference distance that can be adjusted in the parser settings. For this study the reference distance was 30 m.

2) Outliers are trimmed from the preadjusted intensities by finding the upper limit (UL), below which there are 95% of all shots.

3) The preadjusted intensities are scaled to 0-255 via $I_n = 255*(I_p / UL)$ where I_n is the distance-corrected normalized intensity.

Aside from the effects of range on the intensity return, there are also effects from incidence angle, surface roughness of the target, and the atmosphere, which can influence the intensity return depending on the environment in which the scans are occurring. As noted by Hartzell et al. (2014), the effect of incidence angle generally only has a significant effect on the intensity return when the angle exceeds 20º. Several authors have noted that natural extended surfaces such as rocks in an outcrop, are usually characterized by roughness that is comparable to the diameter of the laser beam and, as such, intensity does not depend on incidence angle due to the fact that a significant part of the target illuminated by the laser will always be oriented toward the sensor (Pesci et al., 2008; Franceschi et al., 2009; Hartzell et al., 2014; Penasa et al., 2014). Hartzell et al. (2014) actually found a decrease in classification accuracy when incorporating the incidence angle of the outcrop with respect to the instrument, leading to the conclusion that the intensity return is independent of incidence angle for surfaces with roughness values that are generally found in outcrops. Regarding the atmospheric effects, it is known that water causes a strong absorption in the NIR, especially around 1400 nm, which can lead to a decreased intensity return if the targets are wet or if too much moisture is in the air (Franceschi et al., 2009). If the scans occur in a dry, arid environment with little to no humidity, and that the atmosphere is stable for the duration of the scan, then any possible atmospheric effects can be negated (Hartzell et al., 2014).

The results presented herein are based on the assumption that the acquired outcrop surfaces have Lambertian-like (diffusely reflecting) behaviour; that is that the intensity return will be reduced by the cosine of the angle of incidence (Pesci and Teza, 2008; Pfeifer et al., 2008; Jutzi and Gross, 2009). Due to the scans in this study being performed with the outcrop face nearly perpendicular to the scanning direction, the incidence angle is considered zero for the classified regions of the image. Due to these factors, the Optech parser correction for distance was considered adequate. Using this correction method, the intensity return can then be considered as a proxy for the reflectance of the target rocks.

2.3.5 Data Fusion and Processing

The intensity pre-processing and correction was followed by the generation of an 8-bit scaled intensity .xyz file containing data in the sequence *xyzi*, with *x, y,* and *z* being arbitrary coordinates, and *i* being the corrected intensity. A visualization of the workflow for the study is provided in Figure 2.7. The Canon EOS DSLR used in this study was calibrated on site at Optech, and a corresponding camera calibration file was provided.

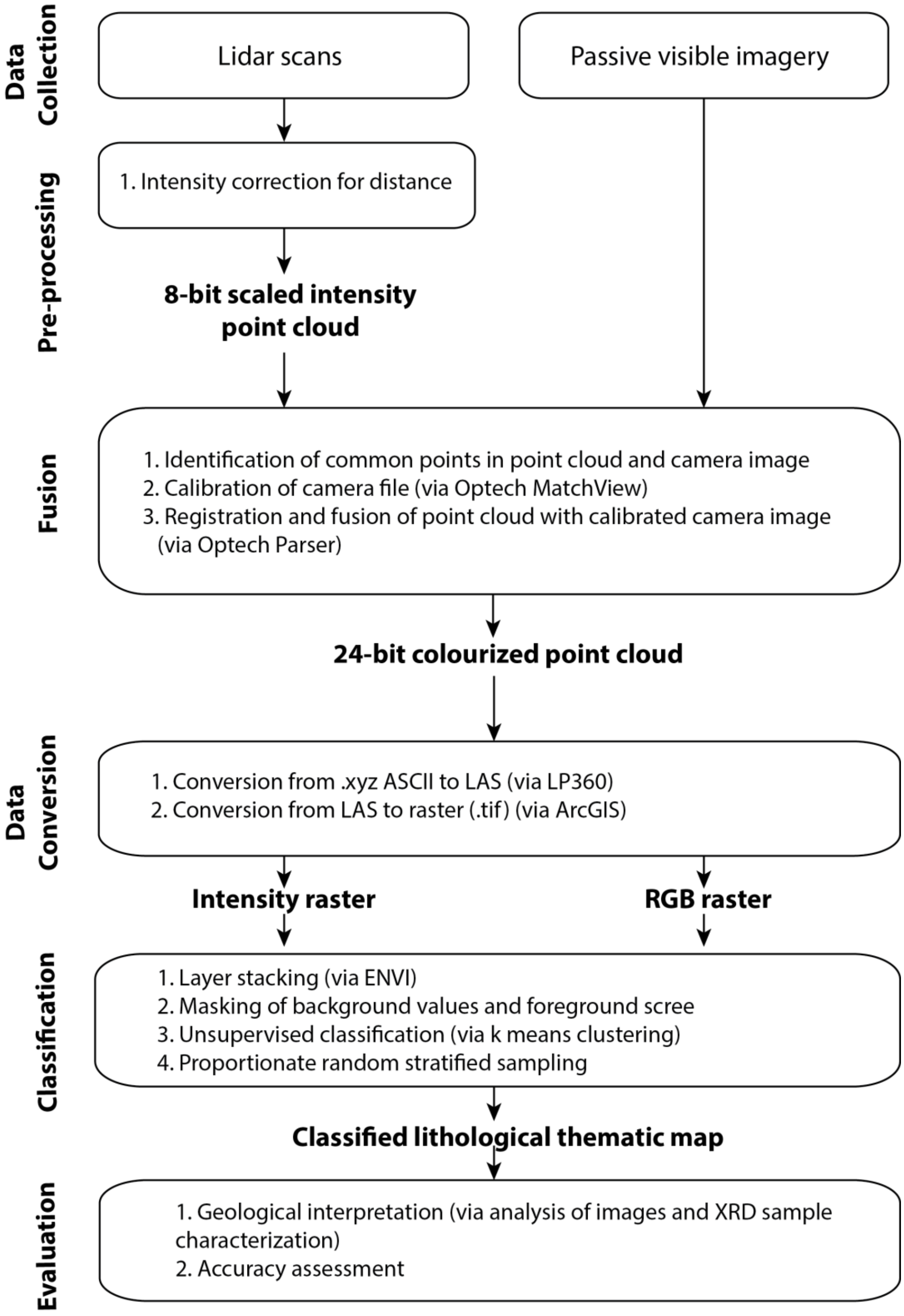

Figure 2.7. Workflow diagram showing the multiple steps required to produce the classified thematic map on an outcrop at Tunnunik. Data products are highlighted in bold.

In order to register the digital camera images that were taken of the same scene, a software program developed by Optech was utilized.

This program, MatchView, allows the user to register corresponding digital camera images with the lidar point cloud by identifying common points in both images. After identifying a minimum of five common points, and once the root mean square error (RMS) was below two pixels, the program calculated the new parameters for the camera calibration file that was provided. The final step to fuse these two datasets together was to use the Optech Parser again, and output a .xyz file with 24-bit texture. This was performed by providing the newly calibrated camera file along with the digital camera image to the parser, which output the colourized lidar point cloud. This .xyz file contains data in the sequence *x, y, z, i, R, G, B*. The *xyz* coordinates are arbitrary, with the origin at the centre of the laser scanner. Intensity and the RGB values are both in 8-bit format.

To initially visualize the fused data in 3D, an open-source software, CloudCompare, was utilized. In order to process this fused point cloud in image processing software, the cloud must first be properly projected and consequently converted to a raster format. To project the scan properly to allow for a face-on view of the canyon wall, the data was parsed into a .las file (*x, z, y, i, R, G, B*) using an ArcGIS extension called LP360 (note the data is now being stored with the *z* and *y* headers swapped in order to achieve a face-on view of the outcrop). To generate the raster products, the 'LAS dataset to Raster' tool was used in ArcGIS, creating two separate raster images; one containing the intensity data, and the other containing the RGB data. Both files have a pixel size of 0.4 cm, for a total of 3,797,208 pixels. Finally, the two raster images are imported into ENVI for the creation of the classified image.

2.3.6 Unsupervised Classification

Due to the presence of background data values outside of the 0-255 range, a mask was created prior to classification, confirming that the background values that are not a part of the scanned canyon wall were not incorporated into the final assessment. Another mask was incorporated to exclude the scree in the lower portion of the image. This is done due to the fact that geologists are mainly interested in the *in situ* material, and so the rubble near the bottom would rarely ever be sampled, since it does not provide the proper context to allow interpretation of the environment in which these rocks were formed. Also, the inclusion of scree would also affect the assumption that incidence angle is ~0 degrees. For these two reasons, the scree was chosen to be masked out. The two previously generated rasters were then stacked into a single 4-band layer, with intensity (NIR), Red, Green, and Blue bands being the variables incorporated for the classification. K-means clustering was performed in ENVI, with the initial output of 40 classes, which were then aggregated into four final classes (dolostone, dark grey shale, red shale, and green shale). The change threshold was set to 2%, with the maximum iterations set at 10. A second clustering was performed with only two classes—dolostone and combined shale—in order to assess the difference in accuracy when comparing multiple shale lithologies versus just one.

K-means is a cluster classifier that partitions a population ‘N’ into ‘*k*’ classes. The initial cluster centres will be arbitrarily set and represented by the means of the pixel vectors allocated to them (Richards, 2013). These initial clusters will run through a pre-programmed amount of iterations of re-clustering, until the change threshold within each class is below a specified percent. As noted by (Campos Inocencio et al., 2014), k-means clustering is an excellent classification technique for geological applications, as this method is not computationally demanding, and can process large amounts of data; identifying discrete patterns and relationships that may not be initially apparent. The output of this clustering method will be a classified thematic map that should differentiate between the lithologies present at the canyon wall outcrop.

2.3.7 Accuracy Assessment

In order to assess the validity of the classification scheme, proportionate stratified random sampling was used in order to compare pixels with the geological map created by the author via field observations of the outcrop and XRD analysis of the collected samples (Table 2.2). This method of sampling was preferred due to the fact that it ensures that even classes that cover a very small portion of the study area still will have samples allocated. For the classification of the four lithologies, the minimum sample size was set at 35 pixels (red shale), resulting in a total of 500 random pixels generated for accuracy assessment. When the three shale lithologies were combined, leading to two classes (dolostone and combined shale), there were a total of 492 random pixels generated for accuracy assessment. The minor pixel discrepancy between the two assessments is due to 8 pixels from the latter being located in unclassified areas. The distributions for each class can be seen in Table 2.2. The correct classification of each of these pixels was derived from observation and analysis while at the outcrop in July 2015, along with geological interpretation of the digital photographs taken. Assessment occurred by manually going through each of the generated random pixels and confirming if each pixel was classified as the correct lithology or not. If not correctly classified, it would be noted as to which class the pixel was incorrectly classified as. Ground truth was also corroborated by the XRD analysis of the samples collected from the outcrop. Upon completion, the data was compiled into an error matrix, which is presented below.

Table 2.2. Proportionate stratified random sampling distribution for: a) 4 classes; b) 2 classes.

a) Class	Number of Random Samples
Red Shale	35
Dark Grey Shale	185
Green Shale	39
Dolostone	241
Total	500

b) Class	Number of Random Samples
Shale	251
Dolostone	241
Total	492

2.4 Results

2.4.1 Sample Characterization

XRD analysis was performed to mineralogically characterize the samples collected along a transect of the scan region. Twelve samples were characterized and the semi-quantitative mineralogy based on relative peak heights and widths of the mineral species identified (Table 2.3). The XRD results are deemed as semi-quantitative due to the fact that no Rietveld cell refinement of the XRD profiles occurred. In Table 2.3, the dolomite, (combined) feldspar, quartz, and clay (muscovite) relative compositions are noted as relative increments of 25%, with <10% denoted by a square. It should be noted that the muscovite peaks could also be interpreted as glauconite, but due to the muscovite pattern fitting slightly better, it was chosen as the mineral present. After assessment of the XRD profiles, it was concluded that there were four unique lithologies present in the scanned area, which for simplicity of classification have been simplified to dolostone, dark grey shale (composed of varying amounts of dolomite, quartz, orthoclase, and muscovite), green shale (composed of varying amounts of dolomite, quartz, orthoclase, microcline, and muscovite), and red shale (composed of varying amounts of dolomite, quartz, orthoclase, microcline, muscovite, pyrite and ankerite).

Table 2.3. Semi-quantitative mineral compositions of rocks collected in this study based on X-Ray Diffraction (XRD) data. The dolomite, (combined) feldspar, quartz, and clay (muscovite) relative compositions are noted as relative increments of 25%, with <10% denoted by a square.

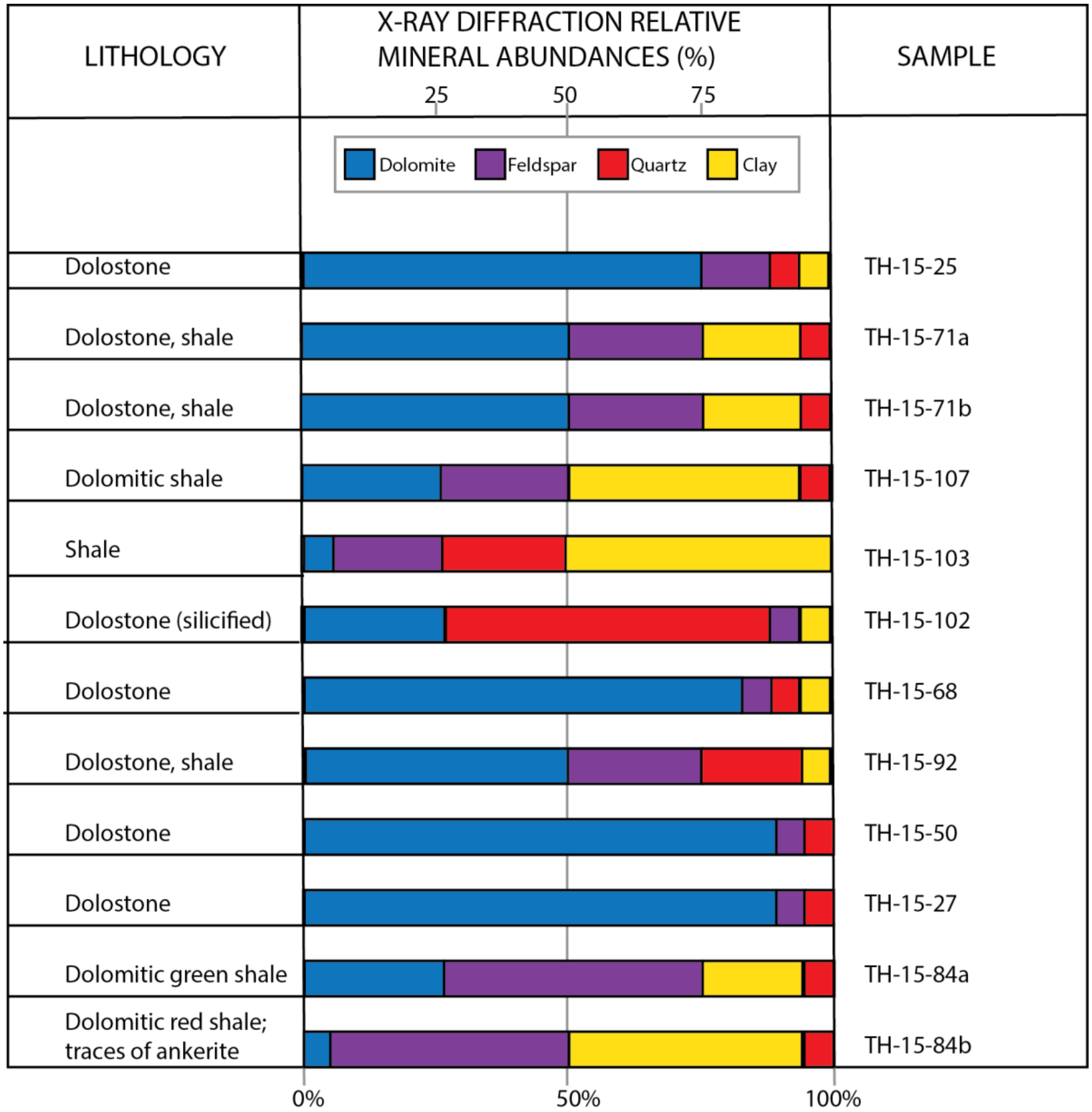

2.4.2 Relationship between Intensity and Lithology

Semi-quantitative analysis through XRD demonstrates that distance-corrected intensity is linked in a linear relationship with proxies for mineralogy at the near infrared wavelength of the lidar instrument. Figure 2.8a displays the distance-corrected intensity returns of the scanned outcrop from which the values were taken to compare against sample mineralogy.

The mean intensity (acquired via identifying the minimum and maximum intensity values) for each sample analyzed was compared against mineralogy (via XRD) to identify the relationship between them. The results of this comparison can be seen in the plots presented in Figure 2.9. The plots demonstrate the correlation between intensity and dolomite (Fig. 2.9a), as well as between intensity and proxies for shale (clay (Fig. 2.9b) and combined feldspar (Fig. 2.9c). Intensity displays a positive linear relationship with weight percent (wt. %) dolomite, with a R^2 value of 0.63. Intensity also displays a negative linear relationship with both wt. % clay and feldspar, providing R^2 values of 0.73 and 0.59, respectively. The corrected intensity values show a distinction between the values associated with dolostone, and for those associated with the shale lithologies (Fig. 2.8a). Dolostone is more reflective, leading to intensity highs; while the shale is less reflective, and is associated with the intensity lows. Figure 2.8 also presents the results of the RGB raster (Fig. 2.8b), which was utilized to produce manually defined geological maps (Figs. 2.8c and 2.8d) that depict the rock units used for evaluating the classification results.

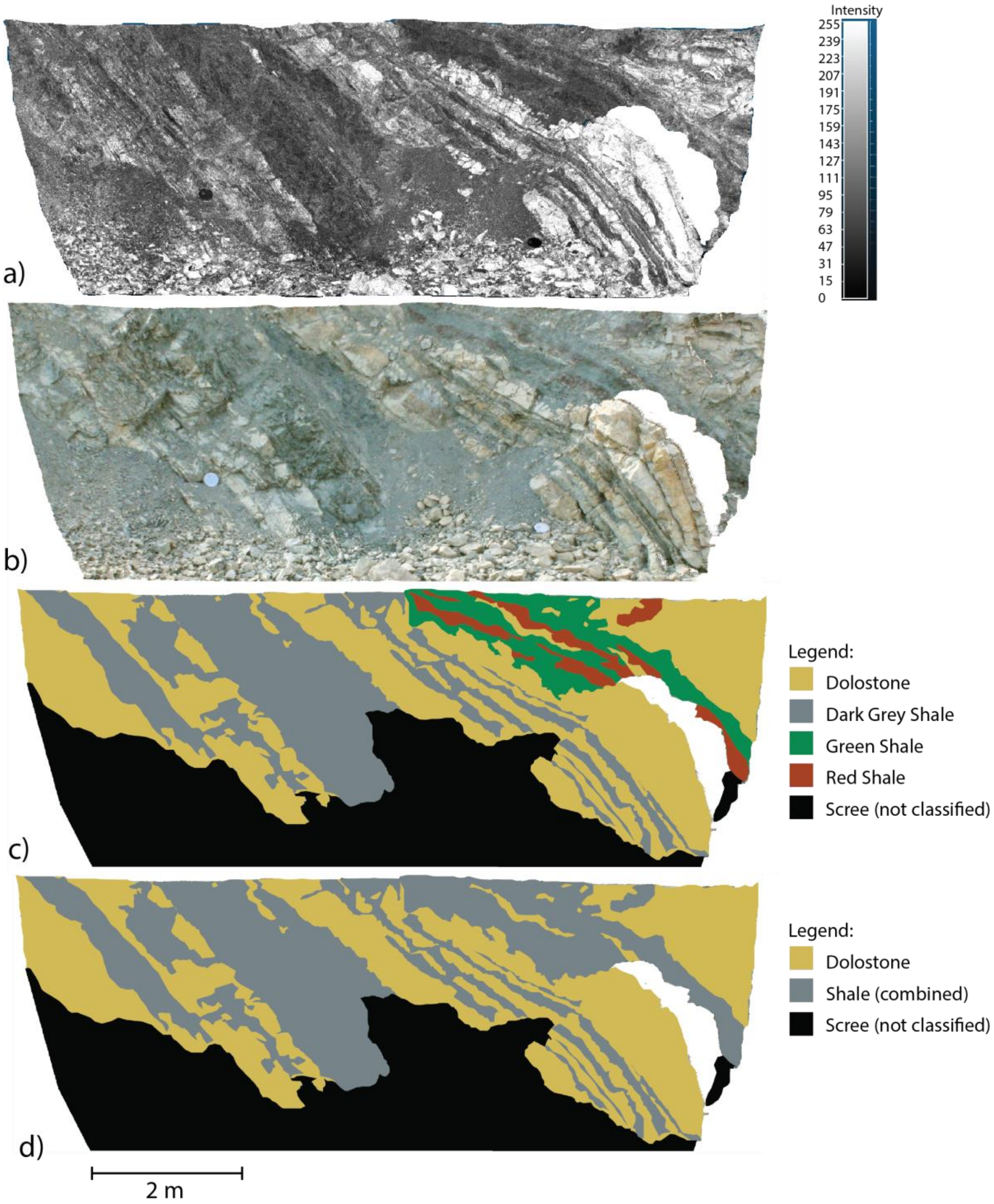

Figure 2.8. a) ILRIS corrected intensity band. b) Stacked visible passive red, green, and blue bands. Two pail lids are present as ground control points. c) Geological map of scan region when k = 4. d) Geological map of scan region when k = 2. Note the areas of scree at the bottom of the scan area are masked.

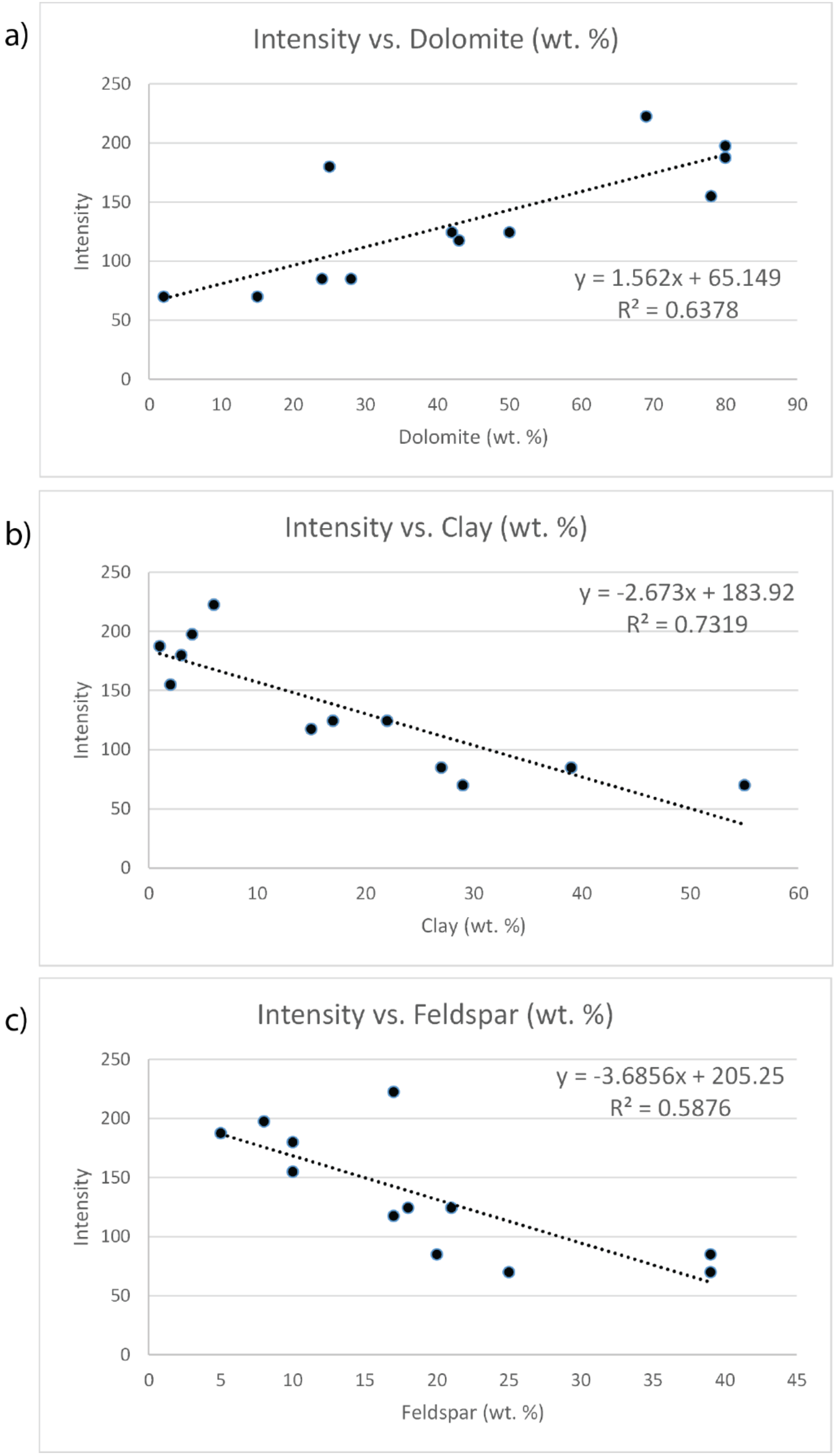

Figure 2.9. Distance-corrected intensity vs. mineralogy plots for: a) dolomite wt. %, b) clay wt. %, c) feldspar wt. %. These relationships indicate mineral composition is associated with corrected intensity.

2.4.3 Classification Results

Two separate clustering processes were performed on the fused dataset collected form the study area at the Tunnunik impact structure. The results of the unsupervised k-means clustering for four and two classes are shown in Figure 2.10. Both of these thematic lithologic maps were assessed for accuracy by performing proportionate stratified random sampling and comparing them to the manually defined geological maps (Figs. 2.8c and 2.8d) that were created by analyzing lithology via field observations and XRD analysis. Results for both classifications are presented below.

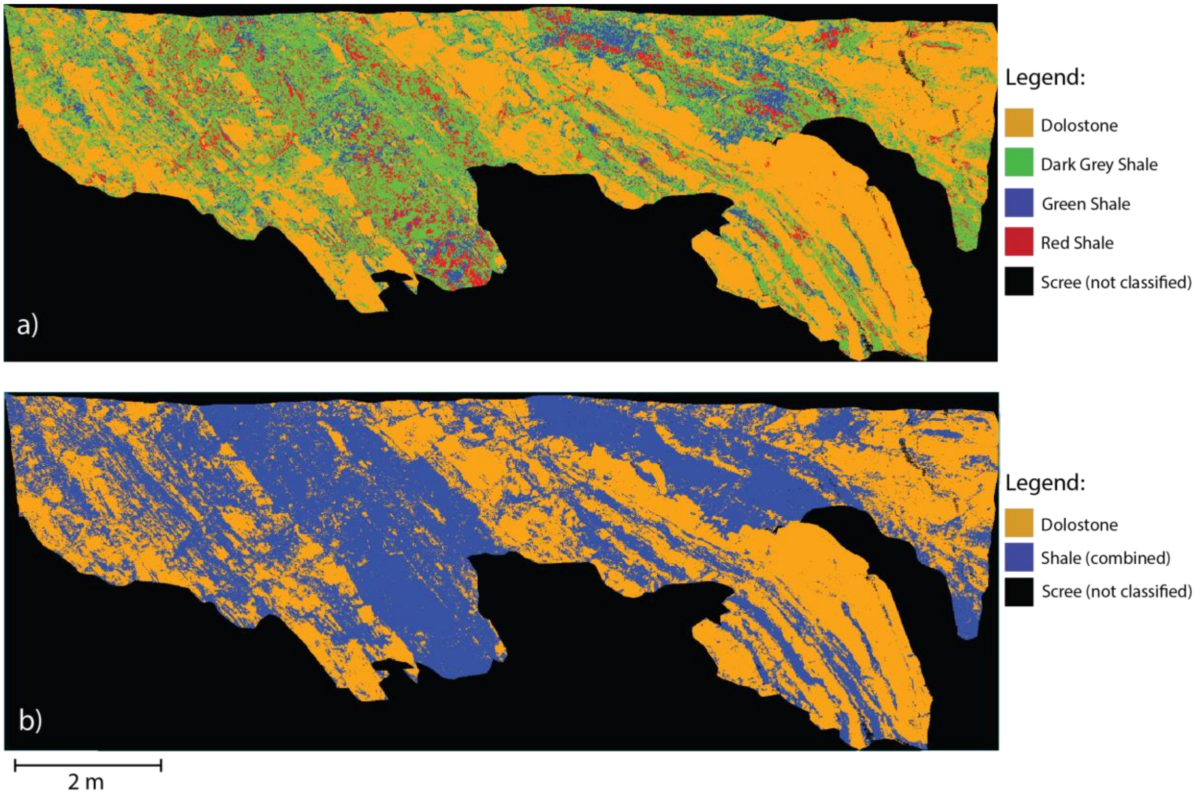

Figure 2.10. K-means clustering results of the fused dataset (distance-corrected intensity, passive red, passive green, and passive blue). a) Final classification with k = 4. b) Final classification with k = 2.

2.4.3.1 Four-Class Results

Initial classification attempts utilized four separate classes; one for each of the four lithologies present in the study area (dolostone, dark grey shale, green shale, and red shale). Class distributions were as follows: dolostone = 28.8% of image; dark grey shale = 22.9% of image; green shale = 4.8% of image; red shale = 4.3% of image; unclassified/masked area = 39.2% of image. To assess the accuracy of the classification, an error matrix was developed by comparing the pixels in the derived thematic map (Fig. 2.10a) to the geological map (Fig. 2.8c), which is presented in Table 2.4. The overall accuracy for the Tunnunik classification map with four classes is 69%. Producer’s (Table 2.5) and user’s (Table 2.6) accuracy were also assessed, which represent the probability of a reference pixel being correctly classified, and the probability that a pixel classified on the map actually represents that class on the ground, respectively. The dolostone class had the highest values for both producer’s (82.2%) and user’s (90.0%) accuracy, while the red shale class had the lowest values for producer’s (22.2%) and user’s (11.8%) accuracy. There was a high amount of misclassification between the three different types of shale, which led to a decrease in classification accuracy. The possible reasons for these misclassifications will be addressed in Section 2.5.2.

Table 2.4. Error matrix for the Tunnunik thematic map (k = 4). All values are in percent.

Class	*Validation: Red Shale*	*Validation: Dark Grey Shale*	*Validation: Green Shale*	*Validation: Dolostone*	*Total*
Red Shale	22.2	14.5	2.2	1.9	7.0
Dark Grey Shale	61.1	64.2	62.2	13.3	37.0
Green Shale	0.0	12.1	24.4	2.7	7.8
Dolostone	16.7	9.3	11.1	82.2	48.2
Total	100.0	100.0	100.0	100.0	100.0

Table 2.5. Producer's Accuracy for the Tunnunik thematic map (k = 4).

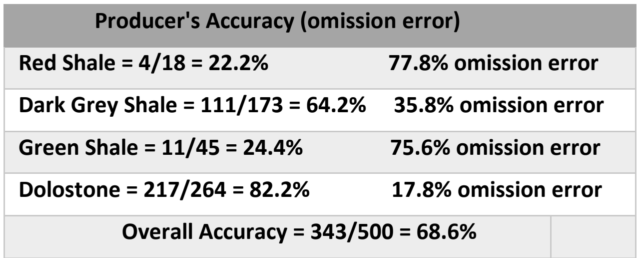

Producer's Accuracy (omission error)	
Red Shale = 4/18 = 22.2%	77.8% omission error
Dark Grey Shale = 111/173 = 64.2%	35.8% omission error
Green Shale = 11/45 = 24.4%	75.6% omission error
Dolostone = 217/264 = 82.2%	17.8% omission error
Overall Accuracy = 343/500 = 68.6%	

Table 2.6. User's Accuracy for the Tunnunik thematic map (k = 4).

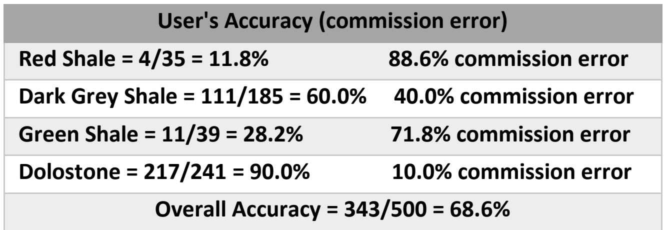

User's Accuracy (commission error)	
Red Shale = 4/35 = 11.8%	88.6% commission error
Dark Grey Shale = 111/185 = 60.0%	40.0% commission error
Green Shale = 11/39 = 28.2%	71.8% commission error
Dolostone = 217/241 = 90.0%	10.0% commission error
Overall Accuracy = 343/500 = 68.6%	

2.4.3.2 Two-Class Results

Following the initial classification with four classes, a second clustering process was performed, with only two classes being used for the final classification; dolostone and (combined) shale (Fig. 2.10b). This classification attempt was tested due to the fact that there is a high amount of misclassification within the three different shale lithologies. Class distributions were as follows: dolostone = 28.8% of image; shale = 32% of image; unclassified/masked area = 39.2% of image. As in the previous classification, an error matrix was created (Table 2.7), along with producer's (Table 2.8) and user's (Table 2.9) accuracy assessments, in order to evaluate whether the use of two classes improved or decreased the accuracy of the classification. After classification, the overall accuracy was shown to be 85.6%, which is a 17% increase from the classification with four classes. The dolostone and the shale class were both very similar in producer's and user's accuracy. Dolostone had accuracies of 82.2% (producer's) and 90.0% (user's), while the shale had accuracies of 89.5% (producer's) and 81.3% (user's). The accuracy of the shale classification improved dramatically by merging the three separate shale classes into one.

Table 2.7. Error matrix for the Tunnunik thematic map (k = 2). All values are in percent.

Class	*Validation: Dolostone*	*Validation: Shale*	*Total*
Dolostone	82.2	10.5	49.0
Shale	17.8	89.5	51.0
Total	100.0	100.0	100.0

Table 2.8. Producer's accuracy for the Tunnunik thematic map (k = 2).

Producer’s Accuracy (omission error)	
Dolostone = 217/264 = 82.2%	**17.8% commission error**
Shale = 204/228 = 89.5%	**10.5% commission error**
Overall Accuracy = 421/492 = 85.6%	

Table 2.9. User's accuracy for the Tunnunik thematic map (k = 2).

User’s Accuracy (commission error)	
Dolostone = 217/241 = 90.0%	**10.0% commission error**
Shale = 204/251 = 81.3%	**18.7% commission error**
Overall Accuracy = 421/492 = 85.6%	

2.5 Discussion

2.5.1 Relationship between Intensity and Lithology

As presented in Figure 2.9, distance-corrected intensity (at the 1535 nm wavelength of the lidar instrument) is shown to be positively linearly related to dolomite wt. %, and negatively linearly related to clay wt. %, and feldspar wt. %, for the scan performed at the Tunnunik impact structure. With respect to dolomite, the fact that it tends to weather to a white or tan colour may also play a role in the relationship between increasing wt. % dolomite and increasing intensity. The muscovite wt. % present in all the analyzed samples was used as a proxy for clay, which can be associated to the shales present in the study. The greater the clay content, the lower the intensity at 1535 nm. The association between the presence of a water absorption feature at ~1400 nm and the potential for bound water within the clay should be noted, as the decreased intensity values associated with increased shale content may rely at least partially on the amount of water present within the more porous shales. This negative linear relationship corroborates Burton et al. (2011), who, utilizing another ILRIS at 1535 nm, identified a relationship between log intensity and clay wt. %. The feldspars identified in this study were associated with the shales, with feldspar wt. % values being highest in the green and red shale in the upper right portion of the scan area. As with clay wt. %, the more feldspar present in a sample, the lower the corresponding intensity values were. It should be noted that this correlation may be due only to the fact that the feldspars are exclusively associated with the shale in this setting, and may not have the same relationship if present in other lithologies such as granite.

This study focused on terrestrial laser scanning with laser pulses coming into contact with the targeted canyon wall (assuming Lambertian behaviour) with little to no incidence angle, and thereby necessitating only a correction for distance. More corrections would be required in order to properly assess the relationship between intensity and lithology in different conditions, such as if the obliquity were increased, or if weather conditions were changed. For example, a recent study performing geological mapping of the Dents-du-Midi limestone massif in Switzerland via terrestrial lidar scanning needed to perform corrections for both distance and incidence angle (Matasci et al., 2015). The intensity correction to remove multiple variables was due to the fact that the dataset was comprised of six scans from multiple scan points with ranges of the target rocks varying between 450 m and 1200 m (Matasci et al., 2015). Related to the incidence angle of the scan, even more complex corrections will be required to compare the intensity to lithology when attempting to assess the relationship of 360° scans, due to the large number of varying incidence angles. Burton et al. (2011) also note that the presence of water and ice in a scan area has a strong impact on the returned intensity, leading to a noticeable decrease in intensity. This also means that scans collected from the same outcrop on different occasions can only be considered valid if the collection occurred under similar conditions and at the same laser wavelength; as the collection of one scan on a sunny day and another on a rainy day would lead to intensity values that would not be able to be reconciled.

It is important to note that for this study, absolute wt. % values cannot be directly compared to a certain intensity value, due to factors affecting the intensity response at the outcrop level. As noted by Franceschi et al. (2009), sedimentary rocks such as shale can retain absorbed water, which can lead to slightly lower intensity responses (especially with TLS operating at ~1500 nm), affecting the ability to directly compare absolute wt. % to specific intensities. While this may slightly affect certain responses, it is still apparent from the data shown in Figure 2.9 that the corrected lidar intensity at 1535 nm is related to lithology. By augmenting this information with other datasets, there is potential for high resolution spectral classification of planetary materials. As noted above, relative relationships can still be ascertained by performing semi-quantitative and quantitative analysis of collected samples (Table 2.3) and comparing with the corrected intensity (Fig. 2.8a).

Another challenge that arises when attempting to associate lidar intensity with lithology is the fact that the intensity value collected by the instrument is relative, and varies from sensor to sensor, especially when the instruments are from different manufacturers (Kashani et al., 2015). Carrea et al. (2016) also note that in order to achieve corrected intensities that can be utilized for lithological differentiation, it is important to use the same instrument for the entire survey, due to the fact that the wavelength and the transmitted power can vary instrument to instrument. As stated by Kashani et al. (2015), no standardized calibration or correction approach has yet been implemented, which creates challenges when attempting to compare intensity values across manufacturers, and especially when attempting to compare across platforms such as aerial and mobile laser systems. It is hoped that these challenges will be addressed in the near future, opening up new avenues for as of yet unknown applications.

2.5.2 Misclassification Factors

The initial four class clustering led to an overall accuracy of 68.6% (Table 2.5). As can be seen in Figure 2.10a, the vast majority of the misclassifications were between the three shale lithologies, and especially between the dark grey shale and the green shale. These two lithologies were only slightly different in visible imagery, and barely discernable in the NIR band. These factors led to the green shale being incorrectly classified as the dark grey shale in 62.2% of instances, with minor amounts of the dark grey shale being incorrectly classified as the green shale (12.1%). The red shale also was misclassified as the dark grey shale in 14.5% of instances. While still considered mostly consolidated, the three shale lithologies are quite friable, which may play a factor in the misclassification due to increased shadowing and possibly increased incidence angles. As noted previously, the lower portion of the scanned area was masked and not classified (Fig. 2.10) due to the fact that it is unconsolidated scree, which makes classification extremely difficult. Dark and shadowed areas were often misclassified as well. The most accurately classified lithology was the dolostone, which was also the most consolidated of the lithologies present.

While the overall accuracy of the four class clustering is still nearing ~70%, the goal of increasing the accuracy led to the refinement of the clustering to 2 classes; dolostone and combined shale (Fig. 2.10b). This final two class clustering led to an overall accuracy of 85.6% (Table 2.8). Dolostone was only incorrectly classified as shale in 10.5% of instances, and shale as dolostone in 17.8% of instances. There are two specific areas within the scan region (topmost right and topmost left) which these errors generally occur. Especially for the topmost left region, a potential reason for the incorrect classification of dolostone as shale is due to the dolostone not having as tan of a weathering surface as everywhere else in the scan region. This dolostone is greyer, and potentially may not have been exposed to the elements for as long as the rest of the outcrop due to physical weathering. Scattered fragments of shale that remain as scree on the dolostone in this area may also play a role in the misclassification. This shale most likely originated from areas of the outcrop above the scanned region where it later fell to its current position.

Another potential factor in misclassification may be due to the slight generalization of the geological maps (Figs. 2.8c and 2.8d). While many efforts were put in to creating the most accurate maps possible, very small areas of unconsolidated shale sitting on top of dolostone, or small pockets of dolostone within the shale, were not always possible to be incorporated into the final geological maps.

While several other studies have previously assessed the ability to identify different rocks in outcrops, to our knowledge, this is the first time k-means clustering has been utilized with a 4-band fused dataset in order to identify lithology. Campos Inocencio et al. (2014) have developed software that performs cluster analysis for classification of rocks in outcrops; however, this software is currently proprietary and also only incorporates the single band of NIR intensity for classification. The incorporation of three more bands in the visible spectrum in this study allow for increased spectral differentiation between areas of the scans that may be difficult to distinguish from intensity alone. For example, as shown in Figure 2.8a, the intensities of the red and green shale are quite similar, and while the classification was not able to differentiate between them perfectly, the incorporation of the RGB bands certainly improved it. Another benefit of incorporating a NIR band with the visible bands is that the visible bands can have shadowed regions depending on the location of the sun when the image was captured. Lidar intensity does not depend of ambient lighting, and therefore can fill areas of no data with NIR values.

Hartzell et al. (2014) performed a similar study that applied multispectral lidar to outcrops and up to six bands to be used in supervised classification. This required three different TLS and passive visible imagery collection. Supervised classification was able to be used due to the outcrop of interest being beside a road (Hartzell et al., 2014). As will be discussed in Section 2.5.3, it is suggested that unsupervised classification is more appropriate when studying outcrops in remote settings that cannot be assessed by a geologist beforehand and it can be argued there is no outcrop more remote than on another planetary body.

2.5.3 Utilization of Lidar for Future Planetary Missions

The incorporation of lidar for future robotic planetary exploration missions would be beneficial for both navigation and as a reconnaissance scientific tool in the proper conditions. Field-based research at planetary analogues have confirmed the fidelity of using lidar as navigational tool, concluding that its extremely precise geospatial data allows the rover to identify hazards with centimetre precision (Zylberman et al., 2016). When this hazard awareness and avoidance becomes fully autonomous, the ability for rovers to travel independently of input from scientists on Earth will lead to increased exploration distances, and through that, further discoveries about the history and evolution of our Solar System. Lidar can also be utilized as a reconnaissance scientific tool for robotic planetary missions, differentiating lithologies from distances of tens to hundreds of metres away. While not replacing primary scientific tools that can identify precise chemical and mineralogical characteristics of analyzed rocks, these tools generally require contact with the rock. If a high resolution lidar were able to be implemented onto future rovers, the data could be utilized to augment other datasets and potentially identify whether an outcrop tens to hundreds of metres away was of interest, and allow a decision on whether it is worth a visit to the outcrop for more detailed analysis.

While supervised classification methods may lead to slightly increased overall accuracy, it is not always the most feasible in the case of geological and planetary exploration. Supervised classification requires *a priori* knowledge of the area to be classified, and necessitates the creation of training sites of known classes (spectrally unique) before the classification algorithm is run. This *a priori* knowledge of an area may be possible when classifying urban areas, or areas covered by satellite imagery, but often is unfeasible in the case of remote outcrops, whether on Earth or another planetary body, such as the Moon. Unsupervised classification, including k-means clustering, removes this issue of establishing training sites prior to classification. A benefit of k-means clustering is the fact that it can process extremely large datasets relatively quickly, which is excellent for lidar point cloud files (Campos Inocencio et al., 2014). K-means clustering does require the input of *k* classes, but it is always wise to initially start with more classes than expected, and to later merge these classes. The method performed in this study still needs the input of a researcher to merge and confirm the accuracy of the classification, meaning that it is a semi-autonomous process. If this clustering method were to be implemented on future planetary missions, the initial unsupervised classification could act as a reconnaissance tool, and the fidelity of the classification could be assessed by a planetary scientist back on Earth. It is hoped that over time, this, and other unclassified classification algorithms can become powerful enough to lead to autonomous lithological classification, vastly expediting our exploration of other planetary bodies, and advancing the state of planetary science.

2.6 Concluding Remarks

This study has shown that mineralogy can be semi-quantitatively correlated with distance corrected intensity at 1535 nm, thereby proving the fidelity of utilizing lidar as a remote sensor of lithology, especially in planetary analogues. In conjunction with this, the fusion of NIR distance corrected intensity with passive visible imagery for remote lithological discrimination via k-means clustering was deemed successful, with overall accuracies of 68.6% (k = 4) and 85.6% (k = 2). A thematic map differentiating the lithologies was established for both clustering processes. Combining field and laboratory analysis of samples with the novel approach of performing k-means clustering on a fused dataset, including NIR lidar intensity returns and RGB passive visible images, has led to a successful discrimination of lithologies at the Tunnunik impact structure.

Ideally, a follow-up to this study would include the incorporation of other bands into the classification, to identify if this can increase the differentiation. Possible bands include surface roughness, or derivatives such as band ratios. Another potential follow up would be to mount a high resolution lidar on a rover and perform these scans and subsequent unsupervised classifications autonomously, with the researcher only receiving the thematic map, and assessing its validity through ground truthing via passive visible imagery returned from the rover.

Combined with basic *a priori* information on target composition or through augmentation with other datasets, the simultaneous acquisition of geospatial and scientific data from lidar instruments will greatly increase the application and value of using lidar, especially for mining, reconnaissance geological mapping in remote environments, and for future planetary missions.

2.7 References

BrukerAXS, 2005, DIFFRACplus Evaluation Package Release 2005. Bruker AXS, Karlsruhe, Germany.

Baldridge, A. M., S.J. Hook, C.I. Grove and G. Rivera, 2009, The ASTER Spectral Library Version 2.0. Remote Sensing of Environment, vol 113, pp. 711-715.

Burton, D., Dunlap, D.B., Wood, L.J., and Flaig, P.P., 2011, Lidar Intensity as a Remote Sensor of Rock Properties: Journal of Sedimentary Research, v. 81, no. 5, p. 339–347, doi: 10.2110/jsr.2011.31.

Campos Inocencio, L., Veronez, M.R., Wohnrath Tognoli, F.M., De Souza, M.K., Da Silva, R.M., Gonzaga, L., and Blum Silveira, C.L., 2014, Spectral pattern classification in lidar data for rock identification in outcrops: The Scientific World Journal, v. 2014, p. 1–10, doi: 10.1155/2014/539029.

Carrea, D., Abellan, A., Humair, F., Matasci, B., Derron, M.-H., and Jaboyedoff, M., 2016, Correction of terrestrial LiDAR intensity channel using Oren–Nayar reflectance model: An application to lithological differentiation: ISPRS Journal of Photogrammetry and Remote Sensing, v. 113, p. 17–29, doi: 10.1016/j.isprsjprs.2015.12.004.

Dewing, K., Pratt, B.R., Hadlari, T., Brent, T., Bédard, J., and Rainbird, R.H., 2013, Newly identified “Tunnunik” impact structure, Prince Albert Peninsula, northwestern Victoria Island, Arctic Canada: Meteoritics & Planetary Science, v. 48, no. 2, p. 211–223, doi: 10.1111/maps.12052.

Franceschi, M., Teza, G., Preto, N., Pesci, A., Galgaro, A., and Girardi, S., 2009, Discrimination between marls and limestones using intensity data from terrestrial laser scanner: ISPRS Journal of Photogrammetry and Remote Sensing, v. 64, no. 6, p. 522–528, doi: 10.1016/j.isprsjprs.2009.03.003.

Girardeau-Montaut, D. 2016, Cloudcompare, a 3D Point Cloud and Mesh Processing Free Software. <www.cloudcompare.org> (accessed on 06.05.2016).

Google Earth 7.1, 2016, Arctic Canada. Image data: Landsat. Map data: ©2016 Google. Available from: <www.google.com/earth> (accessed on 07.04.2016).

Hartzell, P., Glennie, C., Biber, K., and Khan, S., 2014, Application of multispectral LiDAR to automated virtual outcrop geology: ISPRS Journal of Photogrammetry and Remote Sensing, v. 88, p. 147–155, doi: 10.1016/j.isprsjprs.2013.12.004.

Höfle, B., and Pfeifer, N., 2007, Correction of laser scanning intensity data: Data and model-driven approaches: ISPRS Journal of Photogrammetry and Remote Sensing, v. 62, no. 6, p. 415–433, doi: 10.1016/j.isprsjprs.2007.05.008.

Jelalian, A.V., 1992, Laser Radar Systems. Artech House, Boston London.

Jensen, J.R. 2007, Remote sensing of the environment: An earth resource perspective (2nd edition). Prentice Hall, Upper Saddle River, NJ.

Jutzi, B., and Gross, H., 2009, Normalization of Lidar Intensity Data Based on Range and Surface Incidence Angle: The International Archives of the Photogrammetry, Remote Sensing and Spatial Information Sciences 38 (Part 3/W8), v. XXXVIII, no. 2006, p. 213–218.

Kaasalainen, S., Jaakkola, A., Kaasalainen, M., Krooks, A., and Kukko, A., 2011, Analysis of incidence angle and distance effects on terrestrial laser scanner intensity: Search for correction methods: Remote Sensing, v. 3, p. 2207–2221, doi: 10.3390/rs3102207.

Kashani, A.G., Olsen, M.J., Parrish, C.E., and Wilson, N., 2015, A review of LIDAR radiometric processing: From ad hoc intensity correction to rigorous radiometric calibration: Sensors (Switzerland), v. 15, no. 11, p. 28099–28128, doi: 10.3390/s151128099.

Krooks, a., Kaasalainen, S., Hakala, T., and Nevalainen, O., 2013, Correction of Intensity Incidence Angle Effect in Terrestrial Laser Scanning: Annals of Photogrammetry, Remote Sensing and Spatial Information Sciences, v. II-5/W2, no. June 2015, p. 145–150, doi: 10.5194/isprsannals-II-5-W2-145-2013.

Matasci, B., Carrea, D., Abellan, A., Derron, M.H., Humair, F., Jaboyedoff, M., and Metzger, R., 2015, Geological mapping and fold modeling using terrestrial laser scanning point clouds: Application to the Dents-du-Midi limestone massif (Switzerland): European Journal of Remote Sensing, v. 48, p. 569–591, doi: 10.5721/EuJRS20154832.

Newman, J. D., and Osinski, G. R., 2016, Geological Mapping of the Tunnunik Impact Structure, Victoria Island, Canadian High Arctic, in 47th Lunar and Planetary Science Conference, Houston, Texas.

Optech, 2016, ILRIS Terrestrial Laser Scanner: Summary Specification Sheet. <http://www.teledyneoptech.com/wp-content/uploads/ILRIS-Spec-Sheet-140730-WEB.pdf> (accessed on 07.07.16).

Osinski, G.R., Abou-Aly, S., Francis, R., Hansen, J., Marion, C.L., Pickersgill, A.E., and Tornabene, L.L., 2013, The Prince Albert Structure, Northwest Territories, Canada: A New 28-km Diameter Complex Impact Structure, in 44th Lunar and Planetary Science Conference, Houston, Texas.

Osinski, G.R., Barfoot, T.D., Ghafoor, N., Izawa, M., Banerjee, N., Jasiobedzki, P., Tripp, J., Richards, R., Auclair, S., Sapers, H., Thomson, L., and Flemming, R., 2010, Lidar and the mobile Scene Modeler (mSM) as scientific tools for planetary exploration: Planetary and Space Science, v. 58, no. 4, p. 691–700, doi: 10.1016/j.pss.2009.08.004.

Penasa, L., Franceschi, M., Preto, N., Teza, G., and Polito, V., 2014, Integration of intensity textures and local geometry descriptors from Terrestrial Laser Scanning to map chert in outcrops: ISPRS Journal of Photogrammetry and Remote Sensing, v. 93, p. 88–97, doi: 10.1016/j.isprsjprs.2014.04.003.

Pesci, A., and Teza, G., 2008, Effects of surface irregularities on intensity data from laser scanning: An experimental approach: Annals of Geophysics, v. 51, no. 5-6, p. 839–848, doi: 10.4401/ag-4462.

Pesci, A., Teza, G., and Ventura, G., 2008, Remote sensing of volcanic terrains by terrestrial laser scanner: preliminary reflectance and RGB implications for studying Vesuvius crater (Italy): Annals of Geophysics, v. 51, no. 4, p. 633–653, doi: 10.4401/ag-4455.

Pfeifer, N., Höfle, B., Briese, C., Rutzinger, M., and Haring, A., 2008, Analysis of the backscattered energy in terrestrial laser scanning data: Int. Arch. Photogramm. Remote Sens. Spat. Inf. Sci., v. 37, p. 1045–1052.

Pfeifer, N. & Briese, C., 2007, Geometrical aspects of airborne laser scanning and terrestrial laser scanning: International Archives of Photogrammetry, Remote Sensing and Spatial Information Sciences, v. XXXVI, p. 311–319.

Richards, J. A., 2013, Remote Sensing Digital Image Analysis: An Introduction (5th ed). Springer.

Wagner, W., Ullrich, A., Ducic, V., Melzer, T., and Studnicka, N., 2006, Gaussian decomposition and calibration of a novel small-footprint full-waveform digitising airborne laser scanner: ISPRS Journal of Photogrammetry and Remote Sensing, v. 60, no. 2, p. 100–112, doi: 10.1016/j.isprsjprs.2005.12.001.

Zylberman, W., Hickson, D., Haid, T., and Osinski, G.R., 2016, 2015 CanMars MSR Analogue Mission: The Key Role of LiDAR in Rover Navigation and Potential for Future Missions, in 47th Lunar and Planetary Science Conference, Houston, Texas.

Chapter 3

3 Utilization of terrestrial lidar intensity data and passive visible imagery for remote ore detection: A case study of the Nickel Rim South Mine, Sudbury, Ontario, Canada

3.1 Introduction

Historically, ore identification and grade estimation were completed by geologists in underground mines. Geologists would approach the newly blasted face and make estimations on the amount of ore present in the face and assess if the ore is following specific structures in the rock, among others. These estimations were generally completed with a notepad or tablet, along with capturing photographs of the faces. Due to the inherent safety risks of working underground, there has been increasing interest in the automation of both mapping and ore discrimination in underground mining. The emergence of terrestrial laser scanners (TLS) has led to the ability to simultaneously complete both these tasks, with the added value of its ability to collect data without the need for ambient lighting (Höfle and Pfeifer, 2007), which is extremely beneficial in the dark and poorly lit environment of an underground mine. Terrestrial lidar has been an underutilized tool in mining exploration; although recent studies have begun to use terrestrial lidar (Huber and Vandapel, 2006; Lemy et al., 2006; Fekete et al., 2010) as well as mobile lidar (Zlot and Bosse, 2014) for high resolution georeferenced 3D models of underground mines utilizing x, y, and z data from the scans.

The majority of terrestrial lidar scanners available today utilize the time-of-flight principle and angle of emission to measure ranges via laser pulses—between 500 nm and 1550 nm—to objects with very high accuracy (Jensen, 2007; Pfeifer and Briese, 2007). The instrument collects hundreds of thousands of points per second, with each point containing specific x, y, and z coordinates that are attributed to a precise point on the target being scanned. Lidar instruments also record the intensity of the returned laser pulse. Intensity is a measure of the backscattered energy—at the wavelength of the laser—that is reflected off the target relative to the energy of the initial pulse (Jelalian, 1992). This intensity return is generally processed by manufacturer’s software and scaled to an 8, 12, or 16-bit dynamic range, which can be included as a scalar field in the point cloud (Höfle and Pfeifer, 2007; Kashani et al., 2015). The aim of many studies utilizing lidar for outcrop analysis is to identify and discriminate between the lithologies present, which requires knowledge of the absolute reflectance of the target rocks. This requires the need for a correction to the intensity values prior to analysis in order to remove extraneous factors such as range, incidence angle, surface roughness and atmospheric effects. Multiple correction methods for intensity have been proposed (Pesci et al., 2008; Franceschi et al., 2009; Kaasalainen et al., 2011; Penasa et al., 2014; Carrea et al., 2016), but a standardized method for all terrestrial lidar scanners still does not exist. At this stage, each researcher will have to choose a correction method based on the influence of the factors mentioned above for their specific situation. Corrected intensity can then be compared to the target composition, as different rock types will return a different intensity response, thus acting as a remote sensor of lithology. Several previous studies have been undertaken using corrected lidar intensity, resulting in the differentiation of sandstones and shale (Burton et al., 2011), limestones from marls (Franceschi et al., 2009), sandstones, carbonaceous pelites, and diamictites (Campos Inocencio et al., 2014) and shales, marlstones, and limestones in a limestone massif (Matasci et al., 2015). Fusion of near infrared (NIR) lidar intensity with passive visible imagery has led to advances for multispectral analysis and classification of rocks (Hartzell et al., 2014). Using supervised classification techniques, Hartzell et al. (2014) were able to confidently differentiate and classify sandstone and limestone in an outcrop. Due to these advances, lidar has become a powerful tool for image classification, especially in geological environments such as underground mines.

While multiple studies highlight high resolution analysis of geological outcrops for differentiation of materials on the surface (Pesci et al., 2008; Franceschi et al., 2009; Osinski et al., 2010; Burton et al., 2011; Campos Inocencio et al., 2014; Hartzell et al., 2014; Matasci et al., 2015), little to no research has occurred in an underground setting, which has its own unique set of variables, including poorly lit areas, considerable dust, and wetness. Several previous studies have investigated ore grade in underground environments using TIR spectroscopy (Rivard et al., 2001) and visible/IR hyperspectral reflectance spectra (Gallie et al., 2002), but to our knowledge, no work has been completed on utilizing the intensity response from lidar scans to investigate if remote differentiation between ore and host rock in an underground environment is possible, while also retaining a precise 3D documentation of the scanned mine faces. Generally opaque minerals will darken a sample, leading to a reduction in overall reflectivity with decreased grain size (Hunt et al., 1971), but Gallie et al. (2002) found that the presence of massive sulphide will act to dramatically increase the reflectance. While most likely unable to discriminate between disseminated ore, it is hypothesized that massive sulphide ore—especially chalcopyrite and pentlandite—will be able to be discriminated from the barren host rock due to their increased reflectivity and therefore elevated lidar intensity returns.

This study consists of a proof of concept experiment comprised of laboratory-based scans of common ore minerals and host rocks present in the Sudbury mining district, followed by a field investigation at the Nickel Rim South (NRS) mine, where lidar scans were completed on ore-bearing stope faces in both dry and wet conditions. Following the methodology developed and presented in Chapter 2, unsupervised classification via k-means clustering was performed on a 4-band dataset—which included high resolution NIR intensity data and passive visible imagery—for the discrimination of ore from the surrounding host rock and concrete spray.

The goal of this study is to determine the fidelity of discriminating between ore and host rock in an underground environment through the fusion of corrected lidar intensity and passive visible imagery. Application of the k-means clustering (unsupervised classification) technique is demonstrated on a dataset collected from an ore-bearing stope face, establishing a thematic map of the scan area that classifies the ore, host rock, and surrounding concrete spray and protective fencing and bolts. Accuracy of the classification is assessed and the advantages and limitations of the method in an underground setting are discussed. Finally, because lidar has potential to increase efficiency and safety in the underground environment, the fidelity of using such data for detailed ore body modelling over time is discussed.

3.2 Proof of Concept Study

To test the hypothesis that ore can be differentiated from surrounding host rock utilizing lidar intensity returns, a proof of concept study was performed. This study was comprised of performing lidar scans on common sulphide ore minerals alongside several barren rock types. These samples are representative of the common copper and nickel ore minerals, which dominate the Sudbury mining district (Ames et al., 2008; Pentek et al., 2008), and also include common host rocks for mineralization. A zinc ore sample was also included. These samples can be seen in Figure 3.1a, and are comprised of pentlandite ($(Fe,Ni)_9S_8$), norite (composed of labradorite $(Ca,Na)(Si,Al)_4O_8$), orthopyroxene ($(Mg,Fe)SiO_3$), and olivine ($(Mg,Fe)_2SiO_4$), chalcopyrite ($CuFeS_2$), quartz diorite (composed of plagioclase ($(Na,Ca)AlSi_3O_8$) and quartz (SiO_2), with minor orthoclase ($KAlSi_3O_8$), hornblende ($(K,Na)_{0\text{-}1}(Ca,Na,Fe,Mg)_2(Mg,Fe,Al)_5(Al,Si)_8O_{22}(OH)_2$)), and pyroxene ($(Ca,Mg,Fe)_2Si_2O_6$)), quartz monzonite (composed of equal amounts of plagioclase and orthoclase, quartz, and minor hornblende) and sphalerite (ZnS).

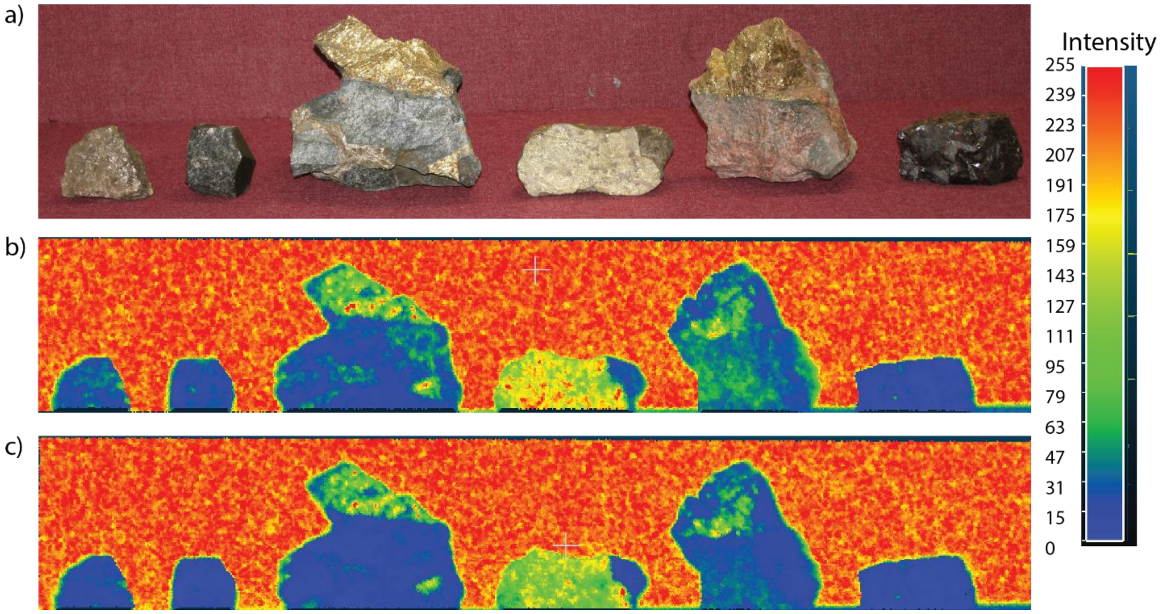

Figure 3.1. Proof of concept lidar scans comparing intensity responses from common ore minerals and host rocks present in the Sudbury mining district. a) Sample rocks used in the scans. From left: massive pentlandite, norite, massive chalcopyrite and pentlandite stringers within quartz diorite, massive chalcopyrite with blebs of pentlandite and pyrite, massive chalcopyrite within feldspar-rich quartz monzonite, massive sphalerite. b) Intensity returns of the 20 m scan with dry rock samples. c) Intensity returns of the 20 m scan with wet rock samples. Note the decrease in intensity when the samples are wet.

As mining environments can vary in moisture, both dry and wet scans were performed, to assess the effect of wetting. Scans of these rocks occurred with the commercially available Optech ILRIS terrestrial laser scanner, which utilizes a 1535 nm wavelength laser (detailed specifications in Table 1). At this wavelength, the intensity response should be sensitive to water content due to a water absorption feature at ~1400 nm, and so we should see a decrease in intensity for the scans of the wet samples (Franceschi et al., 2009). Scans of wet and dry samples occurred under low-light conditions (to mimic an underground setting) at a distance of 20 m. Each scan took approximately 15 minutes, with approximately 1 mm spot spacing. Scans were parsed using the Optech Parser, scaling the intensity responses to 0-255. The results were visualized using open source software, notably CloudCompare (Girardeau-Montaut, 2016). The results of the dry and wet scans can be seen in Figure 3.1b and 3.1c, respectively. Even from a solely visual assessment, it is apparent that the massive chalcopyrite is easily differentiable from the host rock, especially so in dry conditions. Even when the samples are wet, it appears that the intensity decreases relatively equally for all of the samples, meaning the ore is still discernable from the host rocks. Massive chalcopyrite appears to be the most easily differentiable from the surrounding rock, followed by pentlandite, which exhibited a lower response than chalcopyrite, but still generally higher than barren host rock. These results showed the feasibility of lidar intensity returns to be used to remotely distinguish ore from host rock, especially in the case of massive and stringer ore composed of chalcopyrite and pentlandite. Further work was performed at Nickel Rim South mine to test the efficacy of this differentiation in an underground setting.

3.3 Study Area

Lidar scans were acquired underground at the Nickel Rim South (NRS) mine in February 2016. As indicated in Figure 3.2, the Nickel Rim South mine is located in the East Range of the Sudbury Basin, 3 km north of the airport located in Sudbury, Ontario, Canada. The Sudbury Basin is a ~60 x 25 km elliptically shaped structure formed by a meteorite impact approximately 1850 Ma, which was later deformed to its current shape (McLean et al., 2005). The structure was originally proposed to be of impact origin in 1964 (Dietz, 1964), but it was only confirmed after decades of debate. Grieve et al. (1991) proposed the Sudbury impact structure seen today was the erosional and deformed remnant of an approximately 200 km multi-ring impact basin, which continues to hold consensus today. The Sudbury Structure straddles the boundary between three geological provinces, with the Neoarchean Superior Province to the north, and the Mesoproterozoic Southern Province and late Mesoproterozoic Grenville Province to the south (McLean, 2005).

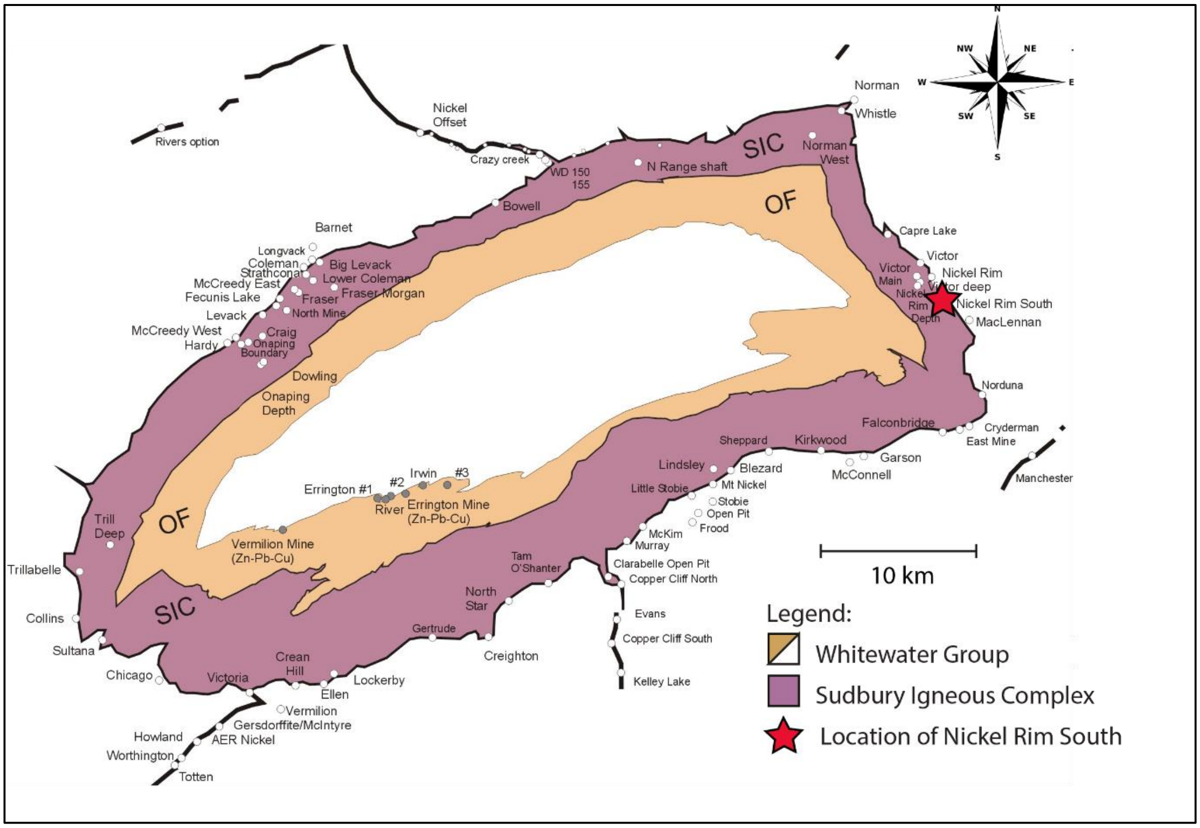

Figure 3.2. Simplified regional geologic map of the Sudbury impact structure, Ontario, Canada. Location of the Nickel Rim South mine is indicated by the red star. Small circles indicate other known Ni-Cu-PGE and Zn-Pb-Cu deposits and occurrences within the Sudbury mining camp. OF = Onaping Formation, SIC = Sudbury Igneous Complex. (after Ames et al., 2003).

The Sudbury Structure can be broken down into three main components: 1) the central Sudbury Basin, composed of post-impact sediments and breccias of the Onaping Formation; 2) the Sudbury Igneous Complex (SIC), a differentiated melt sheet composed of an upper granophyre unit, underlying norite, quartz gabbro, and the basal gabbroic to noritic sublayer; and 3) the footwall rocks, which is generally locally brecciated, with the Sudbury Breccia located at the contact of the SIC and the footwall rocks (McLean et al., 2005).

While not the only type of deposit present in the Sudbury mining camp, footwall-type Cu-Ni-PGE mineralization is a dominant mineralization style that was present at the level where the lidar scans occurred at the Nickel Rim South mine. This chalcopyrite dominated mineralization generally occurs in intensely brecciated areas of the Sudbury Breccia, and is characterized by massive sulphide veins along with smaller stringers and associated disseminated sulfides (McLean et al., 2005; Pentek et al., 2008). As noted by McLean et al. (2005), the ore mineral assemblage is composed of dominantly chalcopyrite ($CuFeS_2$), with lesser amounts of pentlandite ($(Ni,Fe)_9S_8$), pyrrhotite ($Fe_{1-x}S$), and bornite (Cu_5FeS_4). Scans of ore and the Sudbury Breccia host rock occurred at the 1565 m level within the mine.

3.4 Methods

3.4.1 Instrumentation

The Optech ILRIS (Intelligent Laser Ranging and Imaging System) 3D laser scanner was the TLS utilized to acquire the scans in this study. The ILRIS operates in the near infrared, at a wavelength of 1535 nm, which is eyesafe (Table 3.1).

The sensor is field portable and weighs approximately 15 kg, which can be mounted on a tripod for data acquisition. The ILRIS can be powered by a portable battery pack, but due to the potential of them becoming drained before underground scanning was complete, a portable MotoMaster PowerBox was utilized to provide power to the scanner for up to 5 hours. The scanner is controlled by Optech software, which sends the user-provided parameters from the field laptop using an Ethernet cable. The ILRIS has a 40º x 40º field of view, and an inboard camera which captures an initial image of the scan area. A region of interest (ROI) can be generated from a subsection of the field of view, which dictates where data will be collected via scanning. Once the ROI has been set, parameters can be adjusted, such as spot spacing and angular resolution, which will increase or decrease scan time, based on how high or low the required resolution needs to be for a particular study. Scan acquisition follows, with the raw data being stored as a dat/i3d file. A DSLR camera was also mounted on the top of the scanner, allowing for corresponding images of the scan area to be captured, which can later be registered to the lidar scan point cloud. The camera used in this study was a Canon EOS Rebel XTi with an 18-55 mm lens, and 10.1 megapixel resolution.

Table 3.2. Main technical specifications of the Optech ILRIS 3D terrestrial laser scanner (Optech, 2016).

Parameter	Unit	
Wavelength	nm	1535
Laser Class		1 (eyesafe)
Range (80% target reflectivity)	m	1250
Range (10% target reflectivity)	m	400
Minimum acquisition distance	m	3
Laser beam divergence	mrad	0.15
Laser beam divergence at 50 m	mm	21
Acquisition accuracy at 50 m	mm	7
Minimum spot spacing at 50 m	mm	1.3

3.4.2 NRS Data Collection

The lidar scans for this study were acquired on the 1565 m level of the Nickel Rim South mine on February 8th, 2016. The ILRIS and associated hardware—including power source and tripod—were brought underground via the main shaft elevator, and then the author was driven to a recently blasted stope containing dominantly massive copper ore within the Sudbury breccia host rock. A scanning location was chosen along the stope wall that contained large chalcopyrite stringers. Concrete spray and fencing had also been installed along this face, which was also incorporated in the scan in order to identify if the presence of these would affect the final classification of the point cloud. Two scans were performed; one with the face dry and dust covered, and the second after washing the wall down with water, resulting in a wet, but non-dust covered face. Both scans were performed from the same location, at a distance of 5 m from the target, and with a point spacing of 2 mm. Scanning time was 15 minutes each, with the instrument positioned so that the targeted wall was perpendicular to it, in order to reduce the effects of incidence angle. The data acquired from both scans was initially stored in an Optech proprietary format (dat/i3d), which was later parsed into an ASCII format. The scanned area used for analysis was 1 x 1 m, and had a total of 2,381,934 points collected for each of the two scans. A digital camera was mounted on top of the ILRIS, and corresponding passive visible images were captured with the assistance of an external light source and flash behind the instrument as to not have areas of shadow in the image, which could affect the following classification.

3.4.3 Intensity Pre-Processing

Using Optech's parsing software, the raw scan files are converted into formats that can then be visualized and assessed by open source programs. The point cloud visualization and analysis software used in this study was CloudCompare (Girardeau-Monteaut, 2016). The intensities were exported in a XYZ 8-bit ASCII format. The parser does this by converting the raw data into a point cloud with the set $\{(x_k, y_k, z_k, I_n (x_k, y_k, z_k))\ k = 1, 2 \ldots N\}$ where $I_n (x_k, y_k, z_k)$ is an 8-bit digital number, representing the distance-corrected intensity normalized to the range 0-255, and N is the number of points where the intensity is useful. Raw intensity has been shown to be a function of the inverse range square ($1/R^2$) (Wagner et al., 2006; Höfle and Pfeifer, 2007; Pesci et al., 2008; Krooks et al., 2013). This correction allows for the intensities to be the same for materials of the same composition at different distances. The Optech parser converts the raw intensity to the distance-corrected intensity in three steps. First, the shot intensity is pre adjusted according to its range via $I_p = I_r{}^*(d_k / d_r)^2$ where I_p is the preadjusted intensity, I_r is the raw intensity in the dat/i3d file, d_k is the shot range, and d_r is a reference distance that can be adjusted in the parser settings. Second, outliers are trimmed from the preadjusted intensities by finding the upper limit (UL), below which there are 95% of all shots. Finally, the preadjusted intensities are scaled to 0-255 via $I_n = 255^*(I_p / UL)$ where I_n is the distance-corrected normalized intensity.

Depending upon the environment under which the scans are being performed, multiple other factors can influence the intensity return from lidar scans, and include incidence angle, surface roughness of the target, and the atmosphere. The angle between the laser beam and the target surface normal can have a large influence on the intensity returns, and under Lambertian conditions, intensity is accepted to be equal to the cosine of the angle of incidence (Pesci and Teza, 2008; Pfeifer et al., 2008; Jutzi and Gross, 2009). Hartzell et al. (2014) concluded that incidence angle only produces a significant effect that requires correction when the angle exceeds 20º. Other researchers have concluded that natural extended surfaces such as rocks in an outcrop are generally characterized by roughness on the scale of the laser beam diameter, meaning a significant amount of the illuminated target will always be oriented towards the sensor, negating the effect of incidence angle (Pesci et al., 2008; Franceschi et al., 2009; Hartzell et al., 2014; Penasa et al., 2014). In one study, the incorporation of a correction for incidence angle on a scan of an outcrop actually lead to a decrease in classification accuracy, thereby leading the researchers to conclude that intensity returns are independent of incidence angle for surfaces that have roughness values of those generally found in outcrops (Hartzell et al., 2014). It should be noted that the metallic surface of the ore may not directly follow Lambertian behaviour, but in this situation the difference in reflectivity between the ore and host rock is deemed to be large enough that no further corrections are necessary for discrimination. The conditions of the atmosphere during scanning also can have an effect on the intensity returns. Water is known to have a strong absorption band in the near infrared at ~1400 nm, which can lead to a decreased intensity response on targets that are wet (Franceschi et al., 2009). For an environment such as an underground mine—which can often be wet—these effects must be taken into account when attempting to interpret the intensity returns. As seen in the proof of concept scans, if the entire scanning area is evenly wet, while having decreased values, the intensity returns are decreased equally for each rock type, still allowing for differentiation between the ore and host rock.

The results presented in this study are based on the assumption that the scanned stope face has Lambertian behaviour, with the intensity related to the cosine of the angle of incidence (Pesci and Teza, 2008; Pfeifer et al., 2008; Jutzi and Gross, 2009). Because the scans were acquired normal to the stope face, the incidence angle is considered zero. Because of these conditions, the distance correction applied during parsing by the Optech software was considered adequate for utilizing the intensity for identifying and differentiating ore from host rock in an underground environment.

3.4.4 Data Fusion and Processing

Pre-processing and intensity correction was followed by the creation of an ASCII file (.xyz) with 8-bit scaled intensity. The file contained data in the sequence *xyzi*, with *x*, *y*, and *z* being arbitrary coordinates, and *i* being the corrected intensity values. Following calibration of the Canon EOS camera on site at Optech, a calibration file was provided, which allowed for proper registration of the digital image with the lidar point cloud via Optech software named MatchView. A visualization of the workflow for the entire study is provided in Figure 3.3.

The registration software, Matchview, allows the user to register lidar point clouds with the corresponding digital camera images by identifying common points in each. By identifying a minimum of five common points, and confirming that the root mean square error (RMS) is below two pixels, new parameters for the camera calibration file are generated. This file is then used in the final step to fuse and register the two datasets correctly. The Optech Parser software was used again to output a 24-bit colour .xyz file, which contains the colourized point cloud. Data in this file is in the sequence *x, y, z, i, R, G, B*. The *xyz* coordinates are arbitrary, with the origin at the centre of the laser scanner. Intensity and the RGB values are both in 8-bit format.

The colourized point cloud was visualized in CloudCompare, and it was found that in order to achieve proper projection with the wall face-on, the *y* and *z* data had to be swapped. This re-projection was achieved by parsing the colourized point cloud to a .las file format (*x, z, y, i, R, G, B*) utilizing an ArcGIS extension named LP360. The next step was to convert these point clouds to a raster format, which was achieved by utilizing the ‘LAS dataset to Raster’ tool available in ArcGIS. Two separate raster images were generated; one as a single-band intensity raster, and the other being a 3-band passive visible imagery raster. Both files have a pixel size of 0.6 cm, and approximately 193,000 pixels in each scene. Lastly, the two rasters are imported into the image processing software ENVI for classification.

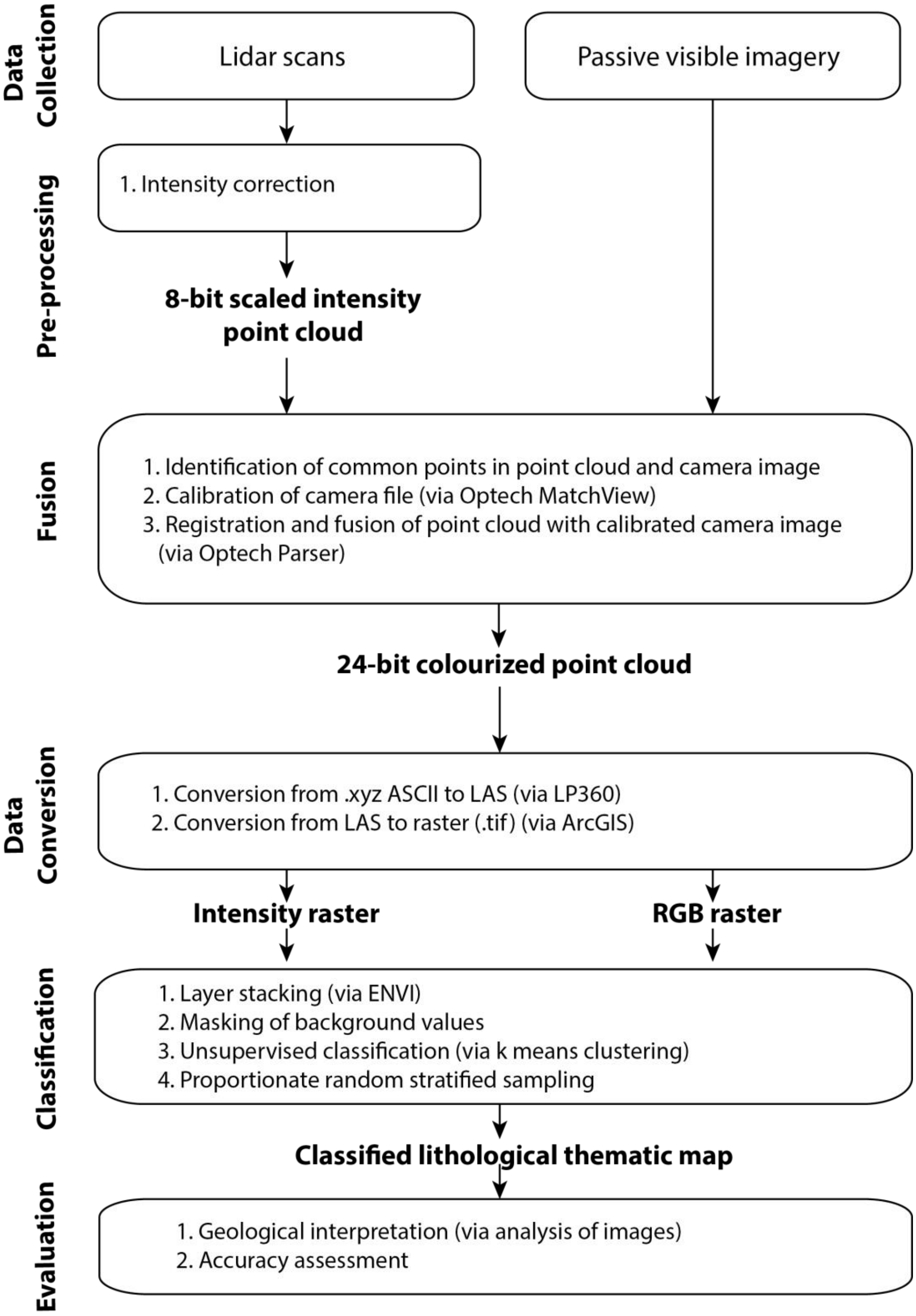

Figure 3.3. Workflow diagram showing the multiple steps required to produce a classified thematic map from the NRS scans. Data products highlighted in bold.

3.4.5 Unsupervised Classification

The final steps prior to application of the classification were to import the intensity raster and the RGB raster into ENVI, and to generate a mask for the images, which removes background data values that are outside of the 0-255 range. The two imported rasters were then stacked into a single 4-band layer, with the near infrared lidar intensity, Red, Green, and Blue bands being the variables incorporated for classification. A k-means clustering method was performed on the stacked image, with the initial output of 30 classes, which were then merged into three final classes; namely host rock, ore, and concrete and fencing. A 2% change threshold was applied to the clustering, with the process running through 10 iterations.

K-means is a clustering algorithm that partitions a population ‘N’ into ‘*k*’ classes. Initial cluster centres are randomly set and represented by the average of the pixel vectors allocated to them (Richards, 2013). The user can program how many iterations of clustering will occur, creating new cluster centres based on the similarity of the surrounding pixel vectors until the change threshold is below the specified percent, which in this study is 2%. The method of k-means clustering requires relatively little computational power, and can process large datasets with ease, which is optimal when working with lidar data, which generally will have millions of data points. The results of the k-means clustering is a classified thematic map, that should identify and discriminate between ore and the surrounding host rock, along with the concrete and fencing present in the scan area.

3.4.6 Accuracy Assessment

To assess the validity and accuracy of the clustering results, proportionate stratified random sampling was performed. This process consisted of generating a total of 505 random pixels within the newly classified thematic map, which were then manually compared to the geological map that was developed as the ground truth image. Distribution of the pixels for accuracy assessment can be seen in Table 3.2. The minimum sample size was set at 40 pixels (ore), which had the smallest amount of samples due to the fact that it comprised the least amount of area in the image. Host rock had 269 random pixels generated, while the concrete and fencing class had 196 random pixels. Ground truth for each of these pixels was derived from observation of the geological map of the image created via geological interpretation of the digital photographs taken and field observations while underground. Upon completion, the results were compiled, overall accuracy was assessed, and an error matrix was generated, which is presented below.

Table 3.3. Proportionate stratified random sampling pixel distribution for 3 classes present in the NRS stope face scan.

Class	Number of Random Samples
Host Rock	269
Ore	40
Concrete and Fencing	196

3.5 Results

3.5.1 Dry vs. Wet Scans

Scans of a stope face—containing ore, host rock, and construction materials such as concrete spray and fencing (including bolts)—were performed in an underground mine under low light conditions. Corresponding camera images were taken while the face was dusty and dry (Fig. 3.4a), which was followed by a thorough spray down of the face with water, upon which a second camera image was captured of the face (Fig. 3.4b). Figures 3.4c and 3.4d are images of the corresponding intensity returns for each of the scan conditions. For the scan performed under dusty target conditions (Figs. 3.4a and 3.4c), it is apparent that the intensities are relatively poorly distributed, with the entire image generally having intensity values in the upper half of the 0-255 range. The concrete spray and ore have nearly identical intensities, which would lead to low classification accuracy.

Similarly, as seen in Figure 3.4c, some of the host rock at the bottom of the image also has a very high intensity return, again leading to incorrect classification.

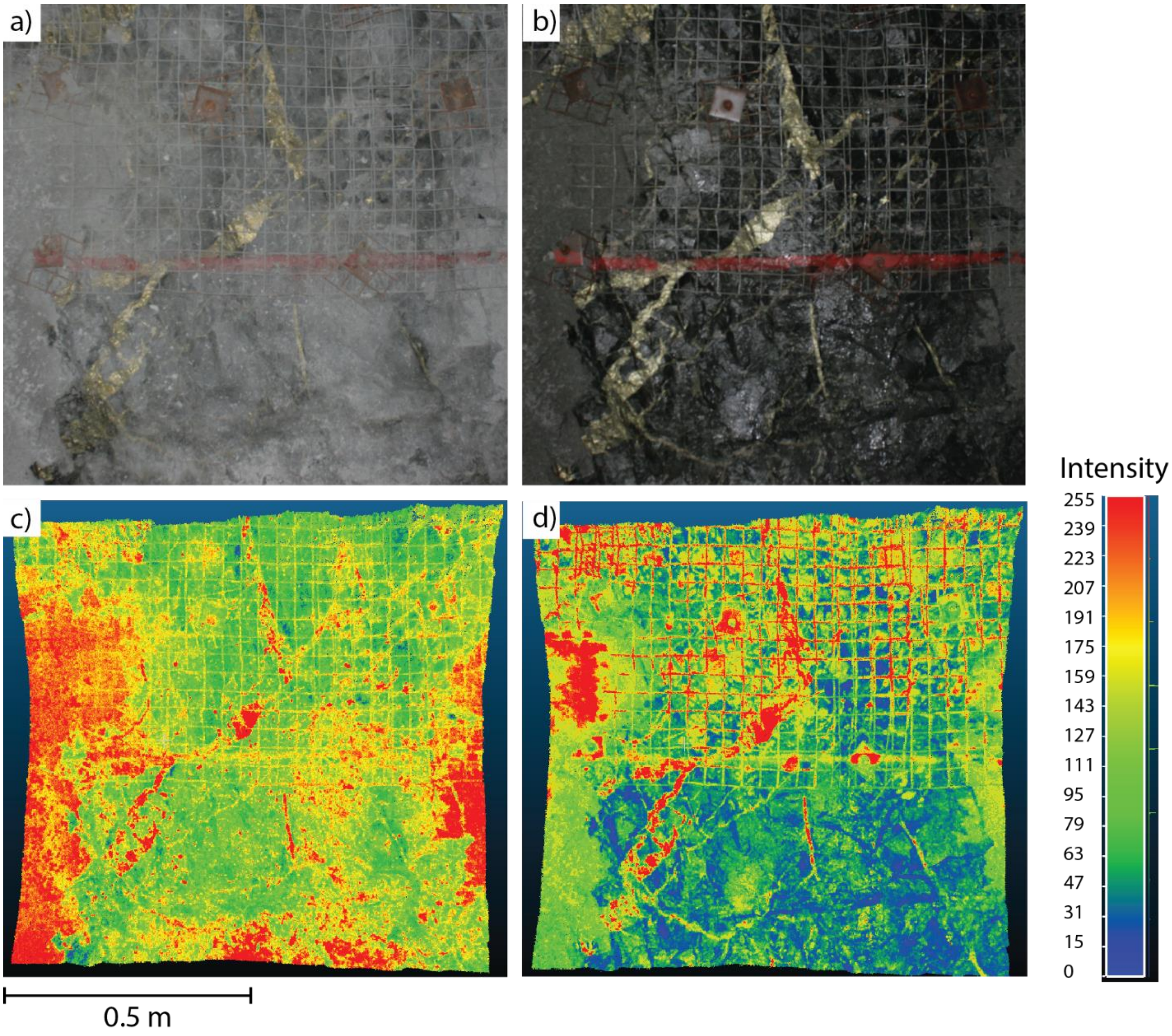

Figure 3.4. The effects of dust and water on the lidar intensity response. a) Passive visible imagery of the stope face in its original dusty condition. b) Passive visible imagery of the cleaned stope face after being washed. c) Corresponding intensity returns for the dusty stope face from a. d) Corresponding intensity returns for the cleaned stope face from b. Note the improved ability to identify the ore in the cleaned stope face intensity image.

In contrast, after the face was cleaned and hosed down with water, the intensity returns in Figure 3.4d are far more distributed and more easily distinguish between the materials present. Ore, with some of the highest intensities, can be identified quite well, with only minor confusion with some of the concrete spray on the left side of the image, along with some of the fencing. The host rock can now be identified much easier, with it returning the lowest intensity values (blue) in the image. The concrete spray along the right and left side of the image can now be differentiated from the ore. Due to these results, the cleaned face was chosen for further classification, with the belief that fusing the intensity image (Fig. 3.4d) with the passive visible imagery captured (Fig. 3.4b) would lead to far improved classification that with the dusty face.

3.5.2 Classification Results

Unsupervised classification via k-means clustering was performed on the fused dataset in order to identify three final classes: host rock, ore, and concrete and fencing materials. The input bands (Figs. 3.5a and 3.5b) and the results of the classification can be seen in Figure 3.5c. Class distributions were as follows: host rock = 48.5% of image; ore = 7.2% of image; concrete and fencing = 35.5%; unclassified = 8.8% of image. The classification accuracy was assessed by the generation of an error matrix, which was created by comparing the pixels in the classified thematic map (Fig. 3.5c) to the geological map (Fig. 3.5d). The error matrix can be seen in Table 3.3. The overall accuracy for the NRS thematic map is 73.3%. Producer’s and user’s accuracy were also assessed (Table 3.4), which represent the probability of a reference pixel being correctly classified, and the probability that a pixel classified on the map actually represents that class on the ground, respectively. The host rock class had the highest values for both producer’s (77.9%) and user’s (79.9%) accuracy, while the ore class had the lowest values for producer’s (43.9%), but a relatively strong user’s accuracy (72.5%), with 29 out of the 40 random pixels were correctly classified as ore. Concrete and fencing had a producer’s accuracy of 77.3%, and a user’s accuracy of 64.3%. The area of highest misclassification was with ore being incorrectly classified as host rock, which most often occurred on the perimeter of the ore stringers. The potential reasons for misclassification will be addressed in the following section.

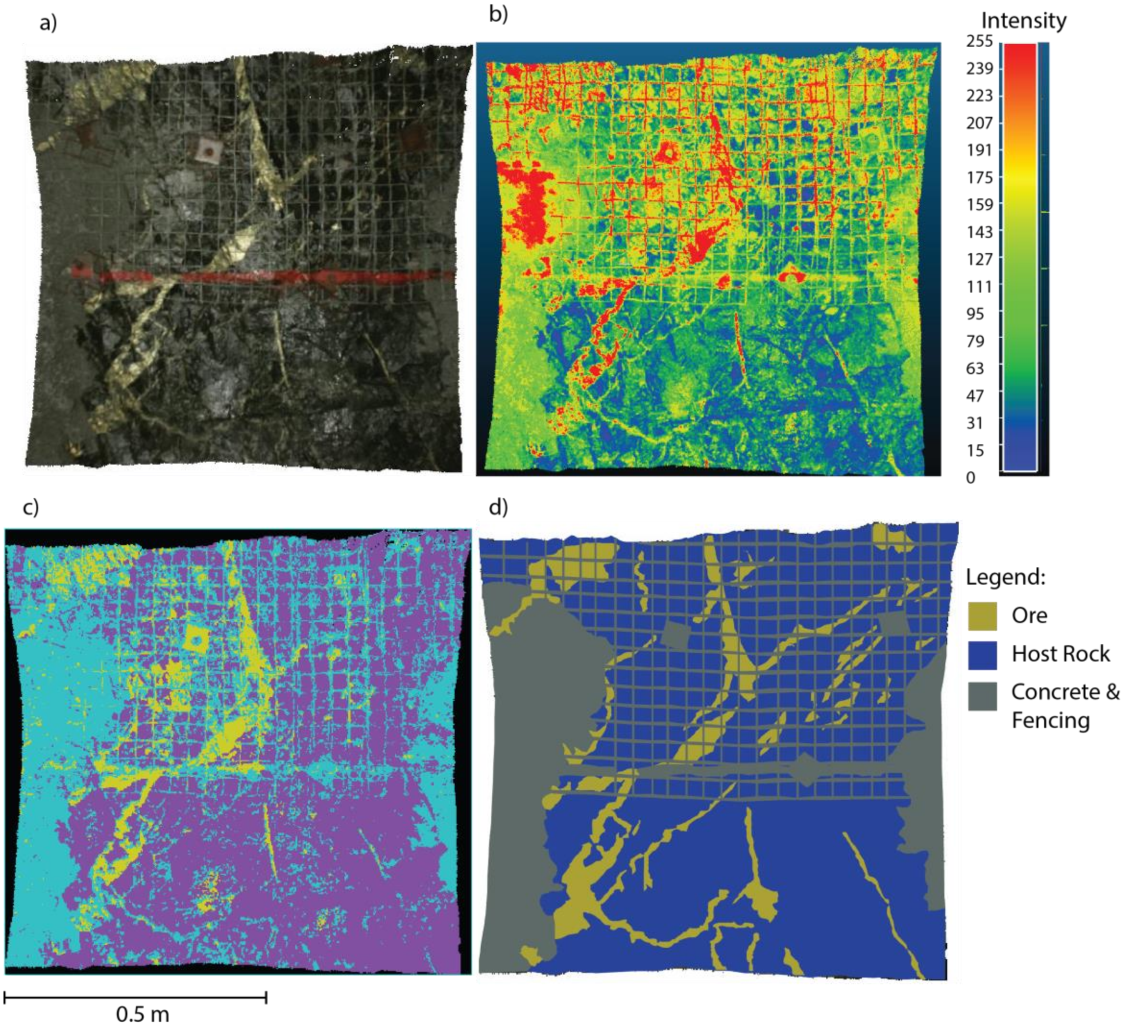

Figure 3.5. Input bands and results of k-means clustering with a 4-band fused dataset on a washed stope face including ore, host rock, concrete spray, and fencing. a) 3-band (RGB) passive visible imagery. b) Single band NIR lidar intensity. c) Results of k-means clustering (k = 3). Overall accuracy is 73%. d) Geological map of stope face used to confirm the accuracy of the clustering method.

Table 3.4. Percent error matrix for the NRS thematic map (k = 3)

Class	*Validation: Host Rock*	*Validation: Ore*	*Validation: Concrete and Fencing*	*Total*
Host Rock	77.9	34.9	19.0	53.3
Ore	1.8	43.9	3.7	7.9
Concrete and Fencing	20.3	21.2	77.3	38.8
Total	100.0	100.0	100.0	100.0

Table 3.5. Producer's and User's accuracy for the NRS thematic map (k = 3)

Producer's Accuracy (omission error)	
Host Rock = 215/276 = 77.9%	22.1% omission error
Ore = 29/66 = 43.9%	56.1% omission error
Concrete and Fencing = 126/163 = 77.3%	22.7% omission error
User's Accuracy (commission error)	
Host Rock = 215/269 = 79.9%	20.1% commission error
Ore = 29/40 = 72.5%	27.5% commission error
Concrete and Fencing = 126/196 = 64.3%	35.7% commission error
Overall Accuracy = 370/505 = 73.3%	

3.6 Discussion

3.6.1 Misclassification Factors

As seen in Table 3.4, the three class clustering led to an overall accuracy of 73.3%. As can be seen in Figure 3.5c and Table 3.3, the most misclassification was ore being incorrectly classified as host rock. Ore was incorrectly classified as host rock in 35% of instances, which could be due to a variety of reasons. First, the presence of the fencing in a gridded fashion over the rock leads to an increase in misclassification. These thin grids of metal can lead to some pixels having both the fencing and ore in them, making it difficult for the clustering method to confidently separate them. As can also be seen in Figures 3.5c and 3.5d, while one bolt (middle left of images) is classified as ore, another (middle right of images) is classified wholly as host rock. These errors are most likely due to the fact that the flash of the digital camera during data collection led to certain facets of the stope face to have increased reflectance, and others to be shadowed. For example, the bolt misclassified as ore was completely lit up by the flash, while the other bolt was hidden in shadow, leading to the incorrect classification of it as the darker host rock. Specular reflection from the metallic materials is also expected, which will affect the differentiation between the ore and some of the fencing material including the bolts. The lidar intensity returns are not as affected by this, due to the fact that they do not require ambient lighting. In some cases, it may be beneficial to only utilize the intensity returns.

Another possible factor in misclassification is due to the fact that the geological map of the image (Fig. 3.5d) may be slightly generalized and miss subtle lithological changes. While much effort was put into ensuring that the geological map created was as accurate as possible, very small stringers of ore were not always able to be incorporated into the final map.

To the knowledge of the authors, it is believed that this is the first time that lidar data has been used to distinguish ore from host rock in an underground environment. As noted previously, lidar has been increasingly utilized for 3D mapping and surface reconstruction of underground mines (Huber and Vandapel, 2006; Lemy et al., 2006;

Fekete et al., 2010; Zlot and Bosse, 2014), but no discrimination between lithologies occurred in any of these studies. This is also believed to be the first time k-means clustering has been utilized with a 4-band dataset in order to identify and discriminate between ore and host rock in an underground environment. TIR spectroscopy (Rivard et al., 2001) and visible/IR hyperspectral reflectance spectra (Gallie et al., 2002) have been collected from samples present in the mines of Sudbury, but on both occasions the samples were collected and then analyzed in a laboratory, and not under *in situ* conditions of the underground environment. In addition, neither of these methods allow for simultaneous acquisition of both 3D geospatial information along with scientific data. Campos Inocencio et al. (2014) have previously developed a proprietary k-means clustering software that has been applied to outcrops on the surface, but this clustering algorithm only uses the single near infrared band from the lidar response, and does not incorporate RGB values. Incorporating the RGB values into the dataset for the classification at NRS generally allows for more spectral differentiation, especially in areas that may be difficult to distinguish from intensity values alone. For example, as seen in Figure 3.5b, very high intensity values are attributed to both the ore and portions of the concrete spray, especially in the middle left section of the scan. The final classification is able to correctly differentiate between these two classes though, due to the incorporation of the RGB values.

Another study performed supervised classification on an outcrop at surface using a fused dataset of 6 bands, which included three different lidar instruments with different laser wavelengths, along with RGB values collected from passive visible imagery (Hartzell et al., 2014). The difference between these studies is that supervised classification requires an initial training set which the researcher classifies prior to running the classification algorithm, while unsupervised only requires manual input post-classification. This prior knowledge of an area may be impossible when performing lidar scans in an underground environment, as the stope may have been just blasted, uncovering new rock faces regularly, without time for the geologist to manually identify prior to more blasting. The utilization of lidar in the underground mining environment will be further addressed in Section 3.6.3.

3.6.2 Dust Cover and Moisture

As seen in Figures 3.4a and 3.4c, the thin layering of dust leads to a much smaller range of intensity values, that is much more difficult to differentiate between the classes present. Dust was also noted to be a factor of misclassification in aerial lidar scans of rural environments, which led to misclassification of asphalt as grass for example (Im et al., 2008). With this in mind, it is far more feasible to collect data that can be properly classified if the areas of interest are washed down in order to remove the dust. In optimal conditions, this would mean washing down and waiting until the face is dry, but it has been shown (Figs. 3.5c and 3.5d) that it is still feasible to differentiate and classify different rock units with a fused dataset on walls that are still wet. As stated previously, Burton et al. (2011) noted that the presence of water and ice in a scan area has a strong impact on the returned intensity (using a TLS operating at 1535 nm), leading to a noticeable decrease in intensity. These authors note that scans collected from the same outcrop on different occasions can only be considered valid if the collection occurred under similar conditions and at the same laser wavelength; as the collection of two scans, one in rainy conditions, and the other in sunny conditions, will lead to intensity values that are not able to be reconciled (Burton et al., 2011). In regards to scans underground in a mining environment, this means that if scans are taken with a wet, washed face, future scans should also occur with those same conditions. As noted by Zlot and Bosse (2014), some mines use a misting spray to tamp down the dust, which would be very beneficial when attempting to collect high quality lidar data.

3.6.3 Utilization of Lidar in Mining Environments

As terrestrial and mobile lidar technology becomes smaller and faster, it is becoming apparent that there are many benefits of incorporating this into the underground mining environment. This speed and size of these instruments are allowing for collection of detailed 3D geospatial information of the mine workings, along with simultaneous acquisition of scientific data via the near infrared intensity returns, which under the proper conditions can be used to discriminate between ore and gangue. Lidar scanners have already been used in mines for geotechnical surveys, including for deformation analysis of bored tunnels (van Gosliga et al., 2006), along with detecting convergence (the deformation of rock due to stress) in underground mines (Vanderbeck, 2016). Terrestrial lidar scanners have also been utilized for identification of concrete spray thickness, bolt spacing, and identifying areas of possible leakage (Fekete et al., 2010), all of which aid in providing very high resolution data which the mine engineers can use for modelling and increased safety assessment. These authors also note that lidar allows the worker to identify the orientation (strike and dip) and large scale roughness of the scanned walls (Fekete et al., 2010). This study builds upon this and shows that it is very feasible to characterize ore rock in the stope faces and differentiate it from surrounding host rock utilizing current lidar technology. For future studies, small, mobile lidar units could be mounted on the back of mine trucks, collecting high-resolution data as soon as the stope faces have been blasted. These rapid scans would allow for immediate assessment by mine geologists at the surface, potentially removing the necessity for them to go underground. Often by the time a geologist makes it to the ore face to manually determine the distribution and grade of the ore, the face could have been blasted multiple times, forcing the geologist to make extrapolations of the ore body from the last time they observed the face. The utilization of lidar could remove this issue, and by creating tie points between the point clouds for each scan, the geologist could generate a time-sequenced cloud that would allow the user to see how the relationship between the ore and host rock has changed as blasting continues further into the rock. These slices of information would potentially allow for the development of a 3D ore body model over time, and lead to important new information, such as the dip direction of ore stringers, or the presence of a major fault which is affecting mineralization. These multiple benefits of utilizing lidar in underground environments should lead to increased efficiency and safety; something that every mine strives for on a daily basis.

3.7 Concluding Remarks and Recommendations

In this study we have found that the fusion of near infrared distance corrected intensity with passive visible imagery for classification of ore and host rock via k-means clustering was successful, with an overall accuracy of 73% (k = 3). A thematic map differentiating ore from host rock and construction materials was established for this classification and is shown in Figure 3.5c. It was also confirmed that the presence of dust as a coating on the mine walls acts to skew the intensity values, and leads to decreased classification accuracy. This new approach of performing unsupervised classification via k-means clustering on a 4-band fused dataset has led to the successful differentiation of ore from host rock. It is hoped that this process will assist in creating a safer and more efficient underground mining environment.

Several recommendations for future work utilizing lidar for ore discrimination in underground environments are presented below:

- If data fusion is to be used by merging lidar intensity and RGB images, it is recommended to ensure a powerful enough light source behind the instrument as to remove shadows from the captured passive visible images.

- In order to have increased classification accuracy scans should be performed on cleaned walls absent of dust. It is also recommended to perform the scans prior to the fencing and bolts being installed, which will remove extraneous factors and increase classification accuracy.

- A follow-up to this study could be to utilize a white light lidar to perform scans on stope faces underground, which collects data at multiple wavelengths. These extra wavelengths could be coupled with the 4-bands utilized in this study, or even as stand-alone data, removing the necessity of capturing passive visible imagery, which as noted above, requires ambient lighting. While white light lidar is not eye safe, the ability to perform this autonomously from the back of a mine truck on an empty stope would prevent human interaction with the instrument while it is collecting data. Also, the consecutive collection of lidar data on the same stope as blasting continues may very well allow for volumetric analysis of ore content in the stope face over time, constraining ore models, and leading to increased confidence in resource estimates.

3.8 References

Ames, D.E., Kjarsgaard, I.M. and Douma, S.L., 2003, Sudbury Ni-Cu-PGE ore mineralogy compilation: Sudbury targeted geoscience initiative, Geological Survey of Canada Open File 1787, CD-ROM.

Ames, D.E., Davidson, A., and Wodicka, N., 2008, Geology of the Giant Sudbury Polymetallic Mining Camp, Ontario, Canada: Economic Geology, v. 103, no. 5, p. 1057–1077, doi: 10.2113/gsecongeo.103.5.1057.

Burton, D., Dunlap, D.B., Wood, L.J., and Flaig, P.P., 2011, Lidar Intensity as a Remote Sensor of Rock Properties: Journal of Sedimentary Research, v. 81, no. 5, p. 339–347, doi: 10.2110/jsr.2011.31.

Campos Inocencio, L., Veronez, M.R., Wohnrath Tognoli, F.M., De Souza, M.K., Da Silva, R.M., Gonzaga, L., and Blum Silveira, C.L., 2014, Spectral pattern classification in lidar data for rock identification in outcrops: The Scientific World Journal, v. 2014, p. 1–10, doi: 10.1155/2014/539029.

Carrea, D., Abellan, A., Humair, F., Matasci, B., Derron, M.-H., and Jaboyedoff, M., 2016, Correction of terrestrial LiDAR intensity channel using Oren–Nayar reflectance model: An application to lithological differentiation: ISPRS Journal of Photogrammetry and Remote Sensing, v. 113, p. 17–29, doi: 10.1016/j.isprsjprs.2015.12.004.

Dietz, R.S., 1964, Sudbury structure as an astrobleme: The Journal of Geology, v. 72, no. 4, p. 412–434, doi: 10.1086/626999.

Fekete, S., Diederichs, M., and Lato, M., 2010, Geotechnical and operational applications for 3-dimensional laser scanning in drill and blast tunnels: Tunnelling and Underground Space Technology, v. 25, no. 5, p. 614–628, doi: 10.1016/j.tust.2010.04.008.

Franceschi, M., Teza, G., Preto, N., Pesci, A., Galgaro, A., and Girardi, S., 2009, Discrimination between marls and limestones using intensity data from terrestrial laser scanner: ISPRS Journal of Photogrammetry and Remote Sensing, v. 64, no. 6, p. 522–528, doi: 10.1016/j.isprsjprs.2009.03.003.

Gallie, E. a., McArdle, S., Rivard, B., and Francis, H., 2002, Estimating sulphide ore grade in broken rock using visible/infrared hyperspectral reflectance spectra: International Journal of Remote Sensing, v. 23, no. 11, p. 2229–2246, doi: 10.1080/01431160110075604.

Girardeau-Montaut, D., 2016, Cloudcompare, a 3D Point Cloud and Mesh Processing Free Software. <www.cloudcompare.org> (accessed on 06.05.2016).

van Gosliga, R., Lindenbergh, R., and Pfeifer, N., 2006, Deformation analysis of a bored tunnel by means of terrestrial laser scanning: Proceedings of the ISPRS Commission V Symposium on Image Engineering and Vision Metrology, v. XXXVI, Par, p. 167–172.

Grieve, R. a. F., Stoffler, D., and Deutsch, A., 1991, The Sudbury Structure - controversial or misunderstood? Journal of Geophysical Research-Planets, v. 96, no. E5, p. 22753–22764, doi: 10.1029/91je02513.

Hartzell, P., Glennie, C., Biber, K., and Khan, S., 2014, Application of multispectral LiDAR to automated virtual outcrop geology: ISPRS Journal of Photogrammetry and Remote Sensing, v. 88, p. 147–155, doi: 10.1016/j.isprsjprs.2013.12.004.

Höfle, B., and Pfeifer, N., 2007, Correction of laser scanning intensity data: Data and model-driven approaches: ISPRS Journal of Photogrammetry and Remote Sensing, v. 62, no. 6, p. 415–433, doi: 10.1016/j.isprsjprs.2007.05.008.

Huber, D.F., and Vandapel, N., 2006, Automatic Three-dimensional Underground Mine Mapping: The International Journal of Robotics Research, v. 25, no. 1, p. 7–17, doi: 10.1177/0278364906061157.

Hunt, G. R., Salisbury, J. W., and Lenhoff, C. J., 1971, Visible and near-infrared spectra of minerals and rocks IV. Sulphides and sulphates. Modern Geology, 3, 1–14.

Im, J., Jensen, J.R., and Hodgson, M.E., 2008, Object-Based Land Cover Classification Using High-Posting-Density LiDAR Data: GIScience & Remote Sensing, v. 45, no. 2, p. 209–228, doi: 10.2747/1548-1603.45.2.209.

Jelalian, A.V., 1992, Laser Radar Systems. Artech House, Boston London.

Jensen, J.R. 2007, Remote sensing of the environment: An earth resource perspective (2nd edition). Prentice Hall, Upper Saddle River, NJ.

Jutzi, B., and Gross, H., 2009, Normalization of Lidar Intensity Data Based on Range and Surface Incidence Angle: The International Archives of the Photogrammetry, Remote Sensing and Spatial Information Sciences 38 (Part 3/W8), v. XXXVIII, no. 2006, p. 213–218.

Kaasalainen, S., Jaakkola, A., Kaasalainen, M., Krooks, A., and Kukko, A., 2011, Analysis of incidence angle and distance effects on terrestrial laser scanner intensity: Search for correction methods: Remote Sensing, v. 3, p. 2207–2221, doi: 10.3390/rs3102207.

Kashani, A.G., Olsen, M.J., Parrish, C.E., and Wilson, N., 2015, A review of LIDAR radiometric processing: From ad hoc intensity correction to rigorous radiometric calibration: Sensors (Switzerland), v. 15, no. 11, p. 28099–28128, doi: 10.3390/s151128099.

Krooks, a., Kaasalainen, S., Hakala, T., and Nevalainen, O., 2013, Correction of Intensity Incidence Angle Effect in Terrestrial Laser Scanning: Annals of Photogrammetry, Remote Sensing and Spatial Information Sciences, v. II-5/W2, no. June 2015, p. 145–150, doi: 10.5194/isprsannals-II-5-W2-145-2013.

Lemy, F., Yong, S., and Schulz, T., 2006, A case study of monitoring tunnel wall displacement using laser scanning technology, in Proceedings of the 10th Congress of the International Association for Engineering Geology and the Environment - Engineering geology for tomorrow’s cities, p. 1–11.

Matasci, B., Carrea, D., Abellan, A., Derron, M.H., Humair, F., Jaboyedoff, M., and Metzger, R., 2015, Geological mapping and fold modeling using terrestrial laser scanning point clouds: Application to the Dents-du-Midi limestone massif (Switzerland): European Journal of Remote Sensing, v. 48, p. 569–591, doi: 10.5721/EuJRS20154832.

McLean, S.A., Straub, K.H., and Stevens, K.M., 2005, The discovery and characterization of the Nickel Rim South deposit, Sudbury, Ontario: Mineralogical Association of Canada, Short Course 35, p. 359–368.

Optech, 2016, ILRIS Terrestrial Laser Scanner: Summary Specification Sheet, <http://www.teledyneoptech.com/wp-content/uploads/ILRIS-Spec-Sheet-140730-WEB.pdf> (accessed on 07.07.16).

Osinski, G.R., Barfoot, T.D., Ghafoor, N., Izawa, M., Banerjee, N., Jasiobedzki, P., Tripp, J., Richards, R., Auclair, S., Sapers, H., Thomson, L., and Flemming, R., 2010, Lidar and the mobile Scene Modeler (mSM) as scientific tools for planetary exploration: Planetary and Space Science, v. 58, no. 4, p. 691–700, doi: 10.1016/j.pss.2009.08.004.

Penasa, L., Franceschi, M., Preto, N., Teza, G., and Polito, V., 2014, Integration of intensity textures and local geometry descriptors from Terrestrial Laser Scanning to map chert in outcrops: ISPRS Journal of Photogrammetry and Remote Sensing, v. 93, p. 88–97, doi: 10.1016/j.isprsjprs.2014.04.003.

Pentek, A., Molnar, F., Watkinson, D.H., and Jones, P.C., 2008, Footwall-type Cu-Ni-PGE Mineralization in the Broken Hammer Area, Wisner Township, North Range, Sudbury Structure: Economic Geology, v. 103, no. 5, p. 1005–1028, doi: 10.2113/gsecongeo.103.5.1005.

Pesci, A., and Teza, G., 2008, Effects of surface irregularities on intensity data from laser scanning: An experimental approach: Annals of Geophysics, v. 51, no. 5-6, p. 839–848, doi: 10.4401/ag-4462.

Pesci, A., Teza, G., and Ventura, G., 2008, Remote sensing of volcanic terrains by terrestrial laser scanner: preliminary reflectance and RGB implications for studying Vesuvius crater (Italy): Annals of Geophysics, v. 51, no. 4, p. 633–653, doi: 10.4401/ag-4455.

Pfeifer, N., Höfle, B., Briese, C., Rutzinger, M., and Haring, A., 2008, Analysis of the backscattered energy in terrestrial laser scanning data: Int. Arch. Photogramm. Remote Sens. Spat. Inf. Sci., v. 37, p. 1045–1052.

Pfeifer, N. and Briese, C., 2007, Geometrical aspects of airborne laser scanning and terrestrial laser scanning: International Archives of Photogrammetry, Remote Sensing and Spatial Information Sciences, v. XXXVI, p. 311–319.

Richards, J. A., 2013, Remote Sensing Digital Image Analysis: An Introduction (5th ed), Springer.

Rivard, B., Feng, J., Gallie, E.A., and Francis, H., 2001, Case History Ore detection and grade estimation in the Sudbury mines using thermal infrared reflectance spectroscopy: Geophysics, v. 66, no. 6, p. 1691 – 1698, doi: 10.1190/1.1487111.

Vanderbeck, R., 2016, A Bayesian Approach to Convergence Detection in Underground Excavations using LiDAR: M. Sc. Thesis, Queen’s University, Kingston, p. 122. (retrieved from http://hdl.handle.net/1974/14339).

Wagner, W., Ullrich, A., Ducic, V., Melzer, T., and Studnicka, N., 2006, Gaussian decomposition and calibration of a novel small-footprint full-waveform digitising airborne laser scanner: ISPRS Journal of Photogrammetry and Remote Sensing, v. 60, no. 2, p. 100–112, doi: 10.1016/j.isprsjprs.2005.12.001.

Zlot, R., and Bosse, M., 2014, Efficient Large-Scale 3D Mobile Mapping and Surface Reconstruction of an Underground Mine, in Springer Tracts in Advanced Robotics, p. 479–493.

Chapter 4

4 Discussion and Conclusions

As exploration continues in the modern era, new and novel techniques are continuously being developed to aid in probing uncharted territory, with the aim of furthering humanity’s understanding of the universe around us. This ever increasing remoteness that is associated with modern exploration—be it the expanses of the ocean, the depths of mines, or even the robotic exploration of other planets—requires a level of autonomy in order to reduce human risk and efficiently collect scientific data. One of the greatest limiting factors that hampers the collection of scientific data in remote regions is time. The advent of technology such as lidar has begun to allow rapid collection of high resolution data that can be used as a navigational and scientific tool for exploration. Especially powerful for long range acquisition when contact science may not be possible, lidar is proving to be an excellent tool for geological mapping of inaccessible regions, providing both a three dimensional documentation of the scanned area along with spectral information from the intensity wavelength (Pesci et al., 2008; Burton et al., 2011; Matasci et al., 2015). After corrections, this intensity value can be used to differentiate between lithologies, and when combined with semi-autonomous image classification, lidar can become a powerful tool for establishing preliminary geological maps.

The results presented in Chapters 2 and 3 show the feasibility of using terrestrial lidar intensity data and passive visible imagery in a semi-autonomous classification method in order to generate relatively accurate geological maps for outcrops in both a remote Arctic setting and in an underground mine. This is believed to be the first time that a 4-band dataset composed of near infrared lidar intensity returns and RGB passive visible imagery have been used to discriminate lithology using the unsupervised classification technique of k-means clustering. It is hoped that this application of lidar can serve as a tool for geoscientists and planetary scientists alike, on or off Earth.

As noted in Chapter 3, to the authors’ knowledge, this is the first time that lidar scans have been utilized in order to discriminate ore from host rock in a subsurface mine. It is hoped that this novel approach can be incorporated into the mine geologist's toolset, generating relatively accurate preliminary geological maps of the active face. As lidar instrumentation continues to become smaller, it will become even easier to efficiently perform scans semi-autonomously, or even fully autonomous, further increasing the safety in mines.

As described in Section 2.5.2 and Section 3.6.1, minor error may be associated with the algorithm-generated maps, which are due to several possible factors. For the Tunnunik scans, overall accuracy was improved by 16.8% when the shale classes were combined into one. While lidar intensity performs admirably when it is scanning lithologies of distinct colour and composition, it is more difficult to distinguish between the subtle differences of three varieties of shale. Another factor that can lead to possible errors is the presence of shadowed areas in the passive visible imagery, which can act to confuse the clustering algorithm and lead to incorrect classification. Lastly, the presence of dust and extraneous materials such as the fencing seen in Figures 3.3 and 3.4 can also act to confuse the classifier.

However, while typically not discussed, there is always human subjectivity when creating a geological map based on visual analysis, which can also lead to "errors". For example, geological contacts are rarely ever continuous, requiring field geologists to "infer" where the boundary is. Human subjectivity also comes into play when there are gradational boundaries between rock types, which means that it is impossible to distinguish an exact location where the boundary should be (Lark et al., 2015). Further human error can be incorporated when field notes and rough drawings of geological maps become published material, oftentimes due to the fact that the published map has a different cartographic scale, leading to further generalizations on where the geological units truly are (Lark et al., 2015).

Using a computer-assisted method to rapidly extract, analyze, and classify geological information could, therefore, potentially lead to a more quantitative and systematic classification of the lithologies present. While not removing the importance of the geologist for final validation of the classification, these preliminary geological maps could be generated independently from human input, which is vital in extreme and remote environments such as in underground mines and on other planetary bodies. In addition to potentially leading to increased accuracy, the utilization of lidar underground can be performed remotely and safely, mitigating human risk. Scans could also be scaled up substantially, potentially being performed on quarry faces that are hundreds of metres in size. The rapid collection of a dense point cloud would mean that the entire quarry face could be scanned in a matter of minutes, again leading to greater efficiency.

The main findings of Chapters 2 and 3 are summarized below:

- Mineral composition can be semi-quantitatively correlated with distance-corrected lidar intensity. Intensity displays a positive linear relationship with weight percent (wt. %) dolomite, with a R^2 value of 0.63. Intensity is also seen to display a negative linear relationship with both shale and feldspars, with R^2 values of 0.73 and 0.59, respectively. The negative relationship with feldspar is most likely due to its exclusive association with the shale, and is not necessarily a rule for feldspar.

- The fusion of near infrared distance-corrected lidar intensity with passive visible imagery for lithological discrimination via k-means clustering was deemed successful for both the Tunnunik outcrop scan and the Nickel Rim South mine stope face scan.
  - Two separate classifications were performed on the Tunnunik outcrop scan. First, a four-class clustering occurred, differentiating dolostone and three variations of shale, with an overall accuracy of 68.8%. Second, a two-class clustering process was performed, combining the three shale lithologies into one, along with dolostone. Overall accuracy increased substantially, at 85.6%.

    - A three-class clustering process was performed on the Nickel Rim South mine stope face scan. The k-means clustering was able to successfully differentiate between ore, host rock, and construction material on a cleaned wall with an overall accuracy of 73%.

- The presence of dust as a coating on mine walls acts to skew the intensity returns, which leads to decreased classification accuracy. The presence of fencing also acts to decrease classification. It was found that scans should be performed on clean walls prior to fencing being installed in order for increased classification accuracy, and therefore more accurate modelling of the amount of ore present in a particular stope face.

4.1 Future Work

There are several avenues of possible further investigation that arose during the course of this thesis. Two are described below.

1. As the field of utilizing lidar for geological applications is still in its infancy, there is still no standardized correction method for intensity that can be applied for all situations (Kashani et al., 2015). In order to increase the value of utilizing lidar intensity returns as a scientific tool, efforts must be made to find a standardized correction method that can account for multiple variables at once. While it may be feasible in some situations to perform a stationary scan normal to a rock face such as performed in this investigation, in other cases it may not be. Establishing a method that could account for the variations in both range and incidence angle for a mobile lidar device mounted on a rover or mine truck would allow for extremely rapid return of valuable geospatial and lithologic data. If this can be accomplished, it is not unlikely that reflectance values from the corrected

intensity could be available immediately through the hardware, instead of requiring later processing by humans.

2. The lithological differentiation provided by corrected intensity returns proves that it may be beneficial to add lidar as another suite of data for remote predictive mapping. Remote predictive mapping (RPM) is the compilation and interpretation of many suites of geoscientific data in order to support field mapping by geologists on the ground (Harris et al., 2012). RPM is currently used in the Canadian Arctic, to assist in mapping this expansive and remote region of Earth. The majority of data suites utilized in RPM today are satellite based, and include LANDSAT, RADARSAT, ASTER, among others, which provide structural and spectral information (Harris et al., 2012). Airborne-based hyperspectral data can sometimes also be incorporated, which can assist in mapping spectral units, geological structures, and alteration (Harris et al., 2012). The rationale for incorporating lidar as another suite for RPM include the fact that it could provide extremely precise digital elevation coordinates, as well as the fact that it's near infrared intensity wavelength could be utilized as another band to spectrally differentiate geologic units. By mounting lidar onto unmanned aerial vehicles (UAVs) and performing scans over a pre-programmed route, precise and high resolution data could be collected autonomously, and incorporated into a RPM. While the satellite-based data could provide data over large swaths of land with low spatial resolution, lidar could compliment this by providing much higher spatial resolution over specific areas, and over time as UAV technology improves, this high spatial resolution lidar data could potentially encompass the same expansive areas as the satellite-based data.

4.2 References

Burton, D., Dunlap, D.B., Wood, L.J., and Flaig, P.P., 2011, Lidar Intensity as a Remote Sensor of Rock Properties: Journal of Sedimentary Research, v. 81, no. 5, p. 339–347, doi: 10.2110/jsr.2011.31.

Harris, J., Schetselaar, E., and Behnia, P., 2012, Remote Predictive Mapping : An Approach for the Geological Mapping of Canada’s Arctic: Earth Sciences, , no. August 2016, p. 495–525, doi: 10.5772/25475.

Kashani, A.G., Olsen, M.J., Parrish, C.E., and Wilson, N., 2015, A review of LIDAR radiometric processing: From ad hoc intensity correction to rigorous radiometric calibration: Sensors (Switzerland), v. 15, no. 11, p. 28099–28128, doi: 10.3390/s151128099.

Lark, R.M., Lawley, R.S., Barron, a. J.M., Aldiss, D.T., Ambrose, K., Cooper, a. H., Lee, J.R., and Waters, C.N., 2015, Uncertainty in mapped geological boundaries held by a national geological survey:eliciting the geologists’ tacit error model: Solid Earth, v. 6, no. 2, p. 727–745, doi: 10.5194/se-6-727-2015.

Matasci, B., Carrea, D., Abellan, A., Derron, M.H., Humair, F., Jaboyedoff, M., and Metzger, R., 2015, Geological mapping and fold modeling using terrestrial laser scanning point clouds: Application to the Dents-du-Midi limestone massif (Switzerland): European Journal of Remote Sensing, v. 48, p. 569–591, doi: 10.5721/EuJRS20154832.

Pesci, A., Teza, G., and Ventura, G., 2008, Remote sensing of volcanic terrains by terrestrial laser scanner: preliminary reflectance and RGB implications for studying Vesuvius crater (Italy): Annals of Geophysics, v. 51, no. 4, p. 633–653, doi: 10.4401/ag-4455.

Appendix

Powder X-Ray Diffraction Patterns:

Sample TH-15-25

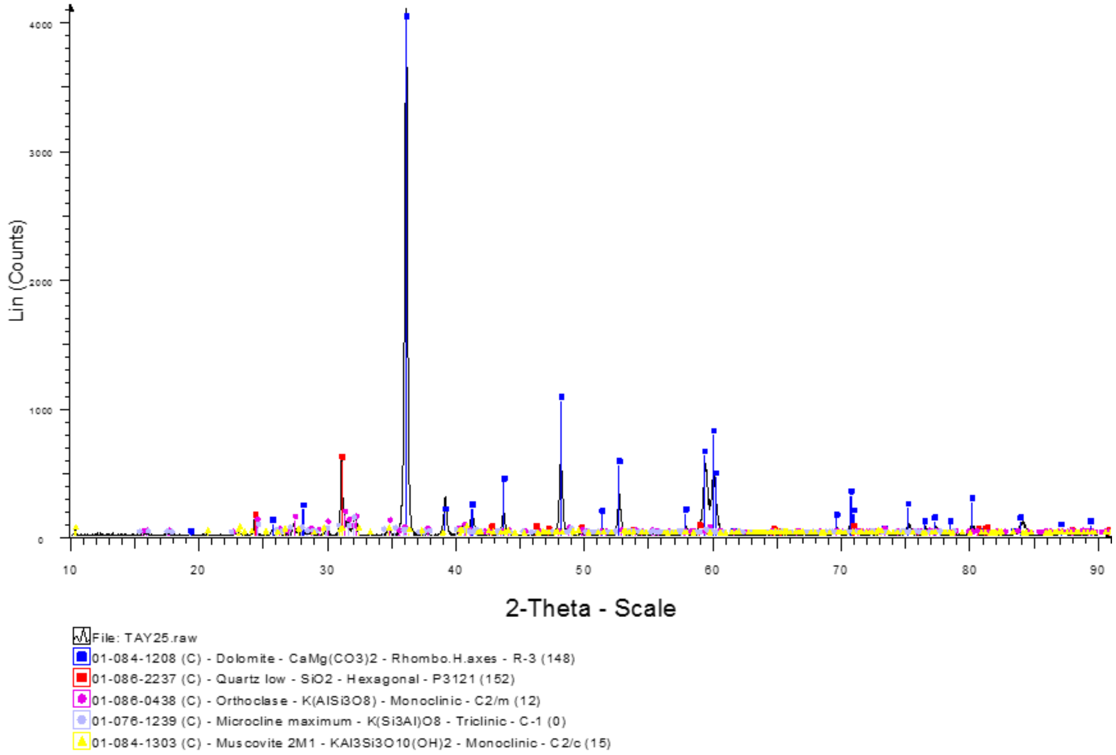

Sample TH-15-71a

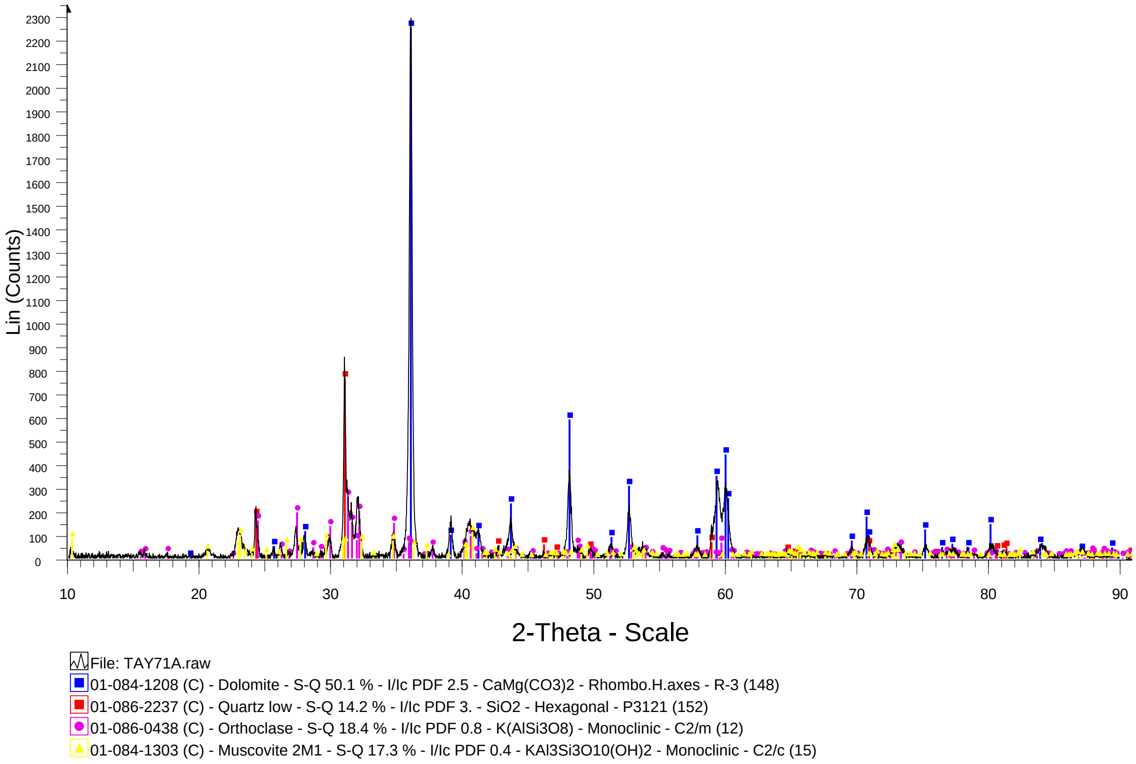

Sample TH-15-71b

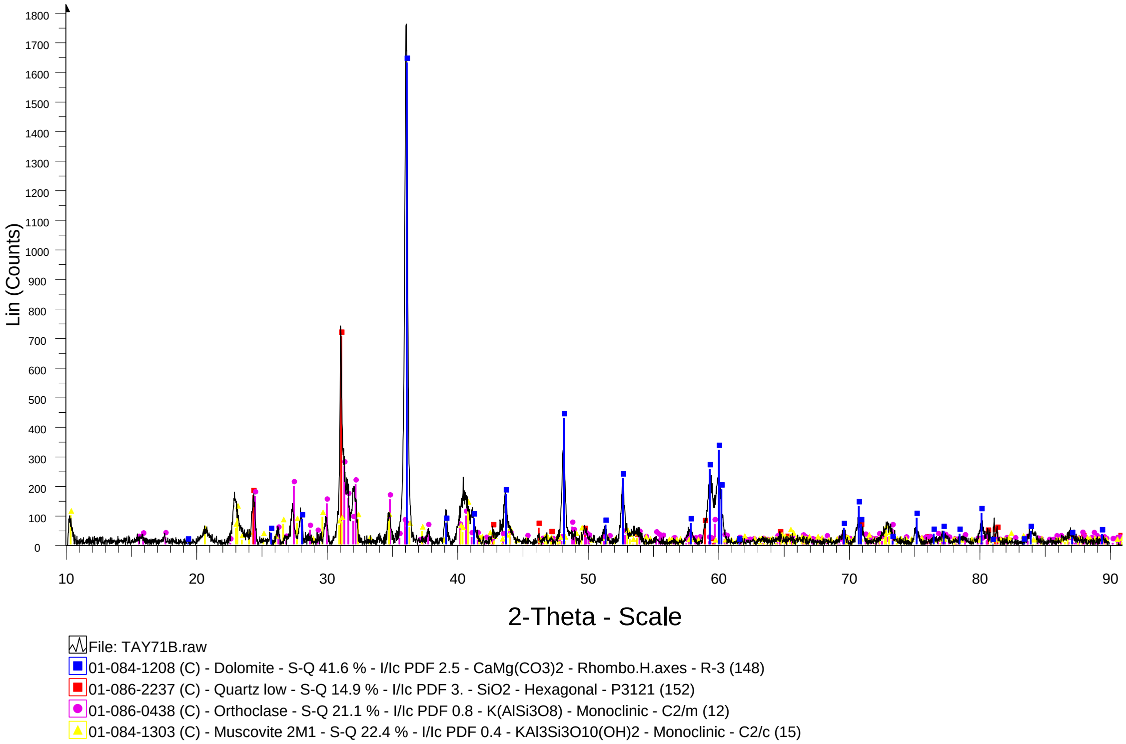

Sample TH-15-107

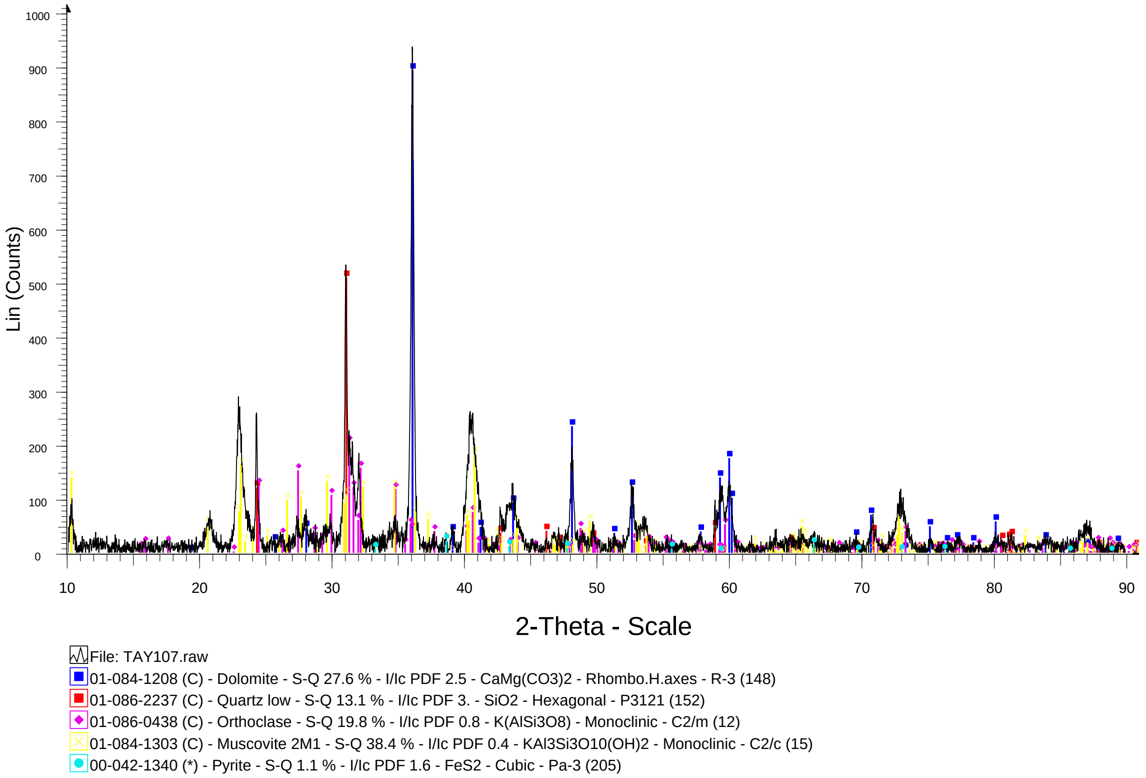

Sample TH-15-103

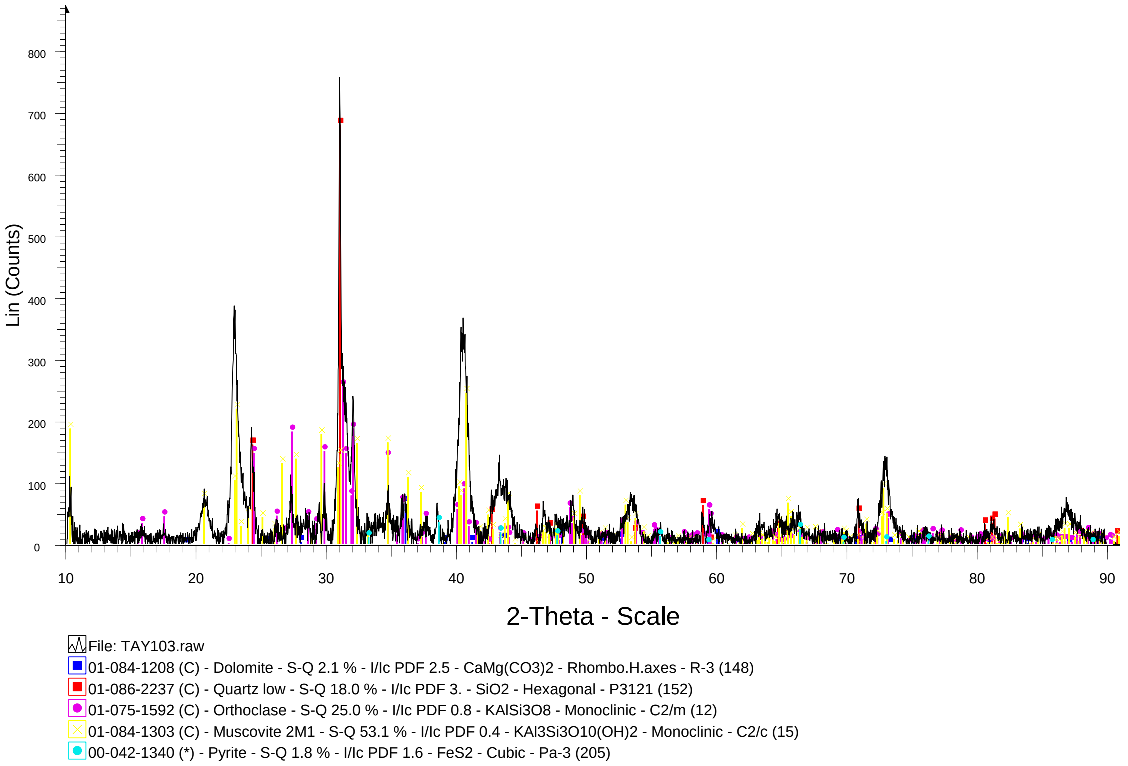

Sample TH-15-102

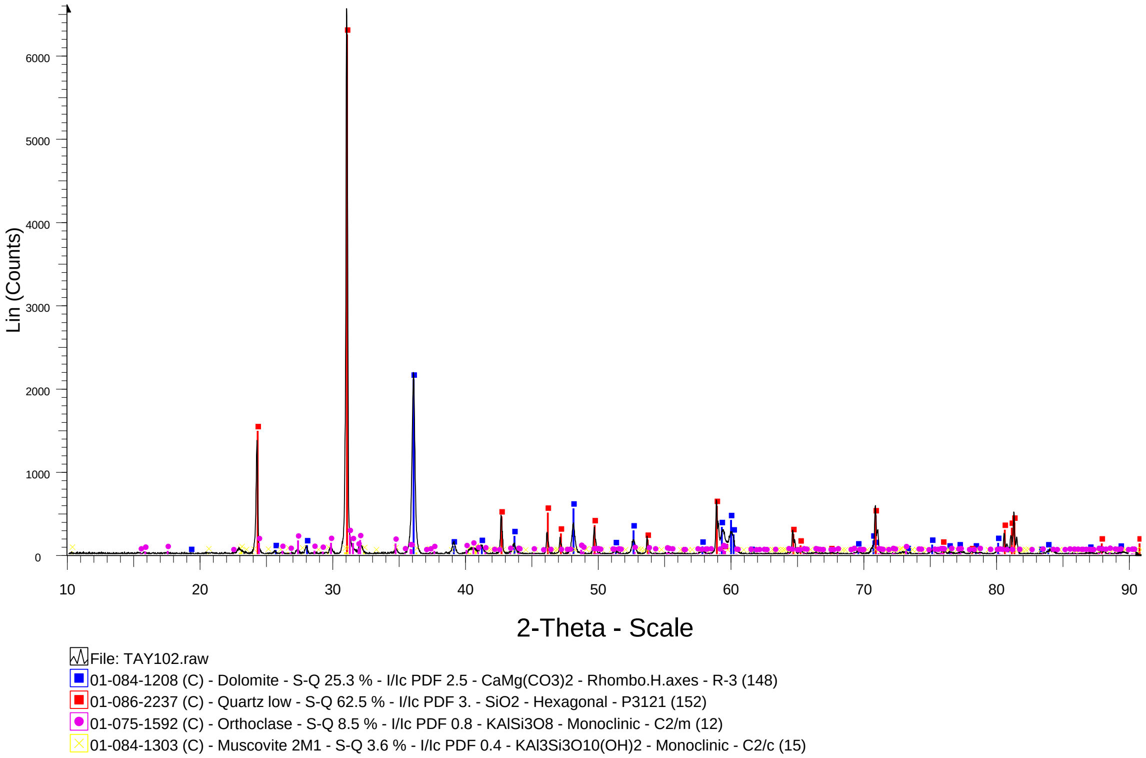

Sample TH-15-68

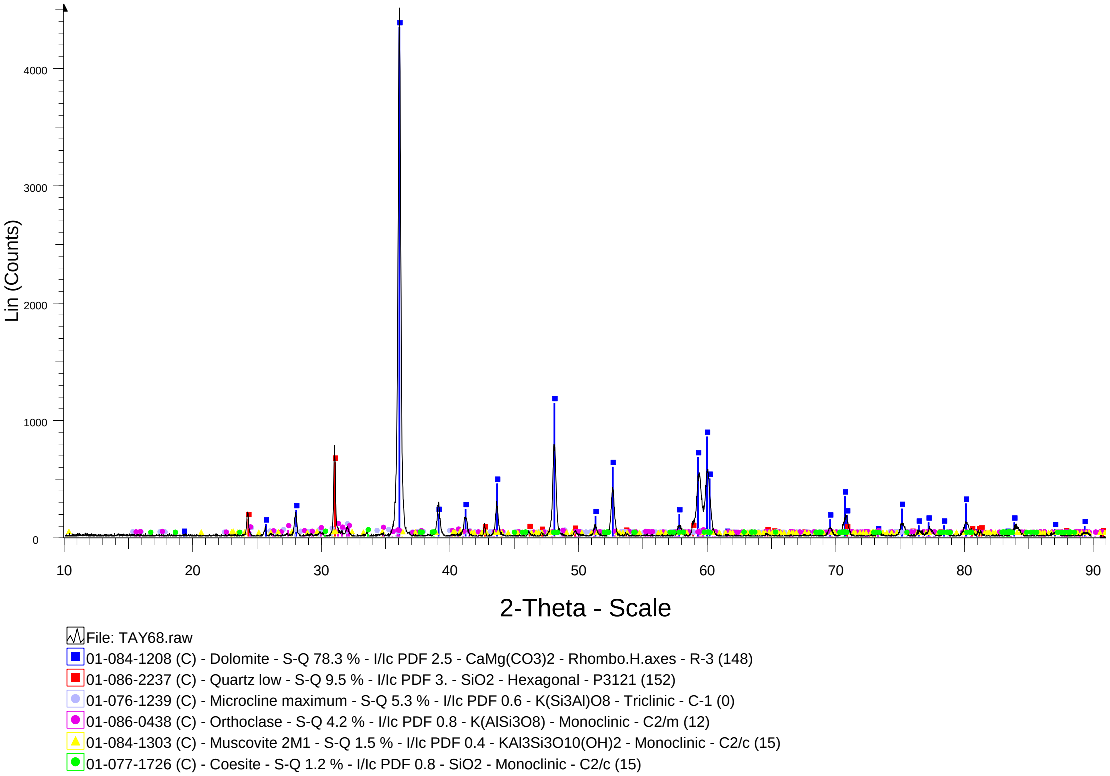

Sample TH-15-92

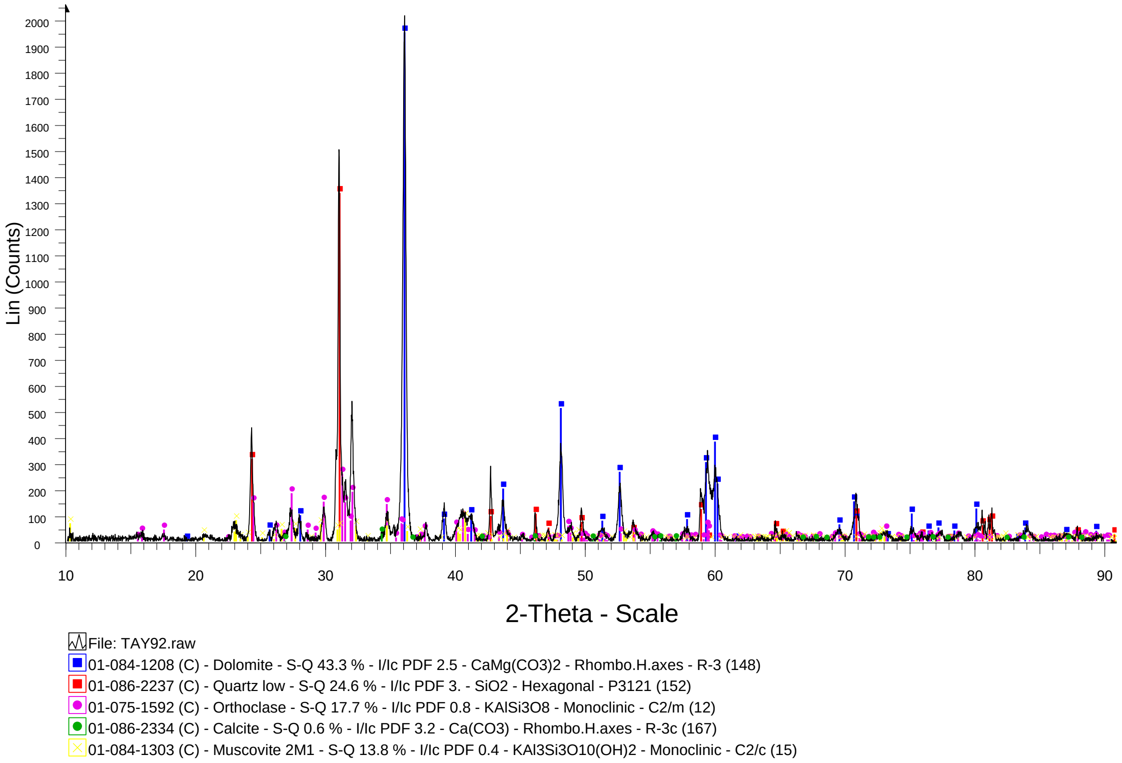

Sample TH-15-50

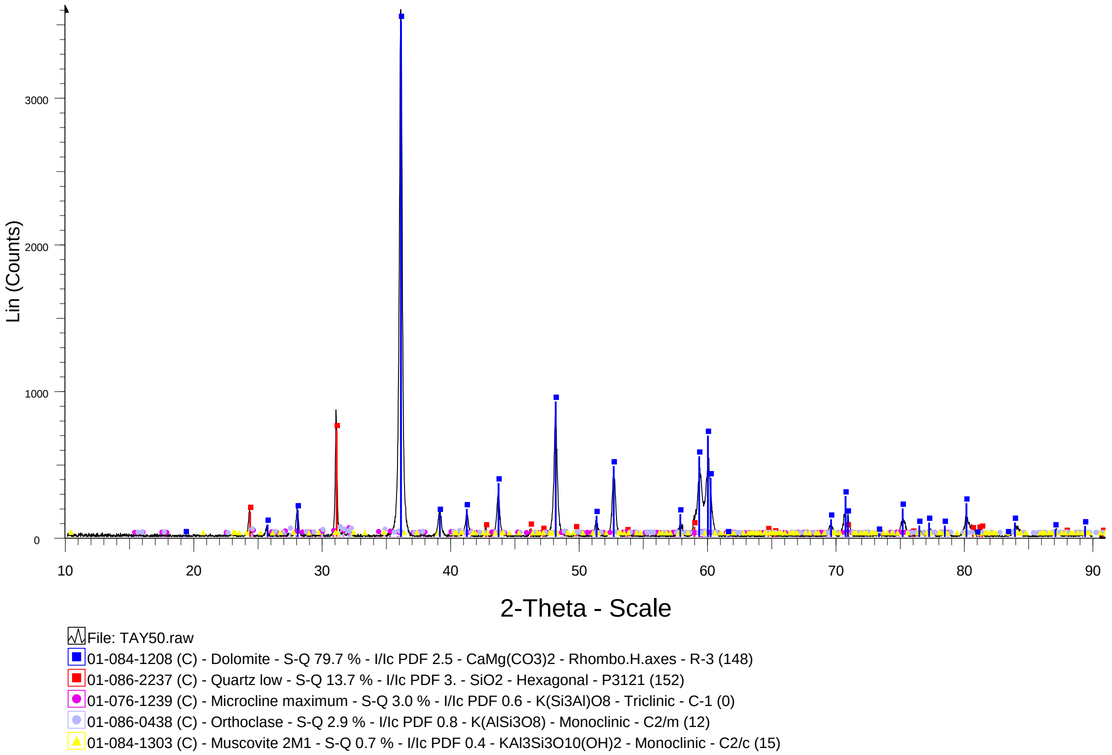

Sample TH-15-27

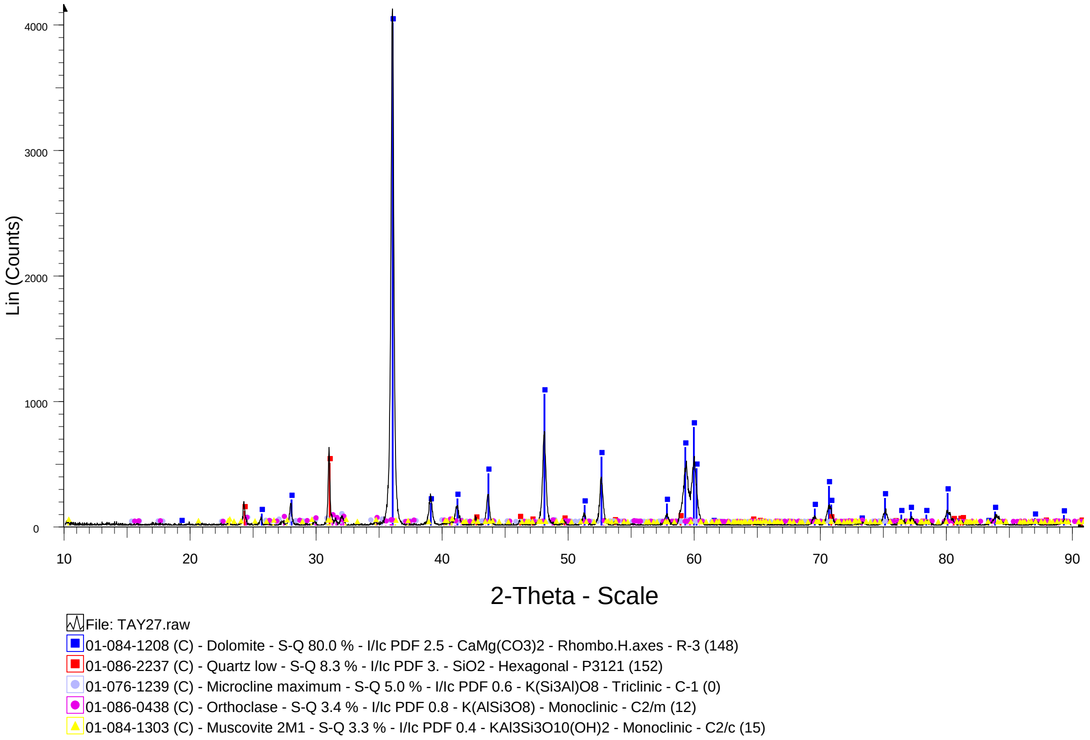

Sample TH-15-84a

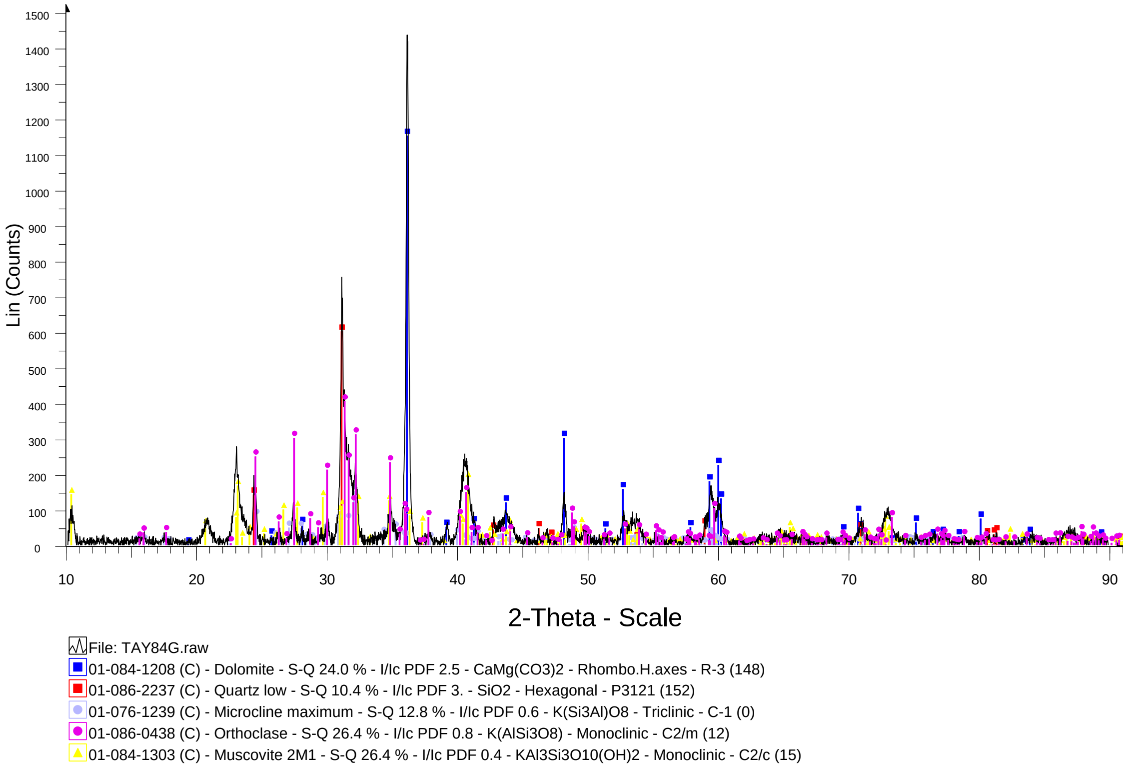

Sample TH-15-84b

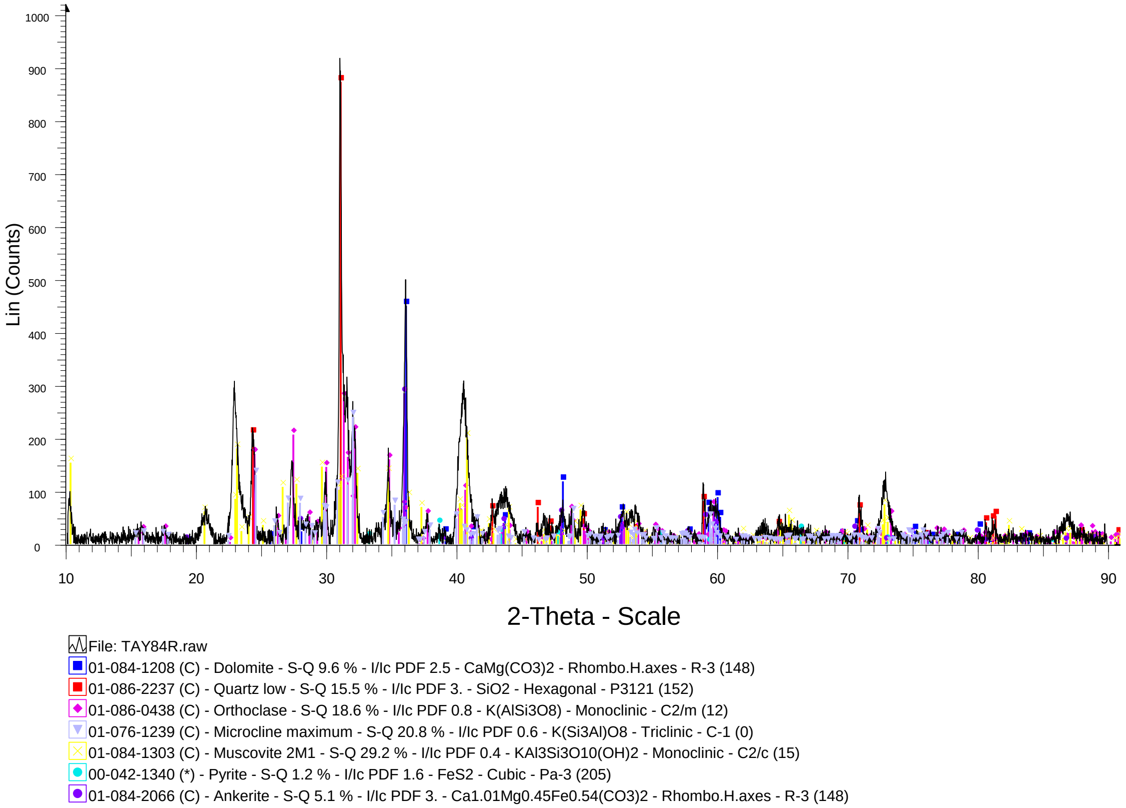

Curriculum Vitae

Name:	Taylor Haid
Post-secondary Education and Degrees:	University of Regina Regina, Saskatchewan, Canada 2009-2014 B.Sc. Honours (Geology) The University of Western Ontario London, Ontario, Canada 2014-2016 M.Sc. (candidate) Geology (Planetary Science)
Honours and Awards:	NSERC CREATE Technologies and Techniques for Earth and Space Exploration Fellowship 2014-2016 Northern Scientific Training Program Grant 2015 Global Opportunities Award 2015 Ontario Graduate Scholarship 2014-2015
Related Work Experience	Teaching Assistant The University of Western Ontario 2014-2016 Lab Instructor University of Regina 2013-2014

Publications:

Chi, G., Haid, T. M., Quirt, D., Fayek, M., Blamey, N., Chu, H. (2016) Petrography, fluid inclusion analysis and geochronology of the End uranium deposit, Kiggavik, Nunavut, Canada. Mineralium Deposita, 1-22.

Ryan, C. H., Haid, T. M., Osinski, G. R., Tornabene, L. L. (2016) 2015 CanMars MSR Analogue Mission: The Utilization of the Three-Dimensional Exploration Multispectral Microscope Imager (TEMMI) for In Situ Analysis. Lunar and Planetary Science Conference. Houston, Texas, March 2016 (poster).

Zylberman, W., Hickson, D., Haid, T. M., Osinski, G. R. (2016) 2015 CanMars MSR Analogue Mission: The Key Role of LiDAR in Rover Navigation and Potential for Future Missions. Lunar and Planetary Science Conference. Houston, Texas, March 2016 (poster).

Haid, T. M., Osinski G. R., (2016) Utilization of LiDAR intensity data for remote ore identification. Mineral Exploration Roundup. Vancouver, British Columbia, January 2016 (poster).

Haid, T. M., Osinski G. R., Tornabene L. L., (2015) Utilization of LiDAR for Geomorphological Analysis of Periglacial Features (abstract SE14A-0347). GACMAC Annual General Meeting. Montreal, Quebec, May 2015 (poster).

Chi, G., Liang, R., Ashton, K., Haid, T. M.., Quirt, D., Fayek, M. 2014. Evidence of fluid immiscibility from uranium deposits in northern Saskatchewan and Nunavut and potential relationship with uranium precipitation. GAC-MAC Annual General Meeting. Fredericton, New Brunswick, May 2014.

Haid, T. M., Chi, G., Quirt, D. 2013. A petrographic and fluid inclusion study of the End uranium deposit, Kiggavik, Nunavut: preliminary findings. Saskatchewan Geological Survey Open House Saskatoon, Saskatchewan, December 2013.